Heterojunctions and Nanostructures

Edited by Vasilios N. Stavrou

HETEROJUNCTIONS AND NANOSTRUCTURES

Edited by **Vasilios N. Stavrou**

Heterojunctions and Nanostructures
http://dx.doi.org/10.5772/intechopen.71162
Edited by Vasilios N. Stavrou

Contributors

Sunil Kumar Pradhan, Victor Barsan, Lianbi Li, Taro Kimura, Romain Giraud, Joseph Dufouleur, Moletlanyi Tshipa, Monkami Masale

Notice

Statements and opinions expressed in the chapters are these of the individual contributors and not necessarily those of the editors or publisher. No responsibility is accepted for the accuracy of information contained in the published chapters. The publisher assumes no responsibility for any damage or injury to persons or property arising out of the use of any materials, instructions, methods or ideas contained in the book.

We are IntechOpen,
the world's leading publisher of
Open Access books
Built by scientists, for scientists

3,650+
Open access books available

114,000+
International authors and editors

118M+
Downloads

151
Countries delivered to

Our authors are among the
Top 1%
most cited scientists

12.2%
Contributors from top 500 universities

CLARIVATE ANALYTICS
**BOOK
CITATION
INDEX**
INDEXED

WEB OF SCIENCE™

Selection of our books indexed in the Book Citation Index
in Web of Science™ Core Collection (BKCI)

Interested in publishing with us?
Contact book.department@intechopen.com

Numbers displayed above are based on latest data collected.
For more information visit www.intechopen.com

Meet the editor

Dr. V. N. Stavrou is currently an adjunct member at the Hellenic Naval Academy, Piraeus, Greece. He received his MSc and PhD degrees in Theoretical Solid-State Physics from the University of Essex in England, in 1995 and in 1999, respectively. He has held postdoctoral positions at the following research institutions: (a) Deutsche Forschungsanstalt fur Luft und Raumfahrt e.V (German Aerospace Research Center) in Germany; (b) Helsinki University of Technology; (c) State University of New York (SUNY) at Buffalo, USA; and (d) University of Iowa, USA. He is specifically interested in searching the electronic, optical, and lattice properties of semiconducting low-dimensional structures (quantum dots and quantum wells, among others). These properties are of special importance for the quantum computing architecture and laser technology. He has published his research work in reputable journals related, among others, to quantum computing, spintronics, decoherence in quantum dots, diluted magnetic semiconductors, and phonon models in low-dimensional structures.

Contents

Preface

A heterostructure is a sandwich of two dissimilar semiconductors (or other materials) with different bandgaps and lattice constants. The junction between two different materials is known as heterojunction. Nanostructures are structures that range between 1 nm and 100 nm in at least one dimension. In the case of semiconductor nanostructures, the carriers can be confined in one, two, or all three dimensions, and the structures are known as quantum wells, quantum wires, and quantum dots, respectively. The aforementioned structures, as well as many others, are of interest for various electronic and optoelectronic device applications such as diodes, lasers, spintronic devices, and dissipationless transistors for quantum computers, among others. Molecular beam epitaxy (MBE), metalorganic chemical vapor deposition (MOCVD), and some other micro-fabrication techniques are used to create high-quality heterostructures. Computational methods such as numerical integration and partial differential schemes have been mainly used to describe, among others, the carrier confinement, as well as the relaxation and dephasing rates.

A collection of research topics related to heterojunctions and nanostructures is presented in the current book. The first part of the book includes chapters related to topological insulators. A few presented topics are, among others, the topological phases of matter, the band topology of insulators and also of Weyl semimetals, transport properties of 3D topological insulator quantum wires and the influence of disorder, transport properties of quasi-1D (and 2D) topological surface states, quantum coherence, and the topological insulator thin-film Hall bar device. The second part of the book includes chapters related to the nanostructure devices for light emission. Topics such as semiconductor quantum nanowire laser diodes, solutions of Schrodinger equation in nanostructures, numerical methods, light-to-electricity conversion devices, photoexcited carrier transportation process in quantum wells and quantum dots, growth mode and characterization of heterostructure of large lattice mismatch, and photoionization cross section are included in the second section, among others.

As an editor of this book, I would like to thank all the authors for their contribution, their high-research standards, and their constructive feedback. Lastly, I would like to express my thanks and gratitude to the InTech team for their support during the preparation of this book.

Dr. Vasilios N. Stavrou
Hellenic Naval Academy
Piraeus, Greece

Topological Insulators

Analysis of Topological Material Surfaces

Taro Kimura

Abstract

We provide a systematic analysis of the boundary condition for the edge state, which is a ubiquitous feature in topological phases of matter. We show how to characterize the boundary condition, and how the edge state spectrum depends on it, with several examples, including 2d topological insulator and 3d Weyl semimetal. We also demonstrate the edge-of-edge state localized at the intersection of boundaries.

Keywords: topological insulator, Weyl semimetal, boundary condition, lattice fermion

1. Introduction

Study of topological phases of matter has been a hot topic in condensed-matter physics for recent years [1]. An importance of topological aspects of materials themselves was already noticed around the discovery of quantum Hall effect (QHE) in early 1980s. QHE is universally observed in a two-dimensional system, but it requires a strong magnetic field, which breaks time-reversal symmetry. A breakthrough after 20 years was the discovery of quantum spin Hall effect (QSHE), which actually demonstrates that a topological phase is possible even without breaking time-reversal symmetry. This opens a new window of the research on topological insulators (TIs) and topological superconductors (TSCs).

A universal feature of topological phases is the bulk/edge correspondence [2]: once the bulk wave function has a topologically nontrivial configuration; there exists a gapless edge state

localized at the boundary. Such an edge state is topologically protected, and thus is robust against any perturbations as long as respecting symmetry of the system. In practice, the edge state plays a significant role in detection of topological phases since it can be directly observed in experiments using angle-resolved photo-emission spectroscopy (ARPES). Therefore the boundary condition dependence of the edge state is expected to provide experimentally useful predictions.

In this article, we provide a systematic analysis of the boundary condition of topological material surfaces, including TIs and also Weyl semimetals (WSMs) [3, 4].[1] In Section 2, we discuss some preliminaries on the band topology of TI and WSM. We explain how one can obtain topological invariants from the band spectrum. In Section 3, we provide a systematic study of the boundary condition. We show how to obtain and characterize the boundary condition for a given Lagrangian or Hamiltonian. Then we apply this analysis to the edge state of 2d TI and 3d WSM both in the continuum effective model and the discretized lattice model. In Section 4, we extend the analysis to the situation with two boundaries in different directions. We demonstrate the existence of the edge state localized at the intersection of surfaces, that we call the edge-of-edge state.

2. Preliminaries: bulk, edge, and topology

In this section, we provide several preliminary aspects of topological materials. In particular, we show simple models, effectively describing the bulk of topological system, and discuss the role of topology thereof.

2.1. Bulk system

We start with a simple two-band Hamiltonian in two dimensions,

$$H_{2d} = -i\sigma_1 \frac{\partial}{\partial x_1} - i\sigma_2 \frac{\partial}{\partial x_2} + m\sigma_3 \tag{1}$$

where Pauli matrices are defined $\sigma_1 = \begin{pmatrix} 0 & 1 \\ 1 & 0 \end{pmatrix}$, $\sigma_2 = \begin{pmatrix} 0 & -i \\ i & 0 \end{pmatrix}$, $\sigma_3 = \begin{pmatrix} 1 & 0 \\ 0 & -1 \end{pmatrix}$. This is a simple effective model for 2d Integer QHE, classified into the 2d class A system according to the 10-fold way classification of TIs and TSCs [8, 9]. In order to investigate the band structure of this system, we consider the Bloch wave function $\Psi_{\vec{p}}\left(\vec{x}\right) = e^{i\vec{p}\cdot\vec{x}}\psi_{\vec{p}}\left(\vec{x}\right)$, and the corresponding Hamiltonian acting on $\psi_{\vec{p}}\left(\vec{x}\right)$, simply denoted by ψ below, is given by

---

[1] See also related works [5–7] for the boundary condition analysis of topological materials.

$$\mathcal{H}_{2d}\left(\vec{p}\right) = p_1\sigma_1 + p_2\sigma_2 + m\sigma_3 = \begin{pmatrix} m & \Delta^*\left(\vec{p}\right) \\ \Delta\left(\vec{p}\right) & -m \end{pmatrix}. \tag{2}$$

We obtain two eigenvalues $\epsilon_{\pm}\left(\vec{p}\right) = \pm\sqrt{\left|\vec{p}\right|^2 + m^2}$. The eigenstate, parametrized by a complex number $\xi \in \mathbb{C}$, is accordingly obtained as

$$\psi = \frac{1}{\sqrt{1+|\xi|^2}}\begin{pmatrix} 1 \\ \xi \end{pmatrix} \quad \text{with} \quad \xi = \frac{\Delta\left(\vec{p}\right)}{\epsilon + m} = \frac{\epsilon - m}{\Delta\left(\vec{p}\right)^*}. \tag{3}$$

We remark that the parameter ξ becomes singular $\xi \to \infty$ at $\vec{p} = 0$. At this point, we have to reparametrize the eigenstate with ξ^{-1} instead of ξ. This means that ξ is not a global, but just a local coordinate, and the eigenstate is given by an element of $\mathbb{C}\mathbf{P}^1$ in this model.

Since this system is gapped, we can neglect the transition between lower and upper bands as long as we consider the adiabatic process. Under such a process, we can consider the Berry connection and curvature defined from the gapped eigenstate[2]

$$\mathcal{A} = \psi^\dagger(id)\psi = -\text{Im}\frac{\xi^* d\xi}{1+|\xi|^2}, \qquad \mathcal{F} = d\mathcal{A} = i\frac{d\xi^* d\xi}{\left(1+|\xi|^2\right)^2} \tag{4}$$

where we use the differential form notation in the momentum space, $d = \left(\partial/\partial p_i\right)dp^i$, namely the Berry connection is one-form $\mathcal{A} = A_1 dp^1 + A_2 dp^2$, and the curvature is two-form $\mathcal{F} = F_{12}dp^1 dp^2$. Under the momentum-dependent transformation, $\xi \to e^{i\phi(\vec{p})}\xi$ (not an overall phase rotation of the eigenstate ψ), the connection behaves as $\mathcal{A} \to \mathcal{A} - d\phi/\left(1+|\xi|^2\right)$. This is a U(1) gauge transformation, which is local in momentum space, and the curvature is invariant under this transformation by itself. This U(1) structure is directly related to the S^1 fibration of $\mathbb{C}\mathbf{P}^1 = S^3/S^1$, and interpreted as a consequence of the particle number conservation of each eigenstate which holds under the adiabatic process.

An important point is that we can construct the topological invariant from the Berry connection and curvature (4). For the 2d system, it is given as an integral of the curvature over the momentum space,

$$\nu_{2d} = \frac{1}{2\pi}\int dp_1 dp_2\, F_{12} = \frac{1}{2}\,\text{sgn}\,(m) \tag{5}$$

which is called the TKNN number, which computes the Hall conductivity of the system [11]. We remark that it is invariant under the continuous deformation of the mass parameter, so that

---

[2]See a textbook on this topic, e.g., [10] for more details.

it would be a topological invariant, but with a discontinuous point at $m = 0$, which is the gapless (sign changing) point $m = 0$. Typically the topological number takes an integer value, but ν_{2d} does not. The reason why we obtain a half integer value is that we take a specific slice of the mass parameter in the total parameter space of the three-parameter Hamiltonian (2).

To explain this let us consider the 3d system as follows,

$$\mathcal{H}_{3d}\left(\vec{p}\right) = p_1\sigma_1 + p_2\sigma_2 + p_3\sigma_3 = \begin{pmatrix} p_3 & \Delta^*(p) \\ \Delta(p) & -p_3 \end{pmatrix} \tag{6}$$

which is known as an effective Hamiltonian of the WSM. This Hamiltonian is simply obtained from the 2d system (2) by replacing the mass parameter with another momentum p_3. We apply essentially the same analysis to this 3d system as 2d, and we obtain the genuine topological invariant:

$$\nu_{3d} = \frac{1}{4\pi}\int_{S^2} d\,\vec{S}\cdot\vec{B} = \frac{1}{2\pi}\int dp_1 dp_2 F_{12}\Big|_{p_3>0} - \frac{1}{2\pi}\int dp_1 dp_2 F_{12}\Big|_{p_3<0} = 1 \tag{7}$$

where the "magnetic field" is defined as $B^i = \frac{1}{2}\epsilon^{ijk}F_{jk}$, namely $\vec{B} = \vec{\nabla}\times\vec{A}$. This means that the gapless point (also called the Weyl point) plays a role as the magnetic monopole in the momentum space. As shown in **Figure 1**, the 2d invariant ν_{2d} is related to the 3d invariant through taking a constant p_3, identified with the mass m, which covers either upper or lower half of the monopole fluxes. This explains why the 2d invariant can be a half-integer, although the 3d invariant takes an integer value. We remark that, in this case, one cannot consider well-defined Berry phase, since the current 3d system is gapless in which the adiabatic process does not make sense. However, the topological invariant still plays a role to discuss stability of the Weyl point: Since a system having a nontrivial topological number, say $\nu_{3d}\neq 0$, cannot be
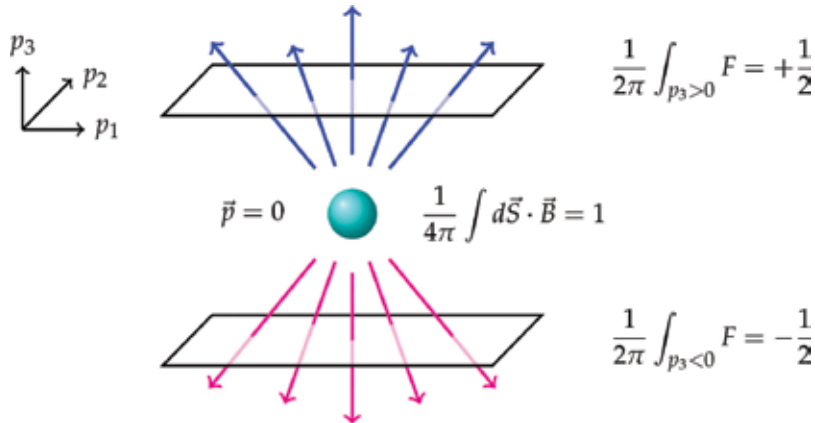

Figure 1. Monopole at Weyl point in the momentum space. The monopole charge is an integer-valued topological invariant ν_{3d}. The 2d invariant ν_{2d} is obtained at a constant $p_3(\to m)$ plane, which covers either upper or lower half of the fluxes, so that ν_{2d} is given by a half of ν_{3d}.

continuously deformed to a trivial system $\nu_{3d} = 0$ by definition. This explains the topological stability of the WSM. If we want to obtain a topologically trivial situation, we need pair-annihilation of the Weyl points having opposite topological invariants: $\nu_{3d} = (+1) + (-1) = 0$. See **Figure 2**.

2.2. Edge state

So far, we have discussed the bulk system, and the material boundary is not yet considered. Let us show a simple argument to incorporate the boundary of the system. If we have a material which has nontrivial topology, the vacuum, outside of the material, should be topologically trivial. Otherwise they cannot be topologically distinguished. As explained above, in order to obtain the topology change in the 2d system, we need the mass parameter whose sign is flipped at the boundary. For this purpose we impose a simple spatial dependence on the mass parameter as $m(x_1) = \vartheta x_1$ with a positive slope $\vartheta > 0$, giving rise to the sign flip at $x_1 = 0$, so that the boundary is the plane $x_1 = 0$ [12]. Then the Hamiltonian takes a form of

$$\mathscr{H}_{2d}(x_1, p_2) = m(x_1)\sigma_1 - i\sigma_2\frac{\partial}{\partial x_1} + p_2\sigma_3 = \begin{pmatrix} p_2 & \sqrt{2\vartheta}\hat{a}^\dagger \\ \sqrt{2\vartheta}\hat{a} & -p_2 \end{pmatrix} \tag{8}$$

where we exchange Pauli matrices compared with the previous one to simplify the expression. Since x_1-dependence remains in this system, we do not consider the momentum basis in x_1-direction, while the momentum in x_2-direction is now denoted by p_2. The off-diagonal element is given by an operator $\hat{a} = (\vartheta x_1 + (\partial/\partial x_1))/\sqrt{2\vartheta}$, $\hat{a}^\dagger = (\vartheta x_1 - (\partial/\partial x_1))/\sqrt{2\vartheta}$, obeying the commutation relation $\left[\hat{a}, \hat{a}^\dagger\right] = 1$, so that it is interpreted as a creation/annihilation operator. Then the energy spectrum is given by $\epsilon_n(p_2) = \pm\sqrt{p_2^2 + 2\vartheta n}$ for $n \geq 1$ (gapped), while the zero mode dispersion is given by $\epsilon_0(p_2) = p_2$ (gapless), which is the chiral edge state of the 2d class A system. See **Figure 3** for numerical plot of the spectrum. In general, we obtain the zero mode localized on the topological material boundary from the mass term

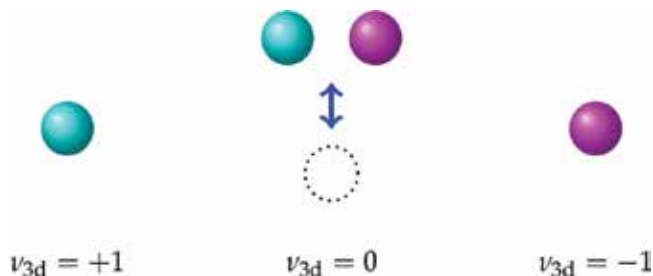$$\nu_{3d} = +1 \qquad \nu_{3d} = 0 \qquad \nu_{3d} = -1$$

Figure 2. The topological invariant distinguishes topologically different situations. The green and red spheres show the monopole with topological charge $\nu_{3d} = +1$ and $\nu_{3d} = -1$, respectively. We need pair annihilation to eliminate the monopoles.
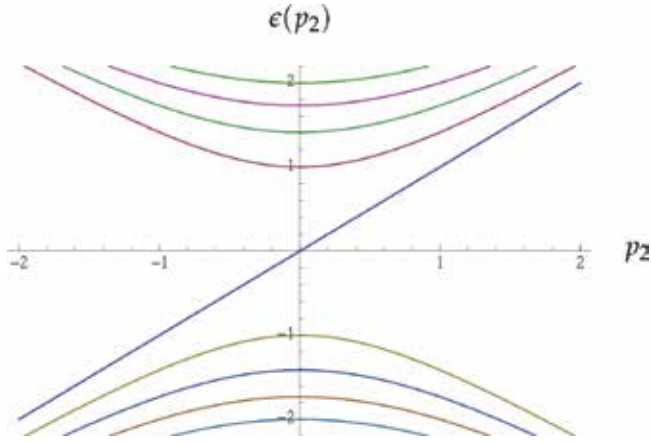
Figure 3. The dispersion relation of the edge state with $\vartheta = 1$. We find a gapless chiral mode specific to the 2d class A TI. The gapped spectra are interpreted as bulk contributions.

with a spatial profile, which is known as the domain-wall fermion. See, for example, [13] for more details.

2.3. Lattice system

Since the electron lives on a lattice in the material, studying the lattice model is important to understand the actual behavior of the electron. Let us introduce the Hamiltonian describing the electron on a lattice

$$H_{2d}^{lat} = -\frac{i}{2}\sigma_1\left(\nabla_1 - \nabla_1^\dagger\right) - \frac{i}{2}\sigma_2\left(\nabla_2 - \nabla_2^\dagger\right) + \sigma_3\left(m + 2 - \frac{1}{2}\left(\nabla_1 + \nabla_1^\dagger\right) - \frac{1}{2}\left(\nabla_2 + \nabla_2^\dagger\right)\right) \quad (9)$$

where we define the difference operator $\nabla_{1,2}\psi_{\vec{n}} = \psi_{\vec{n}+\vec{e}_{1,2}} - \psi_{\vec{n}}$ with the unit vector $\vec{e}_{1,2}$ in n_1 and n_2-direction. Then the corresponding Bloch Hamiltonian is given by

$$\mathcal{H}_{2d}^{lat}\left(\vec{p}\right) = \sigma_1 \sin p_1 + \sigma_2 \sin p_2 + \sigma_3\left(m + 2 - \cos p_1 - \cos p_2\right). \quad (10)$$

Periodicity $p_{1,2} \sim p_{1,2} + 2\pi$ reflects the lattice structure: The momentum is restricted to the Brillouin zone $p_{1,2} \in [0, 2\pi]$. The spectrum is given by $\epsilon\left(\vec{p}\right) = \pm\sqrt{\left(\sin p_1\right)^2 + \left(\sin p_2\right)^2 + \left(m + 2 - \cos p_1 - \cos p_2\right)^2}$, which has four gapless points $\vec{p} = (0,0)$ at $m = 0$, $\vec{p} = (\pi, 0)$ and $(0, \pi)$ at $m = -2$, $\vec{p} = (\pi, \pi)$ at $m = -4$. Expanding the momentum around $\vec{p} = (0,0)$, one can see the effective Hamiltonian (2) is obtained. If expanding the momentum around $\vec{p} = (\pi, 0)$ instead, we similarly obtain the Hamiltonian (2), but we have to replace $p_1 \rightarrow -p_1$.
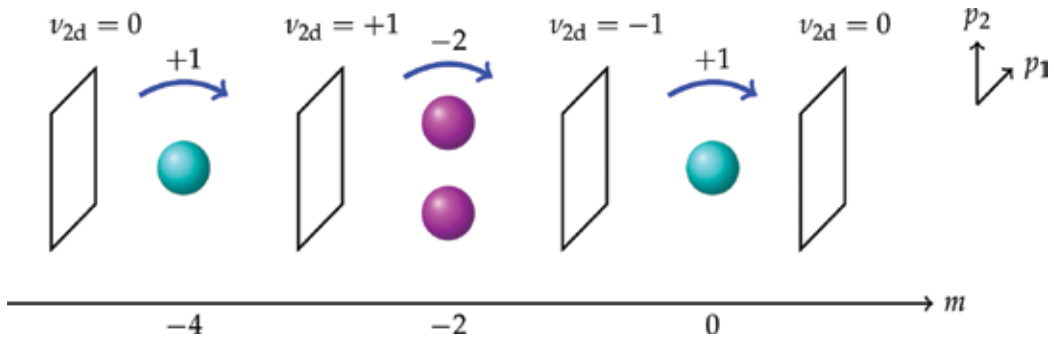
Figure 4. The mass dependence of the 2d topological invariant ν_{2d} for the lattice model (10). Topology change occurs at the gapless points $m = -4, -2, 0$. Change of the invariant corresponds to the monopole charge $+1, -2, +1$ associated with each gapless point.

Let us see the topological structure of the lattice model. Applying the same procedure to the Hamiltonian (10), we obtain the topological invariant as follows [14]:

$$\nu_{2d} = \frac{1}{2\pi} \int_{BZ} dp_1 dp_2 \, F_{12} = \begin{cases} 0 & (m > 0 \text{ or } m < -4) \\ -1 & (-2 < m < 0) \\ +1 & (-4 < m < -2) \end{cases} \tag{11}$$

where the momentum integral is taken over the Brillouin zone. In contrast to the continuum effective model, we have integer valued topological invariants in this case. This is essentially related to the anomaly of $(2 + 1)$-dimensional Dirac system, known as the parity anomaly. However, it is also known that the lattice regularization naively gives rise to an anomaly-free system: The gapless points have to appear as a pair, so that each anomalous contribution is canceled with each other [15, 16]. Actually the present model (10) has four gapless points in the parameter space: $(p_1, p_2, m) = (0, 0, 0)$, $(\pi, 0, -2)$, $(0, \pi, -2)$, $(\pi, \pi, -4)$. Each gapless point plays basically the same role as that discussed in the continuum model with the monopole charge $+1$ or -1. Thus we immediately obtain $\nu_{2d} = \frac{1}{2}(+1 - 2 + 1) = 0$ for $m > 0$, $\frac{1}{2}(-1 - 2 + 1) = 1$ for $-2 < m < 0$, $\frac{1}{2}(-1 + 2 + 1) = 1$ for $-4 < m < -2$, and $\frac{1}{2}(-1 + 2 - 1) = 0$ for $m < -4$. See **Figure 4**.

We can similarly consider a lattice model for 3d WSM system. We consider the Hamiltonian defined on a 3d lattice

$$H_{3d}^{lat} = \frac{1}{2}\sigma_1 \big(\nabla_1 + \nabla_1^\dagger - \nabla_2 - \nabla_2^\dagger + 2c\big) - \frac{i}{2}\sigma_2 \big(\nabla_2 - \nabla_2^\dagger\big) - \frac{i}{2}\sigma_3 \big(\nabla_3 - \nabla_3^\dagger\big). \tag{12}$$

The corresponding Bloch Hamiltonian is given by

$$\mathcal{H}_{3d}^{lat}\big(\vec{p}\big) = \sigma_1 \big(\cos p_1 - \cos p_2 + c\big) + \sigma_2 \sin p_2 + \sigma_3 \sin p_3, \tag{13}$$

and the spectrum yields $\epsilon\left(\vec{p}\right) = \pm\sqrt{\left(\cos p_1 - \cos p_2 + c\right)^2 + \left(\sin p_2\right)^2 + \left(\sin p_3\right)^2}$. The parameter c tunes the gapless Weyl points as follows

$$(p_1, p_2, p_3) = \begin{cases} \left(\cos^{-1}(1-c), 0, 0\right) \ \& \ \left(\cos^{-1}(1+c), 0, \pi\right) & (0 < c < 2) \\ \left(\cos^{-1}(-1-c), \pi, 0\right) \ \& \ \left(\cos^{-1}(1+c), \pi, \pi\right) & (-2 < c < 0) \\ \text{n/a} & (|c| > 2) \end{cases} \quad (14)$$

The band spectrum is shown in **Figure 5** at $p_3 = 0$ and $c = 1$. We can see two Weyl points at $(p_1, p_2) = (\pm\pi/2, 0)$. We will study the boundary condition of this model in Section 3.3.

2.4. Higher-dimensional system

So far we have considered a simple system in two and three dimensions. We can even discuss such a topological structure in the momentum space of more involved systems. In this section we discuss a higher-dimensional generalization of the system discussed above. Dimensional reduction of this system gives rise to several interesting situations in 2d and 3d.

We consider a four-band model defined in four spatial dimensions, which is a natural higher-dimensional generalization of (2),

$$\mathcal{H}_{4d}(p) = p \cdot \gamma + m\gamma_5 = \begin{pmatrix} m & \Delta(p)^\dagger \\ \Delta(p) & -m \end{pmatrix} \quad \text{with} \quad \Delta(p) = p \cdot \sigma = \begin{pmatrix} p_4 + ip_3 & p_2 + ip_1 \\ -p_2 + ip_1 & p_4 - ip_3 \end{pmatrix} \quad (15)$$

where we use the gamma matrices defined as $\gamma_k = \begin{pmatrix} 0 & -i\sigma_k \\ \sigma_k & 0 \end{pmatrix}$ for $k = 1, 2, 3$, $\gamma_4 = \begin{pmatrix} 0 & \mathbb{1} \\ \mathbb{1} & 0 \end{pmatrix}$,
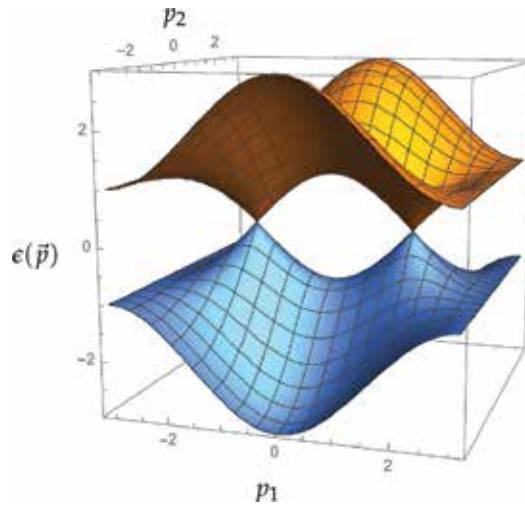

Figure 5. The energy spectrum of the lattice WSM model (13) with $p_3 = 0$ and $c = 1$. There exist two gapless Weyl points at $(p_1, p_2) = (\pm\pi/2, 0)$. The parameter c characterizes the distance between the Weyl points.

$\gamma_5 = \begin{pmatrix} \mathbb{1} & 0 \\ 0 & -\mathbb{1} \end{pmatrix}$, and the off-diagonal element is given by $\Delta(p) = p \cdot \sigma \in \mathbb{H}$ with $\sigma = (i\,\vec{\sigma}, \mathbb{1})$.
We remark that this Hamiltonian is a 4×4 matrix, such that each element shows a 2×2
matrix. The spectrum is simply obtained as $\epsilon(p) = \pm\sqrt{|p|^2 + m^2}$, and each state is doubly
degenerated. We have a similar eigenvector to (3) as follows,

$$\psi = \frac{1}{\sqrt{1 + |\xi|^2}} \begin{pmatrix} \mathbb{1} \\ \xi \end{pmatrix} \quad \text{with} \quad \xi = \frac{\Delta}{\epsilon + m} = \frac{\epsilon - m}{\Delta^\dagger} \in \mathbb{H}. \tag{16}$$

Currently each component shows a 2×2 matrix, which takes a value in quaternion $\mathbb{H}$, so that
the eigenvector is a 2×4 matrix due to the degeneracy, namely $\psi = (\psi_1 \; \psi_2)$, where each $\psi_{1,2}$
is a four vector. For a degenerated system, we can define non-Abelian analog of the Berry
connection $\mathcal{A}_{ab} = \psi_a^\dagger(id)\psi_b$ for $a, b = 1, 2$. In this case, we obtain an SU(2) valued Berry connec-
tion, which is a consequence of S^3 fibration of $\mathbb{H}\mathbf{P}^1 = S^7/S^3$. The topological invariant for the
4d system is given by the four-dimensional momentum integral of the second Chern class,
which is known as the instanton number,

$$\nu_{4d} = -\frac{1}{8\pi^2} \int \text{Tr}\mathcal{F} \wedge \mathcal{F} = \frac{1}{2}\text{sign}(m). \tag{17}$$

Actually the instanton configuration obtained here, by solving a matrix equation, is closely
related to the ADHM construction. See [12] for more details. We again obtain a half-integer
topological invariant. The reason is totally parallel with the previous case. To obtain an integer
valued topological invariant, we consider the 5d uplift, the 5d WSM, obtained by replacing the
mass with another momentum $m \rightarrow p_5$,

$$\mathcal{H}_{5d}(p) = p \cdot \gamma + p_5\gamma_5, \tag{18}$$

and thus the integral over the 5d momentum space, instead of 4d, gives rise to

$$\nu_{5d} = -\frac{1}{8\pi^2} \int_{S^4} \text{Tr}\mathcal{F} \wedge \mathcal{F} = 1, \tag{19}$$

which implies the SU(2) monopole, called the Wu-Yang monopole, at the origin in the momen-
tum space. Then the 4d momentum integral performed to obtain the 4d invariant ν_{4d} is
equivalent to the hemisphere integral of S^4, which provides a half of the 5d invariant.

3. Boundary condition analysis

3.1. Operator formalism

In order to discuss the boundary condition, we start with a first order Hermitian differential
operator [3, 4, 17, 18]

$$\widehat{D} = -i\sigma \frac{\partial}{\partial x}. \tag{20}$$

Now we put a Pauli matrix σ, but we can consider a generic Hermitian matrix. Considering the inner product in a finite size system defined on the interval $x \in [x_L, x_R]$, we obtain

$$\begin{aligned} \left\langle \phi \middle| \widehat{D}\psi \right\rangle &= \int_{x_L}^{x_R} dx\, \phi(x)^\dagger \left(-i\sigma \frac{\partial}{\partial x} \psi(x) \right) \\ &= \phi(x)^\dagger (-i\sigma)\psi(x) \Big|_{x_L}^{x_R} + \int_{x_L}^{x_R} dx \left(-i\sigma \frac{\partial}{\partial x} \phi(x) \right)^\dagger \psi(x) \\ &= \phi(x)^\dagger (-i\sigma)\psi(x) \Big|_{x_L}^{x_R} + \left\langle \widehat{D}\phi \middle| \psi \right\rangle. \end{aligned} \tag{21}$$

The Hermitian condition $\left\langle \phi \middle| \widehat{D}\psi \right\rangle = \left\langle \widehat{D}\phi \middle| \psi \right\rangle$ implies that the surface term should vanish

$$\phi(x)^\dagger \sigma \psi(x) \Big|_{x_L}^{x_R} = \phi(x_R)^\dagger \sigma \psi(x_R) - \phi(x_L)^\dagger \sigma \psi(x_L) = 0, \tag{22}$$

which gives rise to two possibilities:

1.   Periodic boundary condition: $\phi(x_R) = \phi(x_L)$ and $\psi(x_R) = \psi(x_L)$

2.   Open boundary condition: $\phi(x_R)^\dagger \sigma \psi(x_R) = 0$ and $\phi(x_L)^\dagger \sigma \psi(x_L) = 0$

In particular, the open boundary condition 2 has the following solution

$$P\psi\big|_{x_{L,R}} = P\phi\big|_{x_{L,R}} = 0 \quad \text{where} \quad P = \frac{\mathbb{1} - M}{2} \tag{23}$$

with the matrix M satisfying $M^\dagger \sigma + \sigma M = 0$, since $\psi = M\psi$, $\phi = M\phi$ at the boundary, then

$$\phi^\dagger \sigma \psi = \phi^\dagger \sigma M\psi = -\phi^\dagger M^\dagger \sigma \psi = -\phi^\dagger \sigma \psi \quad \Rightarrow \quad \phi^\dagger \sigma \psi = 0. \tag{24}$$

In general we can apply different matrices $M_{L,R}$ for x_L and x_R, but here we assume $M_{L,R} = M$ for simplicity, namely the same boundary condition for $x_{L,R}$. We remark that the condition (23) is specific to the operator choice (20). We have to derive the corresponding boundary condition case by case. We will show a generic formulation of the boundary condition using the Lagrangian formalism in Section 3.2.

3.1.1. Lattice system

Let us apply the similar argument to the lattice system defined on a one-dimensional interval $n \in \{1, \ldots, N\}$. We introduce an analogous difference operator to (20) as

$$\widehat{D}_{\text{lat}} = -i\sigma\nabla \tag{25}$$

where $\nabla\psi_n = \psi_{n+1} - \psi_n$ and $\nabla^\dagger \psi_n = \psi_{n-1} - \psi_n$. In this case, the inner product $\left\langle \phi \middle| \widehat{D}_{\text{lat}}\psi \right\rangle$ is given by

$$\sum_{n=1}^{N} \phi_n^\dagger \left(-i\sigma \nabla \psi_n \right) = \sum_{n=1}^{N} \left(i\sigma \nabla^\dagger \phi_n \right)^\dagger \psi_n + \phi_0^\dagger (i\sigma) \psi_1 - \phi_N^\dagger (i\sigma) \psi_{N+1} \qquad (26)$$

where ϕ_0 and ψ_{N+1} are considered as auxiliary fields. The self-conjugacy condition $\left\langle \phi \middle| \widehat{D}_{\text{lat}} \psi \right\rangle = \left\langle \widehat{D}_{\text{lat}} \phi \middle| \psi \right\rangle$ requires that the surface term should vanish:

$$\phi_0^\dagger \sigma \psi_1 - \phi_N^\dagger \sigma \psi_{N+1} = 0. \qquad (27)$$

The periodic boundary condition $\phi_{n+N} = \phi_n$, $\psi_{n+N} = \psi_n$ is a simple solution to this. The other possibility is that each term independently vanishes, corresponding to the open boundary condition. This means that the lattice system is similarly considered as the continuum system, and the open boundary condition is imposed by (23). We remark that for the lattice system the surface term (27) is not given by the on-site term, but involving a hopping to the next site. This suggests that we have to take care of the locality and continuum limit of the system.

3.1.2. Example

Let us consider an example with $\sigma = \sigma_3$. Then the matrix M should be a linear combination of $\sigma_{1,2}$. Since the operator P has a zero eigenvalue, the determinant should vanish $\det P = 0$, which leads to

$$M = \sigma_1 \cos\theta + \sigma_2 \sin\theta = \begin{pmatrix} 0 & e^{-i\theta} \\ e^{i\theta} & 0 \end{pmatrix}, \qquad (28)$$

obeying $M^\dagger = M$ and $M^2 = \mathbb{1}$ with two eigenvalues ± 1. It is also expressed as $M = \sigma_1 e^{i\theta\sigma_3} = \sigma_2 e^{i\left(\theta - \frac{\pi}{2}\right)\sigma_3}$. Thus the operator $P (= P^\dagger)$ turns out to be a projection operator $P^2 = P$ having eigenvalues $1, 0$ with the corresponding eigenvectors

$$P \begin{pmatrix} 1 \\ -e^{i\theta} \end{pmatrix} = \begin{pmatrix} 1 \\ -e^{i\theta} \end{pmatrix} \qquad \text{and} \qquad P \begin{pmatrix} 1 \\ e^{i\theta} \end{pmatrix} = 0. \qquad (29)$$

We remark $\sigma_3 P = \breve{P}\sigma_3$, $\sigma_3\breve{P} = P\sigma_3$ where $\breve{P} = \mathbb{1} - P$ obeying $\breve{P}P = P\breve{P} = 0$. Thus we obtain a one-parameter family of the solution to the boundary condition (23),

$$\psi \Big|_{x_{L,R}} \propto \begin{pmatrix} 1 \\ e^{i\theta} \end{pmatrix}. \qquad (30)$$

Since $\breve{P}\psi = \psi$, the current in x_3-direction vanishes at the boundary, $J_3 = \psi^\dagger \sigma_3 \psi = \psi^\dagger \breve{P}\sigma_3 \breve{P}\psi = \psi^\dagger \sigma_3 P\breve{P}\psi = 0$. In other words, the open boundary condition is interpreted as a vanishing condition for the normal component of the current as expected.

3.2. Lagrangian formalism

We explain how to derive a proper boundary condition for a given system with the Lagrangian formalism. The integral over the spacetime $\mathcal{M}$ of the Lagrangian defines the action

$$S = \int_{\mathcal{M}} \mathcal{L}(\phi, \partial\phi). \tag{31}$$

If the system has a continuous local symmetry, the action may be invariant under the infinitesimal deviation of the field $\phi \to \phi + \epsilon(x)\varphi$[3]:

$$0 = \delta S$$

$$= \int_{\mathcal{M}} \left(\frac{\partial \mathcal{L}}{\partial \phi} - \partial_\mu \left(\frac{\partial \mathcal{L}}{\partial(\partial_\mu \phi)} \right) \right) \epsilon(x)\varphi - \int_{\mathcal{M}} \epsilon(x)\partial_\mu \left(\frac{\partial \mathcal{L}}{\partial(\partial_\mu \phi)} \varphi \right) + \int_{\mathcal{M}} \partial_\mu \left(\frac{\partial \mathcal{L}}{\partial(\partial_\mu \phi)} \epsilon(x)\varphi \right). \tag{32}$$

The first term vanishes due to the Euler-Lagrange equation of motion for the bulk, $\frac{\partial \mathcal{L}}{\partial \phi} - \partial_\mu \left(\frac{\partial \mathcal{L}}{\partial(\partial_\mu \phi)} \right) = 0$. The vanishing condition for the second term implies the current $J^\mu = \frac{\partial \mathcal{L}}{\partial(\partial_\mu \phi)} \varphi$, satisfying the conservation law $\partial_\mu J^\mu = 0$, a.k.a. the Nöther current. The third term is a surface contribution which plays a role in the system with the boundary. The invariance of the action is thus rephrased as

$$0 = \int_{\partial\mathcal{M}} \epsilon(x) n \cdot J \tag{33}$$

where n is the normal vector defined as $\int_{\mathcal{M}} \partial_\mu V^\mu = \int_{\partial\mathcal{M}} n \cdot V$ with an arbitrary vector field V^μ and the boundary of the manifold denoted by $\partial\mathcal{M}$. This ends up with the condition such that the normal component of the current should vanish at the boundary

$$n \cdot J \big|_{\partial\mathcal{M}} = 0. \tag{34}$$

This seems physically reasonable and consistent with the previous argument in Section 3.1.2 because at the boundary there is no ingoing and outgoing current.

Furthermore, this zero current condition can be modified by taking into account the additional surface contribution to the action

$$S_B = \int_{\partial\mathcal{M}} \mathcal{L}_B(\phi) \tag{35}$$

where we assume the boundary d.o.f. is not dynamical (not including the derivative $\partial\phi$). Then the condition (34) becomes

$$\left[n \cdot J + \frac{\partial \mathcal{L}_B}{\partial \phi} \varphi \right]_{\partial\mathcal{M}} = 0. \tag{36}$$

This characterizes the boundary condition. In the following, we consider several examples to see how the boundary condition plays a role in the topological materials.

---

[3]This is an assumption. In general, the action itself is not invariant under the deviation.

3.3. 3d Weyl semimetal

3.3.1. Continuum system

Let us apply the argument discussed above to the WSM system. We consider the effective Hamiltonian (6) with a slight modification

$$\mathscr{H}_{3d}\left(\vec{p}, x_3\right) = p_1\sigma_1 + p_2\sigma_2 - i\sigma_3\frac{\partial}{\partial x_3}. \tag{37}$$

We put a boundary only at $x_3 = 0$ for simplicity, so that the system is defined on a positive domain $x_3 > 0$. In this case, since the current operator is defined as $\vec{J} = \psi^\dagger \vec{\sigma} \psi$, the boundary condition, corresponding to the zero current condition (36), that we impose is[4]

$$\psi^\dagger\sigma_3\psi\Big|_{x_3=0} = 0. \tag{38}$$

The eigenstate satisfying the condition (38) is parameterized by a single phase factor

$$\psi\left(\vec{p}, x_3\right) = \sqrt{\alpha\left(\vec{p}\right)}e^{-\alpha(\vec{p})x_3}\begin{pmatrix} 1 \\ e^{i\theta} \end{pmatrix} \tag{39}$$

which is normalized as $\int_0^\infty dx_3\,\psi^\dagger\psi = 1$, and the normalizability requires $\alpha\left(\vec{p}\right) > 0$. This eigenstate is localized on the boundary $x_3 = 0$ and exponentially decay into the bulk $x_3 > 0$ due to the factor $e^{-\alpha(\vec{p})x_3}$, where the parameter $\alpha\left(\vec{p}\right)$ plays a role as the inverse penetration length. In this case, the exponential factor $e^{-\alpha(\vec{p})x_3}$ is responsible for the x_3-direction dependence, instead of the plane wave factor $e^{ip_3x_3}$ used for the bulk analysis. In other words, the current analysis of the edge state uses Laplace basis instead of Fourier basis. Therefore, under the replacement $p_3 \to i\alpha$, we can apply almost the same analysis.

Then the spectrum and the inverse penetration length of the edge state are obtained from the eigenvalue equation, given as follows

$$\epsilon\left(\vec{p}\right) = p_1\cos\theta + p_2\sin\theta, \qquad \alpha\left(\vec{p}\right) = -p_1\sin\theta + p_2\cos\theta. \tag{40}$$

Actually it is written using an SO(2) transformation with the relation $\epsilon^2 + \alpha^2 = \left|\vec{p}\right|^2$,

$$\begin{pmatrix} \epsilon \\ \alpha \end{pmatrix} = \begin{pmatrix} \cos\theta & \sin\theta \\ -\sin\theta & \cos\theta \end{pmatrix}\begin{pmatrix} p_1 \\ p_2 \end{pmatrix}. \tag{41}$$

We show the spectrum of the edge state depending on the boundary condition with the bulk spectrum in **Figure 6**. We remark that the edge state cannot be defined in the whole

---

[4]This is of course equivalent to the boundary condition discussed in Section 3.1.2.

momentum space due to the normalizability condition $\alpha\left(\vec{p}\right) > 0$. Such a bounded spectrum associated with the WSM edge state is called the Fermi arc, and the boundary condition parameter, a relative phase factor, parameterizes the direction of the arc. Accordingly the current similarly behaves as $(J_1, J_2, J_3) \propto (\cos\theta, \sin\theta, 0)$.

3.3.2. Lattice system

Let us apply a similar analysis to the lattice model for 3d WSM. We consider the lattice model (13) with a boundary at $n_3 = 1$, defined on the positive n_3 region, $n_3 \geq 1$,

$$\mathscr{H}_{3d}^{lat}\left(\vec{p}, n_3\right) = \begin{pmatrix} 0 & \Delta\left(\vec{p}\right)^* \\ \Delta\left(\vec{p}\right) & 0 \end{pmatrix} - \frac{i}{2}\sigma_3\left(\nabla_3 - \nabla_3^\dagger\right) \tag{42}$$

with a complex parameter

$$\Delta\left(\vec{p}\right) = \cos p_1 - \cos p_2 + c + i\sin p_2, \tag{43}$$

which is analogous to the model in the continuum $\Delta\left(\vec{p}\right) \sim p_1 \pm ip_2$. We keep an explicit n_3-dependence of the system to deal with the boundary condition. According to the discussion in Sections 3.1.1 and 3.1.2, we consider the edge state consistent with the boundary condition as

$$\psi\left(\vec{p}, n_3\right) = \beta\left(\vec{p}\right)^{n_3-1}\begin{pmatrix} 1 \\ e^{i\theta} \end{pmatrix} \tag{44}$$

where $\beta\left(\vec{p}\right)$ is a real parameter, corresponding to the penetration depth, and the normalizability requires $|\beta\left(\vec{p}\right)| < 1$. In particular, we consider the situation $0 < \beta\left(\vec{p}\right) < 1$ for the moment: The negative $\beta\left(\vec{p}\right)$ solution is interpreted as a doubling counterpart of the positive one. The eigen-value equation $\mathscr{H}_{3d}^{lat}\left(\vec{p}, n_3\right)\psi\left(\vec{p}, n_3\right) = \epsilon\left(\vec{p}\right)\psi\left(\vec{p}, n_3\right)$ leads to
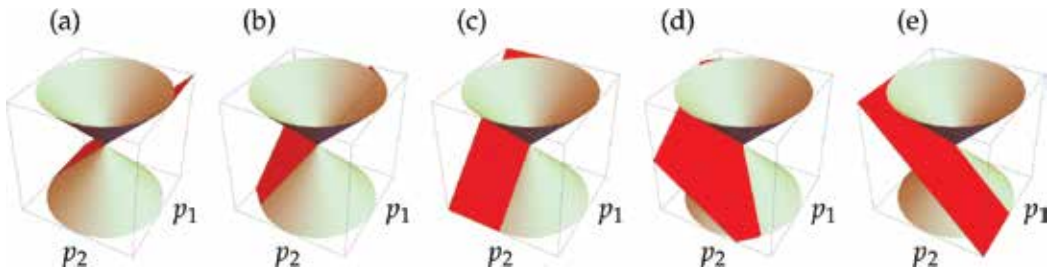

Figure 6. The boundary condition dependence of the edge state spectrum for $\theta = 0, \pi/4, \pi/2, 3\pi/4, \pi$ with the bulk spectrum. The parameter θ plays a role as a rotation angle in the momentum space.

$$\mathcal{D}\psi\left(\vec{p},n_3\right)=0 \quad \text{with} \quad \mathcal{D}=\begin{pmatrix} i\tilde{\alpha}\left(\vec{p}\right)-\epsilon\left(\vec{p}\right) & \Delta\left(\vec{p}\right)^* \\ \Delta\left(\vec{p}\right) & -i\tilde{\alpha}\left(\vec{p}\right)-\epsilon\left(\vec{p}\right) \end{pmatrix} \tag{45}$$

where we define $\tilde{\alpha}\left(\vec{p}\right)=\frac{\beta(\vec{p})^{-1}-\beta(\vec{p})}{2}$. Since we consider the situation $0<\beta\left(\vec{p}\right)<1$, it turns out $\tilde{\alpha}\left(\vec{p}\right)>0$. The solution is then obtained as

$$\epsilon\left(\vec{p}\right)=\cos\theta \text{Re}\Delta\left(\vec{p}\right)+\sin\theta \text{Im}\Delta\left(\vec{p}\right) \tag{46}$$

$$\tilde{\alpha}\left(\vec{p}\right)=-\sin\theta \text{Re}\Delta\left(\vec{p}\right)+\cos\theta \text{Im}\Delta\left(\vec{p}\right) \tag{47}$$

which has an analogous expression as (41) using SO(2) rotation

$$\begin{pmatrix} \epsilon \\ \tilde{\alpha} \end{pmatrix}=\begin{pmatrix} \cos\theta & \sin\theta \\ -\sin\theta & \cos\theta \end{pmatrix}\begin{pmatrix} \text{Re}\Delta \\ \text{Im}\Delta \end{pmatrix}. \tag{48}$$

At this moment, it is obvious that the spectrum of the current lattice model is parallel with the continuum model under the correspondence $(p_1,p_2,\alpha)\leftrightarrow(\text{Re}\Delta,\text{Im}\Delta,\tilde{\alpha})$.

We show the spectrum of the edge state in **Figure 7**, in particular, its boundary condition dependence. **Figure 8** shows constant energy slices of the spectrum. We can see the so-called Fermi arc, which connects two bulk Weyl points. As discussed for the continuum model, the boundary condition parameter plays a role as a rotation angle in the momentum space.

3.4. 2d topological insulator

3.4.1. Continuum system

The 2d class A TI is given by the dimensional reduction of the 3d WSM. Replacing $p_2 \to m$ in the Hamiltonian (37), we obtain

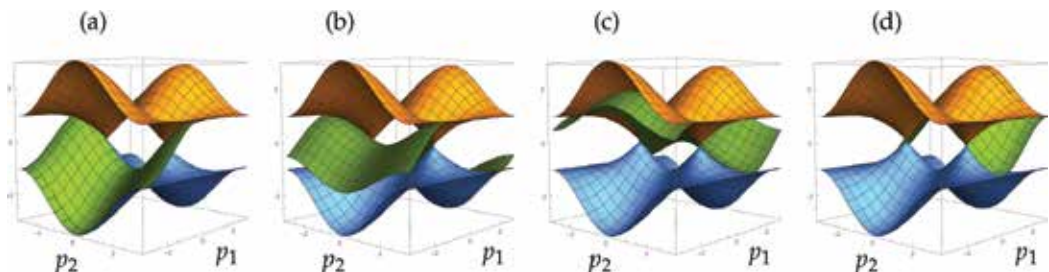**Figure 7.** The boundary condition dependence of the edge state spectrum $\epsilon\left(\vec{p}\right)$ for $\theta=\pi4,\pi/3,5\pi/3,2\pi$ (green), in addition to the bulk spectrum (orange and blue), the parameter c is taken to be $c=1$.
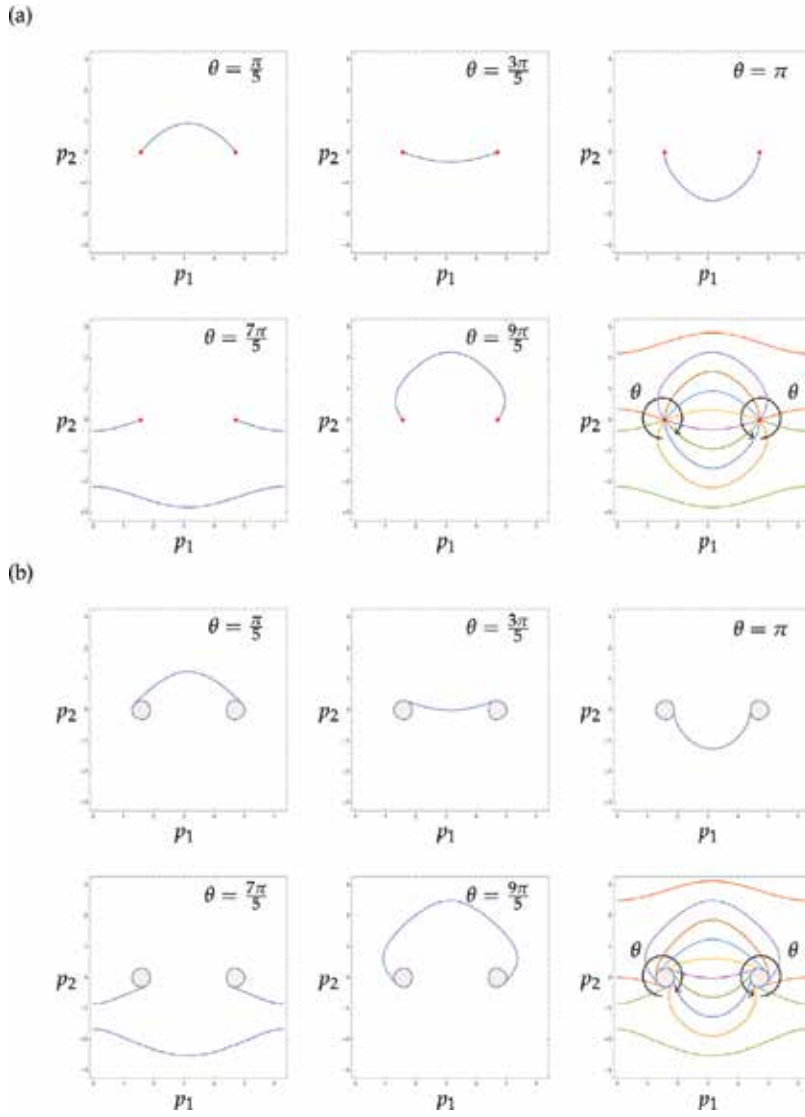
Figure 8. The Fermi arc at (a) zero energy $\varepsilon\left(\vec{p}\right) = 0$ and (b) finite energy $\epsilon\left(\vec{p}\right) = 0.3$ with $\theta = \pi/5, 3\pi/5, \pi, 7\pi/5, 9\pi/5$. The red dot and shaded region show the bulk contribution. The last panels show Fermi arcs with various values of the parameter θ.

$$\mathscr{H}_{2d}\left(p_1, x_3\right) = p_1\sigma_1 + m\sigma_2 - i\sigma_3\frac{\partial}{\partial x_3}. \tag{49}$$

After this dimensional reduction, we can apply totally the same analysis to this model discussed in Section 3.3: we consider the localized edge state satisfying the boundary condition

$$\psi(p_1, x_3) = \sqrt{\alpha(p_1)}e^{-\alpha(p_1)x_3}\begin{pmatrix} 1 \\ e^{i\theta} \end{pmatrix} \qquad (50)$$

where the inverse penetration depth $\alpha(p_1)$ has to be positive due to the normalizability. Then we obtain the solution

$$\epsilon(p_1) = p_1\cos\theta + m\sin\theta, \qquad \alpha(p_1) = -p_1\sin\theta + m\cos\theta. \qquad (51)$$

Figure 9 shows the boundary condition dependence of the edge state spectrum. Replacement $p_2 \to m$ corresponds to take a section at $p_2 = m$, and the 3d Fermi arc is reduced to the 2d chiral edge mode.

3.4.2. Lattice system

Similarly, we consider the dimensional reduction of the lattice Hamiltonian of 3d WSM (13). In this case, we have two options,

$$p_1 \to m_1: \quad \mathcal{H}_{2d}^{(1)} = \sigma_1(\cos m_1 - \cos p_2 + c) + \sigma_2\sin p_2 + \sigma_3\sin p_3 \qquad (52)$$

$$p_2 \to m_2: \quad \mathcal{H}_{2d}^{(2)} = \sigma_1(\cos p_1 - \cos m_2 + c) + \sigma_2\sin m_2 + \sigma_3\sin p_3 \qquad (53)$$

and the corresponding spectra are given as follows:

$$\epsilon_1(p_2, p_3) = \pm\sqrt{(\cos m_1 - \cos p_2 + c)^2 + (\sin p_2)^2 + (\sin p_3)^2} \qquad (54)$$

$$\epsilon_2(p_1, p_3) = \pm\sqrt{(\cos p_1 - \cos m_2 + c)^2 + (\sin m_2)^2 + (\sin p_3)^2} \qquad (55)$$
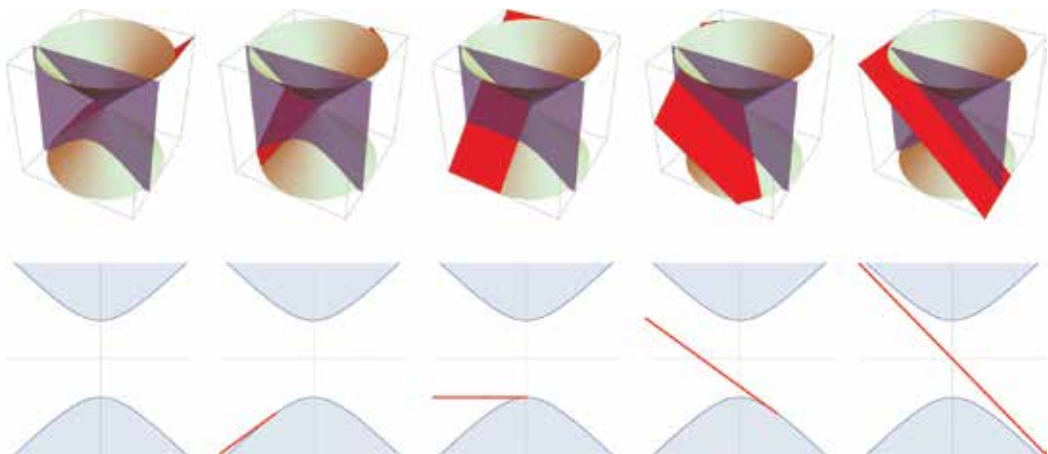

Figure 9. The boundary condition dependence of the edge state for the 2d system. The dimensional reduction corresponds to taking a section at $p_2 = m$. The horizontal axis in the bottom panel shows the momentum p_1.

We can follow the analysis discussed in Section 3.3.2 for the current system. **Figure 10** shows the boundary condition dependence of the edge state spectrum. These behaviors are consistent with the continuum model in the vicinity of the would-be gapless points. Such a dependence of the boundary condition has been recently predicted to be observed in monolayer silicene/germanene/stanene nanoribbons [19]. We remark that we obtain the edge state with positive and negative chiralities from the reduction $p_1 \to m_1$, which is equivalent to topologically trivial state. Actually the edge state is almost embedded, and indistinguishable with the bulk spectrum, in particular, for $\theta = 5\pi/7, 9\pi/7$. On the other hand, we obtain a single chiral edge state from the reduction $p_2 \to m_2$, indicating topologically nontrivial state. We can see an edge state spectrum survives for the whole region of the parameter θ.
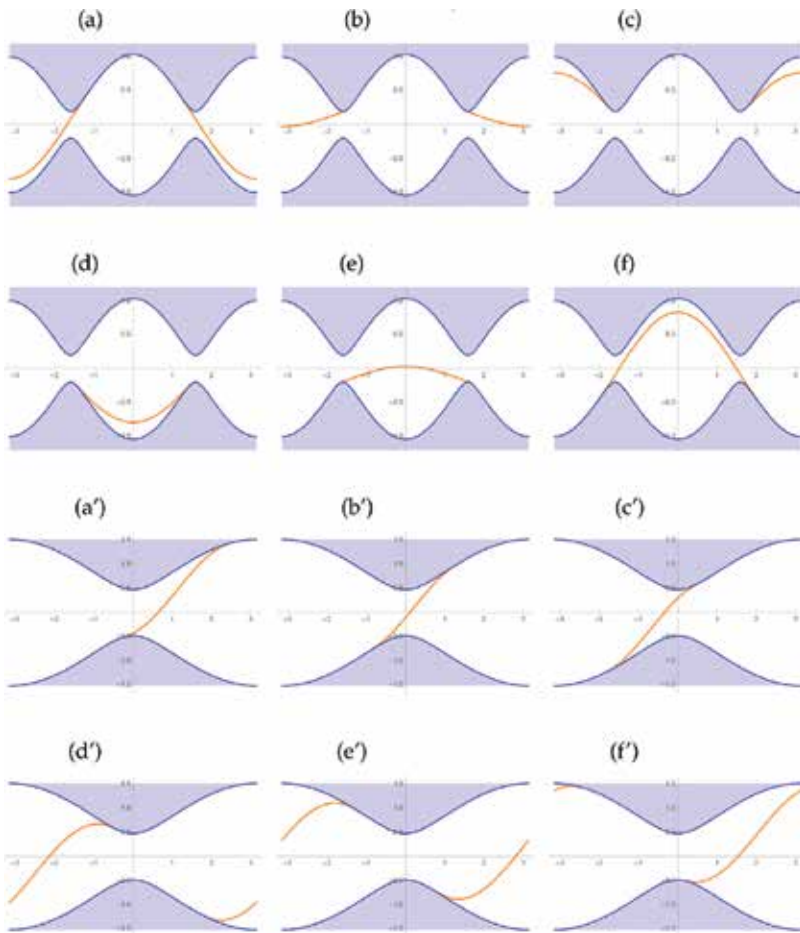

Figure 10. The boundary condition dependence of the 2d lattice system (52) and (53) with $c = 1$. (a)–(f) and (a′)–(f′) show the spectra obtained from the reduction $p_1 \to m_1 = \pi/2 + 0.5$ and $p_2 \to m_2 = 0.2$. The horizontal axes are the momenta p_2 and p_1, respectively. The blue region is the bulk, and the orange line is the edge state spectrum.

4. Edge-of-edge state

So far we have examined situations with a single boundary with the boundary condition. In general we can impose another boundary in the different direction, and a different boundary condition. In this section we consider a generic situation involving two boundaries with two different conditions. Then an intersection of two boundary plays a role of "edge-of-edge" and we study the corresponding edge-of-edge state localized on such an intersecting boundaries [4]. See also related works [20–24].

4.1. 5d Weyl semimetal

As discussed in Section 3.1, the boundary condition is characterized by the projection (23), so that the degrees of freedom of the boundary state should be a half of the original one. This implies that, if we impose two boundary conditions, we will have a quarter of the original d.o.f. Therefore, to obtain physical degrees of freedom at the edge-of-edge, we have to start with a four-component system or more. For this purpose, we start with the 5d WSM system discussed in Section 2.4 by introducing boundaries at $x_4 = 0$ and $x_5 = 0$. The boundary condition, namely the zero current condition (34), is now given by

$$\psi^\dagger \gamma_4 \psi \Big|_{x_4=0} = 0 \qquad \psi^\dagger \gamma_5 \psi \Big|_{x_5=0} = 0, \tag{56}$$

since the current operator is given by $J_\mu = \psi^\dagger \gamma_\mu \psi$. These conditions are rephrased as

$$P_4 \psi \Big|_{x_4=0} = 0 \quad P_5 \psi \Big|_{x_5=0} = 0 \quad \text{with} \quad P_{4,5} = \frac{\mathbb{1} - M_{4,5}}{2} \tag{57}$$

where the matrix $M_{4,5}$ obeys $M_a^\dagger \gamma_a + \gamma_a M_a = 0$ for $a = 4, 5$. Explicitly we have

$$M_5 = \begin{pmatrix} 0 & U_5^\dagger \\ U_5 & 0 \end{pmatrix}, \qquad M_4 = -\frac{1}{2}\begin{pmatrix} U_4 + U_4^\dagger & U_4 - U_4^\dagger \\ -U_4 + U_4^\dagger & -U_4 - U_4^\dagger \end{pmatrix}, \tag{58}$$

where $U_{4,5}$ are elements of U(2). A solution to these conditions localized at the boundary is given by

$$\psi\big(p_{1,2,3,5}, x_4\big) = e^{-\alpha_4(p)x_4}\begin{pmatrix} \mathbb{1} - U_4 \\ \mathbb{1} + U_4 \end{pmatrix}\chi\big(p_{1,2,3,4}\big), \quad \psi\big(p_{1,2,3,4}, x_5\big) = e^{-\alpha_5(p)x_5}\begin{pmatrix} \mathbb{1} \\ U_5 \end{pmatrix}\xi\big(p_{1,2,3,4}\big). \tag{59}$$

In particular, the edge state localized at $x_5 = 0$ is apparently similar to the 3d case (39), just replacing the phase factor $e^{i\theta} \in$ U(1) with $U_5 \in$ U(2). The eigenvalue equation $\mathcal{H}_{5d}\psi = \epsilon\psi$ leads to $\epsilon_5^2 + \alpha_5^2 = \left|\vec{p}\right|^2 + p_4^2$ and also

$$\left[(i\alpha_5 - \epsilon_5) + \left(p_4 - i \, \vec{\sigma} \cdot \vec{p} \right) U_5 \right] \xi = 0. \tag{60}$$

Decomposing $U_5 = e^{i\theta_5} V_5$ with $e^{i\theta_5} \in U(1)$ and $V_5 \in SU(2)$, we consider the SU(2) transformation $\left(p_4 - i \, \vec{\sigma} \cdot \vec{p} \right) V_5 = p_4' - i \, \vec{\sigma} \cdot \vec{p}'$. Then we have

$$\left(\alpha_5 \sin\theta_5 - \epsilon_5 \cos\theta_5 + p_4' \right)\xi = 0, \tag{61}$$

$$\left(\alpha_5 \cos\theta_5 + \epsilon_5 \sin\theta_5 - \vec{\sigma} \cdot \vec{p}' \right)\xi = 0. \tag{62}$$

Diagonalizing $\vec{\sigma} \cdot \vec{p}'$, which is equivalent to the 3d Hamiltonian (6), as $\left(\vec{\sigma} \cdot \vec{p}' \right)\xi_\pm = \pm\sqrt{\left|\vec{p}'\right|^2}\,\xi_\pm$, we obtain the spectrum and the inverse penetration depth as follows:

$$\epsilon_5(p) = p_4' \cos\theta_5 \pm \sqrt{\left|\vec{p}'\right|^2}\sin\theta_5, \qquad \alpha_5(p) = -p_4'\sin\theta_5 \pm \sqrt{\left|\vec{p}'\right|^2}\cos\theta_5, \tag{63}$$

which is written using an SO(2) transformation as before,

$$\begin{pmatrix} \epsilon_5 \\ \alpha_5 \end{pmatrix} = \begin{pmatrix} \cos\theta_5 & \sin\theta_5 \\ -\sin\theta_5 & \cos\theta_5 \end{pmatrix} \begin{pmatrix} p_4' \\ \pm\sqrt{\left|\vec{p}'\right|^2} \end{pmatrix}. \tag{64}$$

We can solve the boundary condition and obtain the spectrum for the boundary at $x_4 = 0$ in a similar way.

Let us then consider a compatible boundary condition for the localized edge-of-edge state

$$P_4\psi\Big|_{x_{4,5}=0} = P_5\psi\Big|_{x_{4,5}=0} = 0. \tag{65}$$

A solution to this condition is given by

$$\psi\left(p_{1,2,3}, x_4, x_5\right) = e^{-\alpha_4(p)x_4 - \alpha_5(p)x_5}\begin{pmatrix} \mathbb{1} - U_4 \\ \mathbb{1} + U_4 \end{pmatrix}\chi(p) \tag{66}$$

with $[U_5(\mathbb{1} - U_4) - (\mathbb{1} + U_4)]\chi(p) = 0$, which is covariant under U(2) transformation $(U_4, U_5, \chi) \to (WU_4W^\dagger, WU_5W^\dagger, W\chi)$ with $W \in U(2)$. To have a nontrivial solution, they should obey $[U_5(\mathbb{1} - U_4) - (\mathbb{1} + U_4)] = 0$. For example, a simple choice is $(U_4, U_5) = (\sigma_3, \sigma_2)$, and the corresponding solution is $\chi^T = (1 \ i)$. Then we obtain the spectrum of the edge-of-edge state $\epsilon(p) = -p_1$, $\alpha_4(p) = p_3$, $\alpha_5(p) = p_2$.

4.2. 3d chiral topological insulator

We discuss dimensional reduction of the edge-of-edge state in the 5d WSM to a more realistic 3d system. Replacing $(p_4, p_5) \to (m, 0)$ as shown in **Figure 11**, then we obtain the 3d chiral (class AIII) TI

$$\mathcal{H}_{3d}^{AIII}\left(\vec{p}\right) = \vec{p} \cdot \vec{\gamma} + m\gamma_4, \tag{67}$$

where the gamma matrices are chosen as $\vec{\gamma} = \tau_2 \otimes \vec{\sigma}$, $\gamma_4 = \tau_1 \otimes \mathbb{1}$, $\gamma_5 = \tau_3 \otimes \mathbb{1}$, and Pauli matrices $\sigma's$ and $\tau's$ act on the spin space $(\uparrow, \downarrow)$ and the sublattice space (A, B), respectively. This Hamiltonian has a chiral symmetry with respect to the sublattice structure $\{\mathcal{H}_{3d}^{AIII}, \gamma_5\} = 0$. We can apply a similar analysis as before. The edge-of-edge state is in this case given by

$$\psi(p_1, x_2, x_3) = e^{-\alpha_2(p_1)x_2 - \alpha_3(p_1)x_3} \begin{pmatrix} \mathbb{1} + i\sigma_3 U_3 \\ i\sigma_3(\mathbb{1} - i\sigma_3 U_3) \end{pmatrix} \xi(p_1) \tag{68}$$

with the compatibility condition

$$\det\left[\mathbb{1} + U_2^{\dagger}(i\sigma_2) + i\sigma_3 U_3 - U^{\dagger}(i\sigma_1)U_3 + i\sigma_1 - i\sigma_2 U_3 - U_2^{\dagger}(i\sigma_3) - U_2^{\dagger}U_3\right] = 0 \tag{69}$$

where $U_{2,3} \in$ U(2) parameterize the boundary condition. We consider the following choice satisfying the compatibility condition $U_2 = \sigma_2 \cos\phi + i\sin\phi$, $U_3 = i\cos\phi - \sigma_3 \sin\phi$. Then we obtain the spectra of the edge state localized at $x_2 = 0$ and x_3, and the edge-of-edge state localized at their intersection

$$\epsilon_2(p_1, p_3) = \pm\sqrt{p_1^2 + p_3^2 + (m\cos\phi)^2}, \tag{70}$$

$$\epsilon_3(p_1, p_2) = \pm\sqrt{p_1^2 + p_2^2 + (m\sin\phi)^2}, \tag{71}$$

$$\epsilon_{eoe}(p_1) = -p_1. \tag{72}$$

Here both edge states are gapped, while only the edge-of-edge state is gapless. This is a suitable situation for experimental detection of the edge-of-edge state because we have to distinguish it from the spectra of the edge states at $x_2 = 0$ and $x_3 = 0$. The reason why we obtain the gapped edge states seems that the symmetry protecting the edge state is weakly broken due to the boundary condition, which is analogous to the TI/ferromagnet junction, etc.
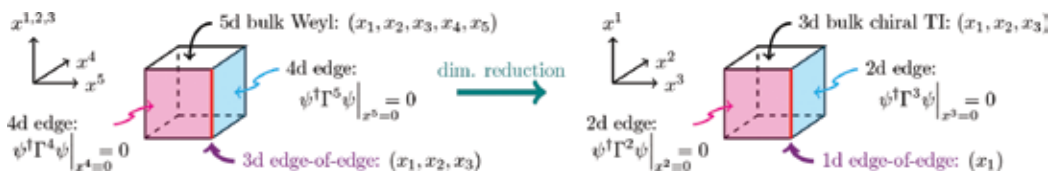

Figure 11. Dimensional reduction from 5d WSM to 3d chiral TI. There exists the edge-of-edge state localized at the boundary intersection, propagating in x_1-direction.

Acknowledgements

Author details

Taro Kimura

Address all correspondence to: taro.kimura@keio.jp

Department of Physics, Keio University, Japan

References

[1] Hasan MZ, Kane CL. Topological insulators. Reviews of Modern Physics. 2010;**82**:3045

[2] Wen X-G. Quantum Field Theory of Many-Body Systems: From the Origin of Sound to an Origin of Light and Electrons. Oxford: Oxford University Press; 2004

[3] Hashimoto K, Kimura T, Wu X. Boundary conditions of Weyl semimetals. Progress of Theoretical and Experimental Physics. 2017;**2017**:053I01

[4] Hashimoto K, Kimura T, Wu X. Edge states at an intersection of edges of a topological material. Physics Review. 2017;**B95**:165443

[5] Devizorova ZA, Volkov VA. Fermi arcs formation in Weyl semimetals: The key role of intervalley interaction. Physics Review. 2016;**B95**:081302(R)

[6] Enaldiev VV, Zagorodnev IV, Volkov VA. Boundary conditions and surface states spectra in topological insulators. JETP Letters. 2015;**101**:89-96

[7] Isaev L, Moon YH, Ortiz G. Bulk-boundary correspondence in three-dimensional topological insulators. Physics Review. 2011;**B84**:075444

[8] Kitaev AY. Periodic table for topological insulators and superconductors. AIP Conference Proceedings. 2009;**1134**:22-30

[9] Schnyder AP, Ryu S, Furusaki A, Ludwig AWW. Classification of topological insulators and superconductors in three spatial dimensions. Physics Review. 2008;**B78**:195125

[10] Chruściński D, Jamiołkowski A. Geometric phases in classical and quantum mechanics. In: Progress in Mathematical Physics. Vol. 36. Boston: Birkhäuser; 2004

[11] Thouless DJ, Kohmoto M, Nightingale MP, den Nijs M. Quantized Hall conductance in a two-dimensional periodic potential. Physical Review Letters. 1982;**49**:405-408

[12] Hashimoto K, Kimura T. Band spectrum is D-brane. Progress of Theoretical and Experimental Physics. 2016;**2016**:013B04

[13] Kimura T. Domain-wall, overlap, and topological insulators. PoS Lattice. 2016;**2015**:042

[14] Golterman MFL, Jansen K, Kaplan DB. Chern-Simons currents and chiral fermions on the lattice. Physics Letters. 1993;**B301**:219-223

[15] Nielsen HB, Ninomiya M. Absence of neutrinos on a lattice. 1. Proof by Homotopy theory. Nuclear Physics. 1981a;**B185**:20-40

[16] Nielsen HB, Ninomiya M. Absence of neutrinos on a lattice. 2. Intuitive topological proof. Nuclear Physics. 1981b;**B193**:173-194

[17] Hashimoto K, Kimura T. Topological number of edge states. Physics Review. 2016b;**B93**: 195166

[18] Witten E. Three lectures on topological phases of matter. La Rivista del Nuovo Cimento. 2016;**39**:313-370

[19] Hattori A, Tanaya S, Yada K, Araidai M, Sato M, Hatsugai Y, Shiraishi K, Tanaka Y. Edge states of hydrogen terminated monolayer materials: Silicene, germanene and stanene ribbons. Journal of Physics: Condensed Matter. 2017;**29**:115302

[20] Benalcazar WA, Bernevig BA, Hughes TL. Electric multipole moments, topological pumping, and a chiral hinge insulator. Physics Review. 2017;**B96**:245115

[21] Benalcazar WA, Bernevig BA, Hughes TL. Quantized electric multipole insulators. Science. 2017;**357**:61-66

[22] Langbehn J, Peng Y, Trifunovic L, von Oppen F, Brouwer PW. Reflection-symmetric second-order topological insulators and superconductors. Physical Review Letters. 2017; **119**:246401

[23] Schindler F, Cook AM, Vergniory MG, Wang Z, Parkin SSP, Bernevig BA, Neupert T. Higher-Order Topological Insulators. 2017;arXiv:1708.03636

[24] Song Z, Fang Z, Fang C. (d-2)-dimensional edge states of rotation symmetry protected topological states. Physical Review Letters. 2017;**119**:246402

Spin-Helical Dirac Fermions in 3D Topological Insulator Quantum Wires

Romain Giraud and Joseph Dufouleur

Additional information is available at the end of the chapter

Abstract

The next generation of electronic devices based on 3D topological insulators will be developed from advanced functional nanostructures and heterostructures. Toward this goal, single-crystalline nanowires offer interesting opportunities for new developments due to the strong quantum confinement of spin-helical surface Dirac fermions and to the possibility to realize core-shell lateral nanostructures adapted to the control of the electro-chemical potential at the interface with a topological insulator. Here, we review the specific transport properties of 3D topological insulator quantum wires and the influence of disorder. Having a large energy quantization, weakly-coupled Dirac surface modes are prone to quasi-ballistic transport, with some analogies to carbon nanotubes but with spin-textured quantum states weakly coupled by non-magnetic disorder. Due to a small interaction with their environment, these surface modes are good candidates to realize novel quantum spintronic devices, spanning from ballistic spin conductors to localized spin filters. A specific topological mode also holds promises to control chiral edge states and Majorana bound states in truly 1D quantum wires, being tunable with a magnetic field or an electrical gate. Challenges toward these goals are briefly discussed, as well as the need for novel functional heterostructures.

Keywords: 3D topological insulators, nanostructures, quantum confinement, Dirac fermions, spin transport, disorder, core-shell heterostructures

1. Introduction

The topology of electronic band structures in crystals can have profound consequences at their interfaces with materials having a trivial topology, resulting in novel electronic states in reduced dimension [1, 2]. A striking example is the realization of gapless metallic states with a Dirac band

structure at the interface between two insulators, if one is a topological insulator (TI). For a 2D crystal, these are dissipationless 1D spin-helical edge states, an electronic phase known as the quantum spin Hall state [3–5]. For a 3D crystal, the metallic phase develops as 2D surface/inter-face states [6, 7] with a spin-helical band structure that limits their scattering by non-magnetic disorder [8]. This novel type of insulators was discovered in materials having a strong spin-orbit coupling (broken rotational symmetry) and a Hamiltonian invariant by time-reversal symmetry (TRS), belonging to the so-called $\mathbb{Z}2$ topological class [7, 9]. The spin-orbit interaction can lead to a band inversion that gives rise to novel quasi-particles having a Dirac-like band structure with spin-momentum locking, at the interface with a trivial insulator (i.e., with non-inverted bands) where the energy gap must close (see **Figure 1a**). A remarkable property is that such metallic states always exist (no gap), even in the presence of perturbations, as long as the main symme-tries are preserved. Thus, regardless the strength of a non-magnetic disorder, the condition for strong (Anderson) localization is never fulfilled. Still, an electronic gap (an important property for the operation of classical electronic devices) can be created, for instance by using a perturba-tion breaking TRS or by coupling topological states at opposite interfaces. The non-trivial nature of such gapped topological states further gives rise to novel exotic phases with a lower dimen-sion (Majorana bound states [10] and quantum anomalous Hall state [11]) of particular interest for the quantum manipulation of coherent states weakly coupled to their environment.

The importance of topological insulators also comes from that they represent a promising alternative to conventional semi-conducting hetero-structures with, in principle, a reduced complexity on the materials' side and an increased stability of their electronic phases (over a large range of physical parameters: temperature, magnetic field, chemical potential, and disorder/inhomogeneities). The most striking example came with the discovery of the quan-tum spin Hall edge states in a 2D topological insulator, first evidenced with HgCdTe quan-tum wells [12]. This novel electronic phase shares some similarities with the magnetic-field induced integer quantum Hall state in high-mobility low-density 2D electron gases (2DEGs) of massive quasi-particles but was predicted in zero field [3, 4, 13] (no magnetic-field induced

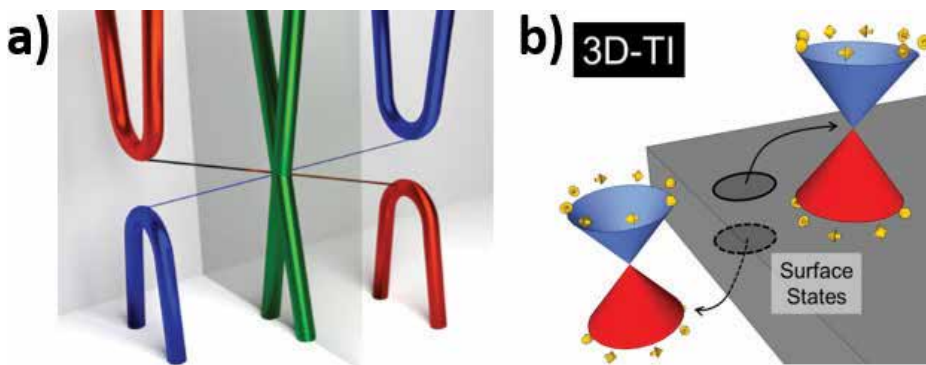**Figure 1.** (a) Evolution of the band gap between a trivial insulator and a 3D topological insulator (with an inverted bulk band structure). At the interface, the gap closes and metallic states with a linear dispersion form. (b) These interface/surface states are 2D spin-helical Dirac fermions, with opposite spin helicity for opposite surfaces (the simplest case of a single Dirac cone in the center of the Brillouin zone is sketched).

orbital effect). Another important discovery was that of 3D topological insulators [14–16], which realize a 2D electron gas of massless Dirac fermions (different from those in graphene due to their helical spin texture) at the surfaces/interfaces of a *single* crystalline film (**Figure 1b**), whereas the creation of a charge-accumulation 2D gas of massive quasi-particles in conventional semiconductors often requires a more complex stacking of epitaxial layers of materials with different energy gaps and electronic-band offsets. In practice, the control of surface electronic states in a 3D topological insulator also requires that of band bending at interfaces (due to charge transfer from the environment) and a significant limitation to investigate topological surface-state transport came from that most materials are not true bulk insulators. Still, an important difference with massive quasi-particles in semiconductors, or Dirac fermions in graphene, is the reduced scattering rate by disorder due to the spin-helical texture of surface Dirac fermions [8, 17]. This favors the quasi-ballistic transport of such quasi-particles, even if they directly coexist with a large density of scattering centers, and it gives a new possibility to study such a transport regime [18] that is otherwise only accessible for massive quasi-particles in rather high-mobility AlGaAs 2DEGs (for which the 2DEG is spatially separated from Coulomb scatterers). Besides, the spin-momentum locking property of the Dirac cone favors the efficient spin-charge conversion in spintronic devices [19–25], still with some potential for improvement due to the enhanced transport length [17], if interface scattering could be further reduced.

Contrary to the case of 2D TIs, with only rare examples found to date, a number of 3D TI materials were discovered, both by theory and experiments, often using ab initio calculations or electron spectroscopy techniques to directly unveil the Dirac band structure of topological surface states (TSS). This offered an important playground to investigate [26, 27], but it is also a source of confusion due to the diversity of these materials and the complexity of some of them. In particular, their study by charge transport measurements proved to be difficult because many materials identified as topological insulators are also semiconductors with a rather small gap, often with a large finite bulk conductivity due to disorder (electrical doping) and a strong electronic polarizability [28]. The search for large-gap 3D topological insulators remains challenging. Indeed, beyond the need for specific symmetries of the crystal structure, it is fundamental to search for materials with a band inversion. With conventional semiconductors, this inversion is usually induced by a strong intrinsic spin-orbit coupling. This is typical for materials with large-Z elements, which also have a rather small bulk energy gap induced by Coulomb interactions. This combination is therefore favorable to realize a band inversion, and since it results from opposite contributions, most Z2 topological insulators tend to have a rather small gap that barely exceeds 300 meV in most cases. Natural point defects, such as vacancies (which are thermodynamically stable and therefore always exist in crystals), can be massively present (small activation energy) and they often act as donors or acceptors, thus easily leading to metallic-like bulk properties typical of degenerate semiconductors (sometimes approaching the dirty-metal limit). Among these semiconductors, Bi-based chalcogenides play an important role for that the continuous tuning of their chemical composition, between different stoichiometric compounds, can change a trivial insulator (no band inversion) into a topological insulator (band inversion), with a varying bulk gap and a relative change of the topological Dirac degeneracy point with respect to the bulk band structure [29]. Binary 3D topological insulators, such as Bi_2Se_3 and Bi_2Te_3, usually have a large residual

bulk conductivity (despite a very small bulk-carrier mobility), so that the total conductance of wide and/or thick nanostructures is dominated by bulk transport. This contribution is slightly reduced in Bi_2Te_3, but only high-energy surface quasi-particles can be studied because the Dirac point lies deep into the valence band, whereas the Fermi level is pinned near or above the top of the valence band. In Bi_2Se_3, the Dirac point lies within the bulk band gap, but the Fermi level is high above the bottom of the conduction band (due to too many Se vacancies), so that it can only be modified over a small energy range by an electrical gate (efficient electrostatic screening), unless the nanostructure is ultra thin. Ternary compounds gave the most advanced results to optimize the surface-to-bulk ratio to the conductance and this approach was successfully used to investigate surface-state transport in the quantum Hall regime at low magnetic fields (close to the Dirac point) [30]. It remains, however, difficult to prepare nanostructures (thin films, nanoribbons, and nanowires) of ternary or even quaternary materials with optimized compositions [31]. Novel heterostructures, such as core-shell nanowires, could thus be important to develop functional devices based on 3D topological insulators, not only to achieve dominant surface transport and use the spin-momentum locking property of 2D topological surface states, but also to realize novel low-dimensional quantum devices at the sub-micron scale despite disorder, due to anisotropic scattering, which are different from "conventional" mesoscopic conductors with either massive quasi-particles in semiconductors or Dirac fermions in graphene (both with quantum transport properties controlled by large-angle scattering).

Unique properties of spin-helical Dirac fermions in disordered 3D topological insulators also arise from their strong quantum confinement in narrow nanowires (quantum wires). The Dirac nature results in a large energy quantization, as compared to the confinement energy of massive quasi-particles, which further reduces their scattering by disorder and favors the quasi-ballistic transport of quasi-1D surface modes [18]. Thus, their quantized band structure gives some specific signatures of topological surface-state transport, unveiled by quantum corrections to the conductance [18, 32, 33], which can be easily distinguished from bulk transport (even for highly-degenerate semiconductors, such as Bi_2Se_3 and Bi_2Te_3). Their spin texture also contribute to reduce their coupling to the environment, so that decoherence due to electronic interactions is also further reduced. All in all, 3D topological insulator quantum wires offer new possibilities to investigate mesoscopic transport in the quasi-ballistic regime over a large range of parameters (dimensionality, aspect ratio, and disorder strength), whereas it can hardly be investigated otherwise. Rare studies based on high-mobility AlGaAs 2DEGs were limited to the near-clean limit [34, 35], with little possibilities to modify some important physical parameters, such as disorder or the kinetic energy, over a broad range. Disordered semiconducting or metallic nanowires are always diffusive conductors. Disordered semiconducting or metallic nanowires are always diffusive conductors. Most similar systems are actually carbon nanotubes, which are clean systems with ballistic-transport properties and very large confinement energies. Disordered 3D TI quantum wires represent an intermediate situation that corresponds to quasi-ballistic transport (due to anisotropic scattering rather than to a weak disorder) and their quantized surface states can be manipulated with rather small magnetic fields, due to larger diameters than for carbon nanotubes. As a consequence, the specific properties of quantized surface Dirac modes can be revealed by the study of different quantum corrections to the conductance (Aharonov-Bohm oscillations and non-universal conductance fluctuations), with good statistical information obtained from magneto-transport measurements below 15 T [18].

2. Transport properties of 2D topological surface states

To understand the physics of 3DTI quantum wires, it is first necessary to take a closer look at the scattering of 2D spin-helical Dirac fermions by a non-magnetic disorder. In this case, backscattering is not suppressed since it remains possible by successive small-angle scattering events, over a scale given by the transport length, l_{tr}. However, the spin texture favors forward scattering, so that the transport length of topological surface state is largely enhanced with respect to the disorder correlation length. As a consequence, the condition for ballistic transport can already be realized in nanostructures with dimensions smaller than a micron, and quantum devices with a simple geometry can be built from individual nanowires.

2.1. Nanostructures of 3D topological insulators for surface-transport studies

Due to their residual bulk doping, the study of surface-state transport in disordered 3D topological insulators is not straightforward. Considering the case of a highly-degenerate semiconductor, such as Bi_2Se_3, with a bulk carrier density as high as $5 \cdot 10^{19}$ cm^{-3} (which roughly corresponds to about 1% of Se vacancies, acting as double donors), the cross over thickness t_c for which the surface conductance becomes comparable to the bulk conductance is roughly given by $t_c = 2(n_s\mu_s)/(n_b\mu_b)$. For a strong disorder typical for Bi_2Se_3, common to both surface and bulk states, the mobility of topological surface states is about one order of magnitude larger than that of bulk states (enhancement due to the anisotropic scattering of spin-helical Dirac fermions) [17]. Taking band bending into account [36], typical values for the surface and bulk carrier densities are $n_s = 5 \cdot 10^{12}$ cm^{-2} and $n_b = 5 \cdot 10^{19}$ cm^{-3}. This gives a value $t_c = 20$ nm. Based on a realistic approximation (ignoring details of band bending due to a very short Thomas-Fermi screening length $\lambda_{TF} \lesssim 3$ nm), this lower bound for t_c (which is likely be larger for smaller bulk carrier densities) clearly shows that the control of topological surface-state transport in disordered 3D TIs requires the use of thin nanostructures. These were successfully grown by different bottom-up methods, each technique having both advantages and disadvantages. Ultra-thin layers of high quality can be prepared by molecular beam epitaxy and are well adapted to tune the interface band structure by electrical fields, but films thicker than 20 nm tend to grow 3D and have more defects. High-quality single-crystalline nanostructures with large aspect ratios can be grown by catalyst-assisted molecular-beam epitaxy or chemical vapor deposition, as well as by catalyst-free vapor transport, but ultra-thin structures are seldom. Very narrow quantum wires can also be prepared by electrodeposition in nanomembranes, presently with some intrinsic limitations related to small diameter fluctuations in ultimate nanomembranes that give quantum confinement inhomogeneities. In all cases, individual nanostructures stable in air can be randomly grown on or transferred onto SiO_x/Si substrates, appropriate to create an electric field at the interface by applying a backgate voltage.

In our work, we mostly investigated the charge transport properties of *single-crystalline atomic-flat Bi_2Se_3 and Bi_2Te_3 nanostructures* grown by catalyst-free vapor transport (**Figure 2a**), with *faceted* shapes of different aspect ratios (nanoplatelets, nanoribbons, nanowires; **Figure 2b**) [37]. As explained below, this allowed us to study the physics of spin-helical Dirac fermions in 2D or in 1D, that is, without or with quantum confinement, respectively. Despite strong disorder, it was shown that momentum scattering is reduced in all cases, due to the spin texture (2D surface states) and quantum confinement (1D surface modes). This has important consequences for both spin transport and quantum coherent transport, as discussed in detail below.
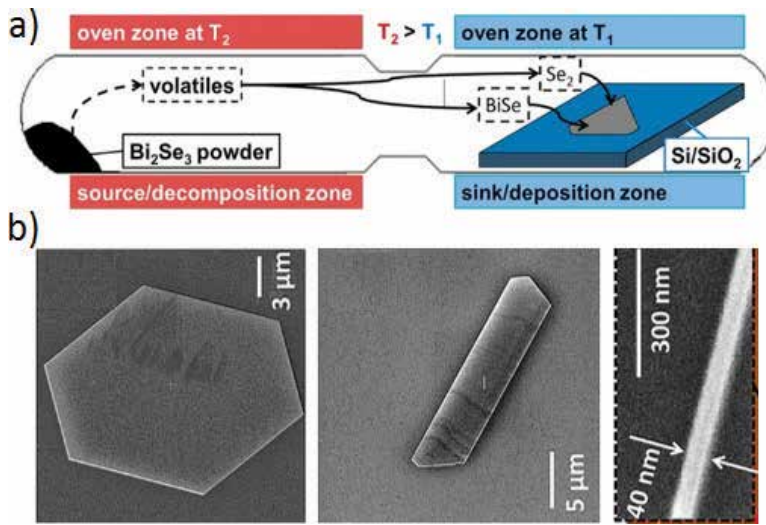
Figure 2. (a) Growth of Bi_2Se_3 nanostructures on p++-Si/SiO$_2$ substrates by vapor transport in a closed quartz ampoule. The sublimation of Bi_2Se_3 crystals generates a flow of molecular species (BiSe and Se$_2$) toward the lower temperature area, where the recombine to form single crystalline nanostructures *in the plane* of the substrate. (b) Nanostructures with different aspect ratios (thin platelets, wide nanoribbons, and narrow nanowires) are distributed randomly onto amorphous SiO$_2$. After [37].

2.2. Band bending and interface charge transfers

The electrical properties of 2D topological surface states can be investigated by quantum magneto-transport G(B) studies and transconductance G(Vg) measurements at low temperatures, which give access to all microscopic parameters (carrier density, mobility, and effective mass) for all carriers (topological interface states, topological surface states, and bulk states). A careful analysis of Shubnikov-de Haas oscillations due to the energy quantization of Landau levels in high magnetic fields gave detailed insights into the electronic band profiles in the thickness of wide Bi_2Se_3 nano-structures (nanoplatelets and nanoribbons) [36]. Important results are summarized as follows:

1. Due to the large residual bulk density and the pinning of the Fermi energy in the conduction or valence band of materials with a large dielectric constant, the bulk contribution to the conductance is never negligible.

2. Besides, it usually controls the upward band bending at interfaces of the topological insulator (charge transfer of bulk carriers to empty gapless topological surface states).

3. Downward band bending can, however, exist if a massive charge transfer from another origin is also present (surface/interface disorder, surface adsorbents, and electrostatic gate). Such a situation is more likely to happen for materials with a small bulk carrier density.

4. If the surface/interface density is very large (typically for $n_s > 10^{13}$ cm^{-2}), a Rashba charge-accumulation 2DEG of massive quasi-particles coexist with Dirac topological states.

For usual as-grown Bi_2Se_3 nanostructures exposed to air, a typical band profile is defined from the contribution of three electronic populations (bulk carriers and two topological states with

different Fermi energies), and the bulk carrier density is large enough to control charge transfer at interfaces and to induce upward band bending. Due to efficient Coulomb screening, an electrostatic gate is solely influencing the population of a single topological interface nearby, so that an independent tuning of both topological states is only achieved in dual-gate devices [38]. In a backgate geometry, the applied voltage is modifying the band bending at the bottom interface only, which results in the tuning of the electro-chemical potential of the interface topological states but not of the surface topological states since, in most cases, the electrical field is totally screened by bulk carriers nearby the bottom interface [17]. In all cases, the backgate-voltage dependence of the conductance nevertheless remains an efficient way to probe the interface topological states and study their properties by transport measurements. A striking example is shown in **Figure 3**, for a rather thick Bi_2Se_3 nanoribbon patterned in a Hall-bar geometry, with a low-enough bulk-carrier density to favor downward band bending at interfaces [36]. For a large interface carrier density, massless Dirac fermions coexist with a Rashba-type massive 2D electron gas. In this case, the back-gate voltage is changing the carrier concentration of different electronic states located at the bottom interface (shift of some peaks in the Fourier transform of Shubnikov de Haas oscillations, **Figure 3b**). The related band profile shown in **Figure 3c** is in very good quantitative agreement with a triangular potential at this interface.

2.3. Anisotropic scattering and charge transport length (=spin diffusion length)

Further important information on the scattering of spin-helical Dirac fermions by a non-magnetic disorder can be obtained from transconductance $G_{(V\_G)}$ measurements [17]. It is indeed important to distinguish between two different scattering times and, accordingly, between two different length scales (**Figure 4a**):

1. The quantum lifetime of quasi-particles can be inferred from Shubnikov-de Hass measurements. It is associated with the mean-free path l_e between two successive scattering centers (thus to the microscopic disorder correlation length) and this momentum scattering time relates to the quantum mobility.

2. The transport time of carriers corresponds to the timescale for momentum backscattering, over a length called the transport length L_{tr}, related to the transport mobility, which determines the classical conductance. Whereas direct backscattering is forbidden by spin-momentum locking (giving dissipationless states in a 2D TI), it is allowed by multiple scattering processes in a disordered 3D TI, resulting in a finite transport length.

Using a thin Bi_2Se_3 nanoribbon (**Figure 4b**), the backgate voltage allowed us to modify the upward band bending, induced by a rather large bulk carrier density, at the bottom interface ("lower surface state", LSS). All microscopic transport parameters could be inferred from quantum magneto-transport (**Figure 4c**) and trans-conductance (**Figure 4d**) measurements [17]. Contrary to bulk carriers, for which $l_e \sim L_{tr}$ is given by the disorder correlation length ξ (isotropic scattering due to a short-range disorder potential), the transport length of both upper and lower topological surface states was found to be much larger than the mean-free path, despite a limitation at about 200 nm probably due to the finite coupling with bulk carriers [larger values are expected for decoupled topological states and/or in materials with a larger disorder correlation length, such as Bi_2Te_3].
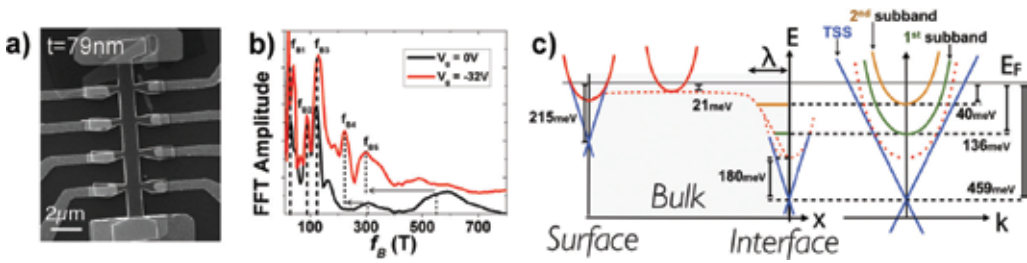
Figure 3. (a) Scanning-electron microscope image of a Hall-bar patterned Bi_2Se_3 thick nanoribbons, (b) fast-Fourier transform of the longitudinal magneto-resistance for two different back-gate voltages, and (c) evolution of the electronic band profile from the top surface to the bottom interface, typical for a low bulk-carrier density (downward band bending) and a large interface carrier density (coexistence of topological states with a Rashba 2DEG). After [36].
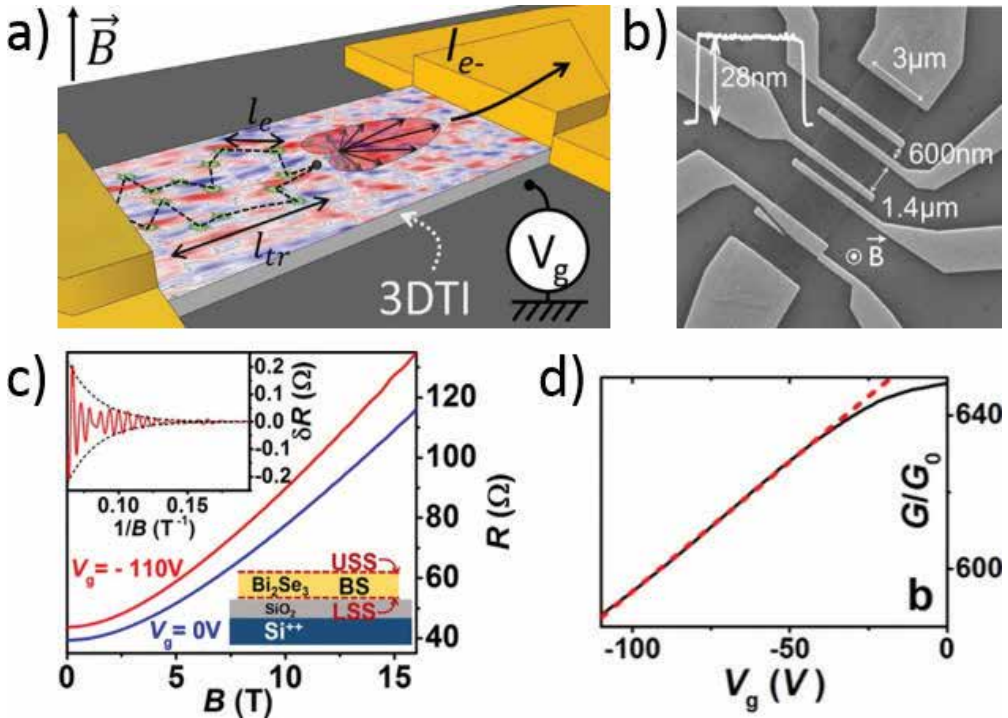

Figure 4. (a) Anisotropic scattering by disorder. The backscattering transport length L_{tr} can be much longer than the mean-free path l_e; (b) scanning electron microscope image of a thin Bi_2Se_3 nanoribbon with traversing ohmic contacts; (c) longitudinal magneto-conductance for two different backgate voltages. Inset: Shubnikov-de Haas quantum oscillations; (d) backgate voltage dependence of the conductance and linear fit from which the transport length of the lower surface states (bottom interface) is inferred. After [17].

The average number of scattering centers involved in a backscattering process is directly related to the ratio L_{tr}/l_e, and it can give some important information on the nature of both the scattering potential and the quasi-particles. Importantly, we revealed the long-range nature of disorder for spin-helical surface Dirac fermions, due to efficient electrostatic screening and

spin-momentum locking, which results in strongly anisotropic scattering, as observed by local probe microscopy. This means that forward scattering is favored for such quasi-particles and that the transport length is strongly enhanced ($L_{tr} \gg l_e$), as predicted by theory [8] and confirmed by trans-conductance measurements [17]. Such a situation never happens in other materials within which charge carriers directly coexist with disorder (including Dirac fermions in graphene), where the scattering of quasi-particles by any kind of disorder is isotropic (that is, $L_{tr} \sim l_e$). Only high-mobility AlGaAs 2DEGs can realize such a situation of anisotropic scattering. In this case, however, this is due to the spatial separation of free carriers and localized ionized donors, and it is not possible to vary the degree of disorder over a wide range, so that there is little room to investigate quasi-ballistic transport (in other words, the transition from ballistic to diffusive transport is rather abrupt and happens already when a small amount of impurities are introduced in the system). This is not the case for spin-helical Dirac fermions, and this property is at the origin of their unique transport properties, particularly in nanostructures, with an extended range of parameters to study quasi-ballistic transport, and therefore the ballistic-to-diffusive crossover in mesoscopic conductors.

This enhanced transport length for topological surface states is also important for spin transport studies, as it gives a lower limit for the size of functional spintronic devices making use of the spin-momentum locking property. Indeed, due to the strong spin-orbit coupling, there is a direct correspondence between the momentum-backscattering transport length and the spin relaxation length. With wide Bi_2Se_3 nanostructures, this scale is rather short (~200 nm), [17] so that, for instance, lateral spin valves could only be realized in the short-junction limit. This also shows that the true potential for the spin-to-charge conversion in highly-disordered Bi_2Se_3 could still give an improvement in the conversion efficiency by two orders of magnitude with respect to state-of-the-art records, with an inverse Edelstein length l_{IEE} determined by the intrinsic transport length of the 3D topological insulator, whereas it presently remains limited by the spin/momentum relaxation below metallic ohmic contacts (with $l_{IEE} \sim 2$ nm).

2.4. Dimensionalities of transport

The enhancement of the transport length for topological surface states also has two fundamental consequences for the quantum transport properties of 3D TI nanostructures and the dimensionality of surface charge transport:

1. The phase coherence length of TSS is also enhanced in the same ratio for diffusive 2D surface states in nanoplatelets or wide nanoribbons, so that mesoscopic transport can be studied in rather wide and long conductors (well beyond the micron size), despite relatively strong disorder. Since $L_\varphi \gg L_{tr}$ (L_φ being determined by inelastic scattering), quantum corrections to the conductance due to diffusive phase-coherent transport can thus be revealed by magneto-transport measurements with magnetic fields as small as 100 mT.

2. The condition for ballistic transport in the transverse motion of surface carriers along the perimeter is more restrictive ($L_p < 2 L_{tr}$), but it can be fulfilled for rather long ($L_p \sim 500$ nm), and therefore with nanostructures having a large cross section ($S \sim 0.2$ μm^2). Contrary to the case of carbon nanotubes, magnetic flux-dependent periodic phenomena in these *quantum wires* (such as the Aharonov-Bohm interference) can therefore be studied in rather small fields, below 1 T.

In the case of highly-disordered Bi_2Se_3 nanostructures ($l_e \sim 30$ nm), large values of L_{tr} (>200 nm) [17] and of L_φ (>2 μm) [39] were found. This implies that the dimensionality of surface-state transport is reduced in narrow nanostructures (mostly nanowires) and that their band structure is modified due to quantum confinement (which even further reduces the scattering by disorder). It thus becomes important to distinguish between three different situations for the dimensionality of charge transport:

1. No quantum confinement [L_{tr} is shorter than every dimensions]. Surface-state transport is diffusive and quasi-particles are 2D spin-helical Dirac fermions with a continuous spin-helical Dirac-cone band structure.

2. Transverse quantum confinement [the perimeter Lp becomes shorter than 2 L_{tr}]. Surface-transport is quasi-ballistic if the distance between contacts is longer than L_{tr} and ballistic otherwise. The length L remains much larger than L_{tr}, so that surface modes are quasi-1D channels in such *long* nanowires (becoming truly 1D only when they close).

3. Full quantum confinement [all dimensions are shorter than L_{tr}]. Spin-helical Dirac fermions are then fully localized in a *short* nanowire, which becomes a 0D quantum dot.

We remark that the dimensionality of quantum coherent transport is another quantity determined by comparing the dimensions of a mesoscopic conductor to the phase coherent length L_φ. Since L_φ is longer than L_{tr}, nanoribbons with a width W, such as $L_{tr} < W < L_\varphi$, have 2D spin-helical surface Dirac fermions but quantum coherent transport is 1D (which modifies the self-averaging of quantum interference in long conductors, for which the length L is longer than L_φ).

3. Transport properties of quasi-1D topological surface states

Signatures of the quasi-ballistic transport of topological surface states in 3D TI quantum wires can be revealed by the study of quantum corrections to the conductance. In a bulky nanostructure, spin-helical Dirac fermions propagate on the surface in a hollow-type electrical geometry, in analogy to carbon nanotubes (ballistic transport) or to the Sharvin-Sharvin metallic tubes (diffusive transport). Phase-coherent transport in the transverse direction (along the perimeter of the nanowire) thus gives rise to periodic Aharonov-Bohm oscillations in the longitudinal magneto-conductance, determined by a well-defined cross section $S = L_P^2/(4\backslash\varphi)$, and their observation in wide Bi_2Te_3 nanoribbons gave the first robust evidence of surface states by transport measurements [40]. Their topological nature was then confirmed by a study of decoherence at very low temperatures in narrow (quantum) nanowires [39], which revealed the unusual weak coupling to the environment and the ballistic motion in the transverse direction. Later, phase-coherent transport in the longitudinal direction was investigated in a study of conductance fluctuations [18], which revealed the subtle influence of disorder in the quasi-ballistic regime, leading to a non-universal behavior of quantum interference. A detailed understanding of the propagation of spin-helical 1D surface modes showed that both the spin texture of Dirac fermions and their quantum confinement are responsible for the weak scattering by disorder [41], thus leading to

the weak coupling between quantum states, a necessary condition for their manipulation by radio-frequency fields, as well as for the study of specific properties related to a single topologically-protected low-energy mode, such as 1D chiral edge states or Majorana bound states [42].

3.1. Quantum confinement: 1D Dirac spectrum

In quantum wires ($L_p < 2 L_{tr}$), the surface-state band structure is modified by periodic boundary conditions imposed in the transverse direction of the nanostructure, leading to the quantization of the transverse momentum $k_\perp$ (**Figure 5b**). This situation is equivalent to the energy quantization of quasi-particles confined into a quantum well with infinitely-high potential barriers, and for Dirac fermions, the transverse energy becomes quantized with a constant energy-level spacing $\Delta = h v_F 1/L_p$ between successive transverse modes. Due to the winding of the wave function along the perimeter (curvature) and to the spin-momentum locking of helical Dirac fermions, an additional Π Berry phase suppresses the topological protection of all energy modes in zero magnetic field (pairs of gapped states). However, if a magnetic field is applied along the nanowire axis, the Aharonov-Bohm flux modifies the periodic boundary condition (which gives an overall shift of transverse quantization planes, thus tuning the energy spectrum). Importantly, this flux dependence can restore the topological protection periodically when the Aharonov-
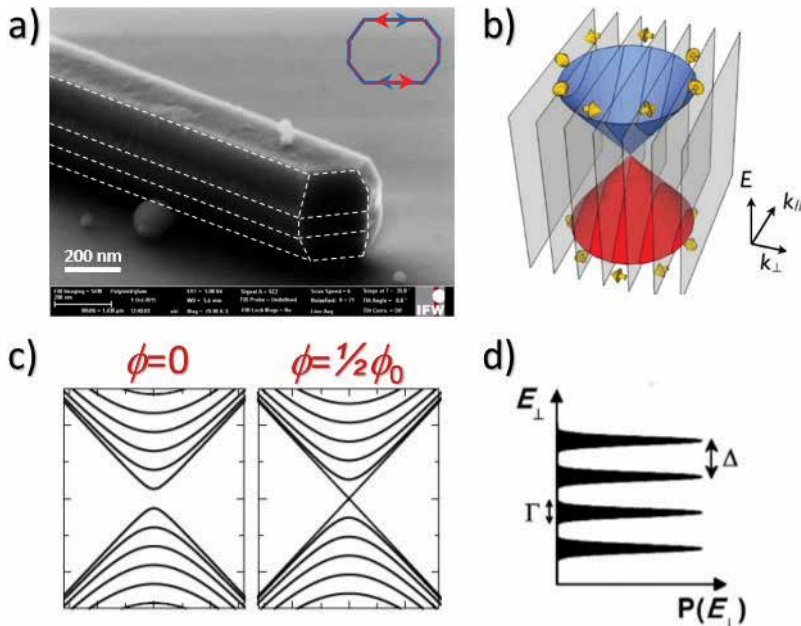

Figure 5. (a) Scanning electron microscope image of a narrow Bi_2Se_3 nanowire, with a perimeter Lp = 300 nm. Dashed lines separate different facets. Inset: schematics of the cross section and coherent winding of topological surface states; (b) transverse-impulse quantization planes intersecting the spin-helical Dirac cone. By applying a magnetic flux, all planes are continuously shifted in the $k_\perp$ direction; (c) resulting band structures for two different values of the magnetic flux ϕ. For $\phi = 0$, quantum confinement gives pairs of modes with a finite energy gap Δ. For $\phi = 1/2\phi_0$, a single topological mode with linear dispersion appears (quantization plane intersecting the Dirac point); (d) energy broadening Γ of the quantized transverse energy due to disorder [for 3DTI quantum wires, Γ is smaller than Δ, even for relatively strong disorder].

Bohm phase compensates the curvature-induced Berry phase, giving rise to a single gapless and linear mode with perfect transmission (**Figure 5c**), independent of disorder [43].

In recent years, a couple of interesting studies suggested the influence of such a topological mode on quantum transport properties, particularly the Aharonov-Bohm (AB) oscillations [32, 33, 44]. These results raised some important questions since it was not possible to give a quantitative interpretation of the physical phenomena observed (Aharonov-Bohm oscillations and non-universal conductance fluctuations) solely based on the contribution of this perfectly transmitted mode to the conductance. In particular, the amplitude of these quantum corrections to the conductance was always found much smaller than the conductance quantum G_0. It thus remained unclear whether these properties were a signature of a topological transition or were rather induced by all spin-textured modes, including dominant contributions from high-energy quasi-1D modes. Actually, the quantum magneto-conductance is mostly due to a limited number of modes, those partially-opened modes with a quantized transverse energy close to the Fermi energy. Since most studies were conducted in the large-N limit ($E_F \gg \Delta$), the relative contribution of the topological surface mode is therefore rather small. A full quantitative understanding required to describe the energy dependence of the transmissions for all surface modes, considering both disorder and interfaces with metallic contacts (see Section 3.4 for details). In particular, the scattering of surface modes by disorder results in the energy broadening Γ of quantized modes (**Figure 5d**). We evidenced that the quasi-ballistic regime is closely related to the condition $\Gamma \ll \Delta$, which is satisfied over an unusual broad parameters range (disorder strength, energy) in 3D topological insulator nanostructures [41].

3.2. Quantum coherence I: Aharonov-Bohm oscillations

The quantum coherent transport of topological surface states in the transverse direction of a 3D TI nanostructure results in conductance oscillations when a *longitudinal magnetic induction* $B_{//}$ is applied (hence a magnetic flux $\phi = B_{//}*S_{el}$, where S_{el} is the effective electrical cross section of metallic surface states). This is due to the flux-periodic evolution of the Aharonov-Bohm quantum interference giving successive conductance maxima (constructive interference) and minima (destructive interference). Because the phase coherence length can be as large as a couple of micrometers (at very low temperatures), two different situations must be considered for coherent transport in the *transverse motion* of surface states:

1. When $L\phi \sim Lp/2$, clear periodic oscillations of the conductance are directly visible in the longitudinal magneto-conductance $G(B_{//})$. In this case (wide nanoribbons), only the fundamental-harmonic Aharonov-Bohm interference modifies the conductance, a behavior which already reveals that the phase averaging due to disorder is not efficient, despite a high point-defect density in most 3DTI materials.

2. When $L\phi \gg Lp$, that is, either at very low temperatures or for short-perimeter nanowires (quantum wires), the periodic AB behavior is usually hidden in complex $G(B_{//})$ traces. This is due to the multiple-harmonic contributions to the transverse quantum interference (related to the multiple winding of coherent trajectories along the perimeter), and to the influence of disorder (phase shifts). The periodic behavior can, however, be revealed by a Fourier transform analysis.

3.2.1. Case of wide nanoribbons (long-perimeter limit, with $L_\varphi \sim Lp/2$)

For wide nanoribbons, periodic Aharonov-Bohm oscillations are directly visible in $G(B_{//})$ traces, with a rather small amplitude typical for the large-N limit in a mesoscopic conductor, where N is the number of populated transverse modes, with $N = E_F/2\Delta$, since $\Delta = hv_F/Lp$ is smaller than E_F. As seen in **Figure 6** for a wide Bi_2Te_3 nanoribbon ($E_F \sim 120$ meV; $Lp = 940$ nm; $\Delta = 2$ meV), the Aharonov-Bohm period, $\delta B_{AB} = 150$ mT, directly relates to the electrical cross section of the nanostructure, with a value being slightly smaller than that given by its physical dimensions (the topological surface states being "burried" below a thin native oxide layer, typically 5 nm thick). The fast-Fourier transform of the $G(B_{//})$ trace thus gives a single peak at the AB frequency.

According to theory, the overall phase shift of this sine evolution due to the AB quantum interference depends on both the degree of disorder and the energy of Dirac quasi-particles [43]. In most cases, the Fermi energy is very large and AB oscillations are phase locked with a conductance maximum in zero magnetic field, as found in many experiments and confirmed by theory. Yet, theory predicts the opposite situation (conductance minimum for a zero magnetic flux) when the chemical potential is near the Dirac point. The overall energy dependence of this phase shift can be quantitatively obtained from models taking explicitly disorder into account, and it allowed us to reveal an oscillatory behavior that is directly related to quantum confinement (see Section 3.4).

For lower temperatures (longer L_φ) or for narrower nanoribbons, roughly when $L_\varphi \sim Lp$, additional Altshuler-Aronov-Spivak (AAS) oscillations develop in addition. These correspond to quantum interference related to the complete winding of coherent paths along the perimeter, with time-reversed coherent loops so that this contribution is never damped by disorder, which is the usual situation found in (diffusive) mesoscopic conductors.

3.2.2. Case of narrow (quantum) nanowires (short-perimeter limit, $Lp < 2 L_{tr} \ll L_\varphi$)

For narrow nanostructures, the conductance modulation due to both AB and AAS interferences results from a complex mixing of high-order harmonics (multiple windings of coherent loops),
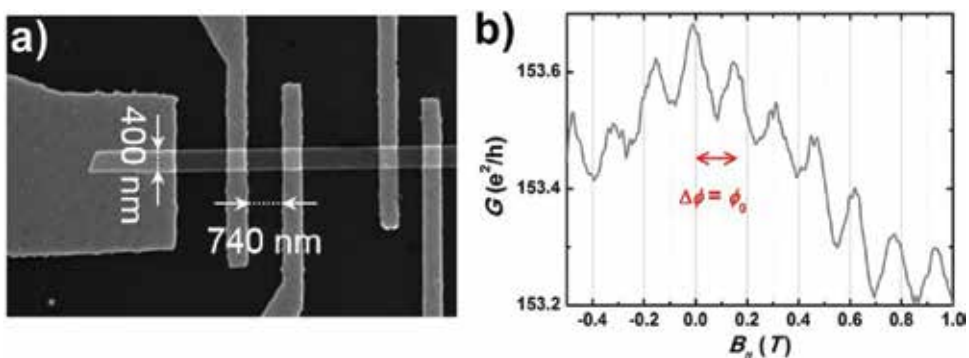

Figure 6. (a) Scanning electron microscope image of a Bi_2Te_3 nanowire with a rather large perimeter $L_p = 940$ nm (width $w = 400$ nm, height $h = 70$ nm) and ohmic CrAu contacts; (b) Aharonov-Bohm periodic oscillations (fundamental harmonics), with a period δB_AB that directly relates to the nanowire's cross section. After [18].

with harmonic-dependent phase shifts induced by disorder and varying relative amplitudes due to quasi-ballistic transport. The periodic-flux dependence of the longitudinal magneto-conductance is therefore hardly visible in most $G(B_{//})$ traces, though it can still be when low-order harmonics remain dominant (as shown in **Figure 7b**). Since this periodic behavior is specific to topological surface states (with a flux-periodic energy spectrum), it can always be unveiled by a careful fast-Fourier transform analysis, provided that enough oscillations are measured (that is, when the field range largely exceeds the fundamental AB period). For a micron-long Bi_2Se_3 quantum wire with perimeter Lp = 280 nm, up to six harmonics were clearly resolved at very low temperature, as seen in **Figure 7c**) [39].

For short wires (L ~ L_φ^{BS}), we also remark that a complication comes further from that aperiodic conductance fluctuations due to bulk carriers coexist with surface periodic AB oscillations [although $L_\varphi^{BS} < L_\varphi^{SS}$, the self-averaging of coherent bulk transport is reduced at very low temperatures due to their charge transport dimensionality d = 3 and to longer L_φ^{BS} values]. Besides, because $G(B_{//})$ curves are measured over a finite field range, the FFT of bulk aperiodic conductance fluctuations often results in a non-monotonous background, possibly giving "peaks" but with no relation to a periodic behavior, contrary to that of $G(B_{//})$ changes due to the AB interference.

The ballistic nature of the transverse motion in such quantum wires results in an unusual temperature dependence of the phase coherence length L_φ^{SS}, with a 1/T behavior observed for all harmonics. This is the signature of both ballistic transport ($L_\varphi = v_F \tau_\varphi$) and a decoherence time $\tau_\varphi \sim 1/T$ limited by a weak coupling to fluctuations of the environment [39]. All other scenarios based on decoherence limited by either the Nyquist noise or the thermal noise give a very different power-law dependence.

An extra signature of the quasi-ballistic regime is also found when considering the relative amplitude of AB harmonics. Contrary to the case of a diffusive mesoscopic conductors, their amplitudes are not increasingly small for higher orders n and they cannot be described by an exponential damping behavior related to the ratio L_φ/L_n, where $L_n = n*L_p$ [39]. This is due to disorder and to both geometric and contact effects, which all influence details of the quantum interference for different quantum coherent paths, in the quasi-ballistic regime [41]. In general, it thus remains difficult to investigate details of the AB oscillations in this regime, due to the complex mixing of all harmonics in the presence of disorder, which varies for different configurations of the microscopic disorder (as obtained by thermal cycling at room temperature of a given mesoscopic conductor).
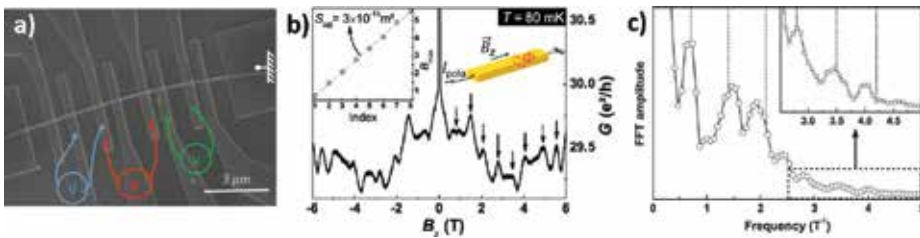

Figure 7. (a) Scanning electron microscope image of a narrow Bi_2Se_3 nanowire with a rather short perimeter Lp = 280 nm and ohmic Al contacts; (b) Aharonov-Bohm periodic oscillations, with the first two harmonics directly visible in the $G(B_{//})$ trace; (c) fast-Fourier transform revealing higher-order harmonics, up to n = 6 at very low temperature. After [39].

3.3. Quantum coherence II: non-universal conductance fluctuations

More information about the weak scattering of quantized surface modes by a non-magnetic disorder can be obtained by studying the (static) conductance fluctuations due to the *longitudinal motion* of surface carriers in a highly-disordered 3DTI quantum wire. Contrary to the case of a diffusive mesoscopic conductor, their statistical properties such as the conductance variance are not universal and they can vary when the quantized Dirac band structure is modified by an Aharonov-Bohm flux [18]. Using a 3D vector magnet, we could vary independently the longitudinal field (tuning of the energy spectrum; transverse motion) and the transverse magnetic field (probing the aperiodic conductance fluctuations due to disorder; longitudinal motion). This provides the complete mapping of quantum interference, as seen in **Figure 8a**). It was shown that the absolute amplitude of the conductance variance varG = δG_{rms}^2 = $<G-<G>>^2$ has a periodic modulation with the magnetic flux (**Figure 8b**), a property specific to surface transport (well-defined cross section). This behavior is well captured by numerical calculations (**Figure 8c** and **d**), which also reproduce the correct amplitude of this modulation mod(varG). We evidenced that non-universal conductance fluctuations are the signature of the weak coupling between transverse quantized modes induced by disorder, and we inferred the amplitude of the disorder broadening Γ from the temperature dependence of the modulation mod(VarG), in rather good agreement
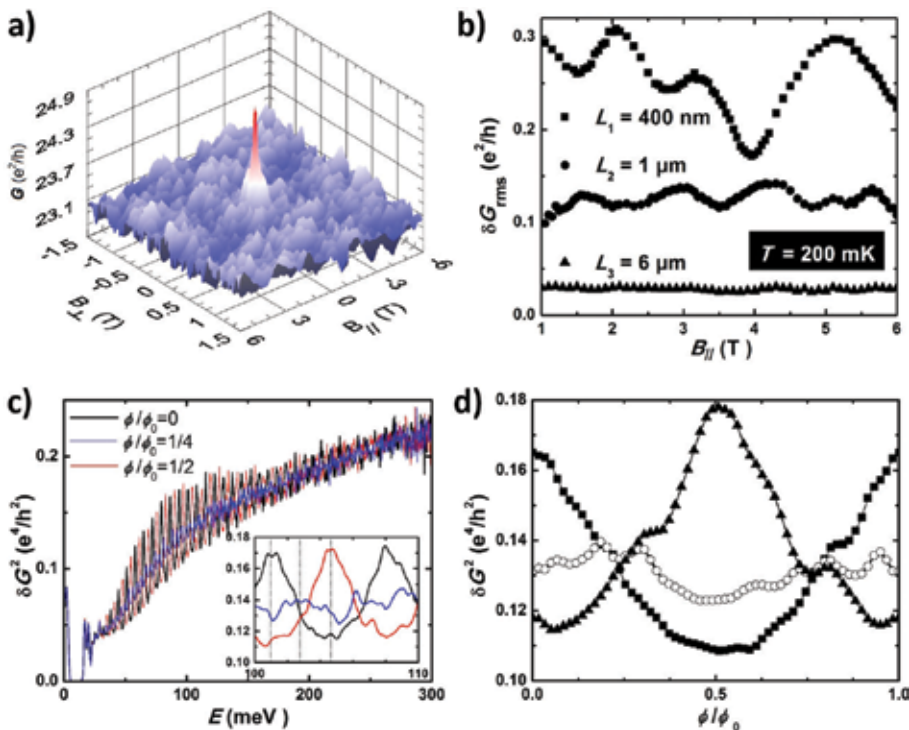

Figure 8. (a) Quantum corrections to the conductance of a Bi_2Se_3 quantum wire mapped over a large range of longitudinal magnetic fields (magnetic flux) and transverse magnetic fields, at very low temperature; (b) flux-dependence of the conductance variance revealing a non-universal behavior and a periodic evolution, a signature of the quasi-ballistic transport of Dirac surface modes; (c and d) numerical calculations of the energy (c) and flux (d) dependences of the conductance variance in a disordered 3DTI quantum wire, showing periodic evolutions due to quantum confinement of all transverse modes. After [18].

with numerical calculations [18]. Because $\Gamma \ll \Delta$, quasi-ballistic transport is a common property to all populated surface modes, each of them giving a significant contribution to the conductance (close to G_0) as compared to that of the perfect transmission case (G_0). Besides, the sharp evolution of varG with the energy of successive transverse modes (**Figure 8c**) suggested that only a limited number of partially-opened modes (nearby E_F) contribute to the conductance fluctuations, due to a rapid energy dependence of the transmission for all channels.

3.4. Quasi-ballistic transport: disorder and transmissions

To evidence that this interpretation is actually very general to all quantum corrections to the conductance in 3DTI quantum wires, it is important to calculate the energy dependence of the transmissions for all modes, taking disorder into account but also interfaces with metallic contacts. This was done in a comparative study of numerical calculations with an analytical model that captures the main property common to all quasi-1D spin-helical surface modes, that is, the suppression of scattering due to quantum confinement [41]. The set of transmissions T_i represents the mesoscopic code of a coherent conductor, from which all important quantities can be calculated [45], the simplest one being the total conductance $G = \sum T_i G_0$. Importantly, the transmissions were found to nearly reach unity for all modes when their longitudinal kinetic energy exceeds Δ (**Figure 9**). The same (rapid) evolution was found even for high-energy modes, though over a slightly broader energy window, thus explaining why quasi-ballistic transport properties exist for many modes over a broad energy range. This also shows that diffusive longitudinal transport is realized only for conductor lengths that largely exceed the transport length. Contrary to the case of 2D quasi-particles with isotropic scattering for which the transition from the ballistic to the diffusive regime is rather abrupt ($l_e < L < L_{tr}$, with $L_{tr} \le 2\, l_e$), the quasi-ballistic regime in 3DTI quantum wires exists over a wider parameter range ($L_{tr}/2 < L < \alpha\, L_{tr}$, with $L_{tr} \gg l_e$ and α is related to the aspect ratio L/L_p). This unusual behavior, related to the enhanced transport length, is due to both the spin texture of Dirac modes (anisotropic scattering) and to their large confinement energy in quantum wires, both favoring the weak scattering of quantized modes by disorder.

3.4.1. Scattering by disorder and contacts

Considering the scattering by disorder as due to a random potential of energy barriers (Gaussian disorder, with a correlation length ξ, see **Figure 10a**), it is possible to give an analytical description of the transmissions of high-energy modes propagating between two transparent ohmic contacts, for different degrees of disorder from the clean limit (ballistic, Fabry-Pérot) to the dirty limit (diffusive) [41]. In the quasi-ballistic regime, we found that the conductance is determined by the interfaces with metallic contacts (similarly to a clean conductor) and not by details of the microscopic disorder in the quantum wire. Due to the quantum confinement of Dirac fermions with evenly-spaced energy levels, the energy dependence of the conductance can oscillate at low energies (whereas its has a linear dependence at high energy, as for the 2D limit) and the average transmission per mode only depends on the nature of the contacts. For an intermediate disorder strength g, Fabry-Pérot interferences are suppressed by efficient phase averaging, and inter-mode scattering results in an oscillatory energy dependence of the transmission, due to the increased density of states at the onset of a

nearby mode and because disorder broadening remains smaller than the energy level spacing. This can be directly seen in the energy dependence of the transmission of a high-energy mode in a Bi_2Se_3 quantum wire (using a realistic value of ξ), as shown in **Figure 10b**). For very large values of g, Γ exceeds Δ and charge transport becomes diffusive.
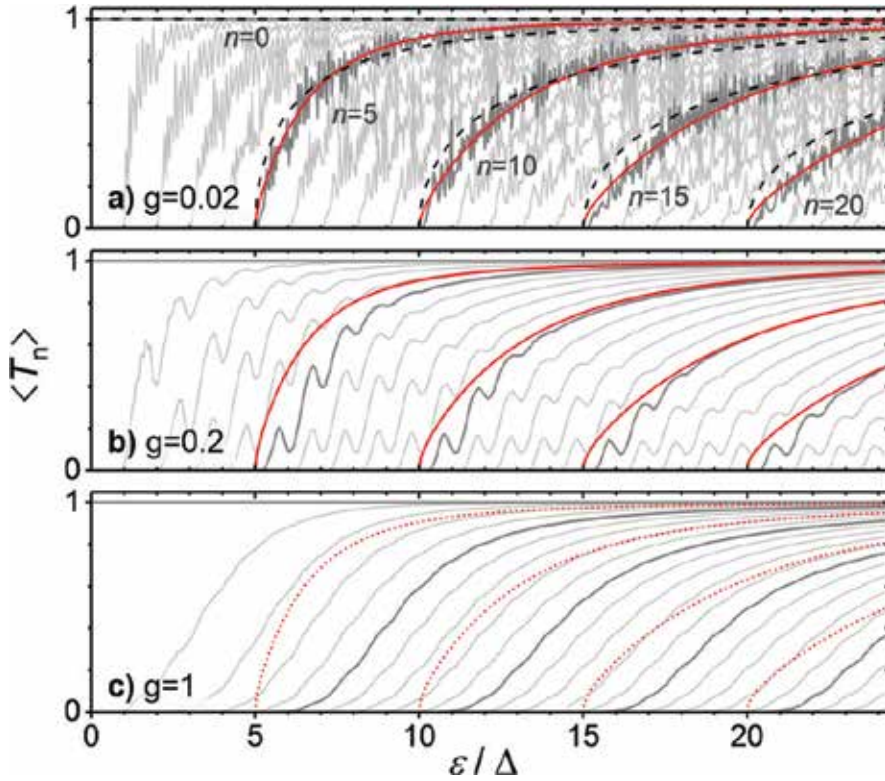

Figure 9. Energy dependence of the surface-mode transmissions in disordered 3D topological insulator quantum wires, for three values of the disorder strength g=0.02 (a), g=0.2 (b), and g=1 (c). After [41].

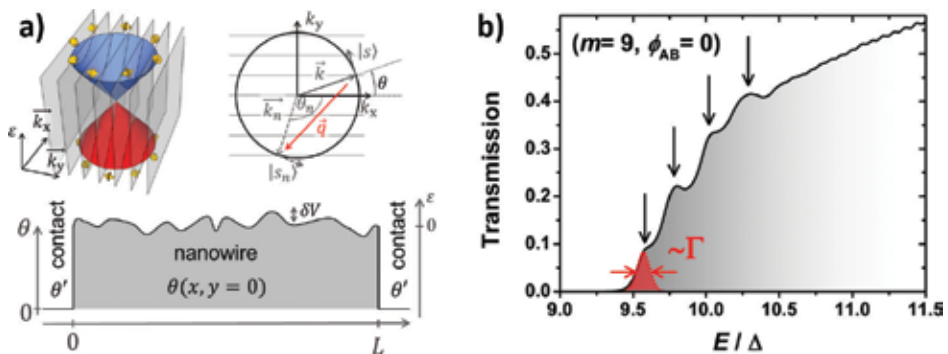**Figure 10.** (a) Quantized band structure of surface modes for a magnetic flux $\varphi = 1/2\varphi_0$ and inter-mode scattering induced by a random disorder potential δV; (b) energy dependence of the transmission of the m = 9 quantized mode for $\phi = 0$, showing resonances due to disorder-induced inter-mode mixing, with an energy broadening Γ. After [41].

To understand why the quasi-ballistic regime exists over a broad range of parameters, it is important to consider the energy dependence of the transport length [see [41] for details], as shown in **Figure 11** for different g values. Contrary to the case of massive quasi-particles, L_{tr} does not vanish at low energy for Dirac fermions in 1D. Instead, it diverges and a similar behavior occurs at high energy, due to the anisotropy of scattering. As a consequence, the transport length has a minimum value that depends on the strength of disorder. For a given disorder correlation length ξ, this minimum value is obtained for $k\xi \approx 1$ and the values of L_{tr}^{min} can be much larger than the transverse dimensions of the nanostructure for all energies, for a broad range of g values, so that the condition for quasi-ballistic transport is always fulfilled for such highly-disordered 3D topological insulator quantum wires. Good agreement was found between this simplified analytical model and numerical calculations, for that details of the microscopic disorder do not affect the conductance in this regime, which is mostly determined by metallic contacts.

3.4.2. Quantitative derivation of the Aharonov-Bohm amplitude

Based on the transmissions calculated for different values of the magnetic flux (corresponding to different quantized energy spectra), it is possible to calculate the energy dependence of Aharonov-Bohm oscillations. As seen in **Figure 11**, their amplitude decreases with the energy of surface modes and a good quantitative agreement with experiments are found at high energies. The oscillatory behavior reported in experiments is also well reproduced, as well as energy-periodic phase shifts [33] which are actually due to the quantized band structure (**Figure 12**) [41].
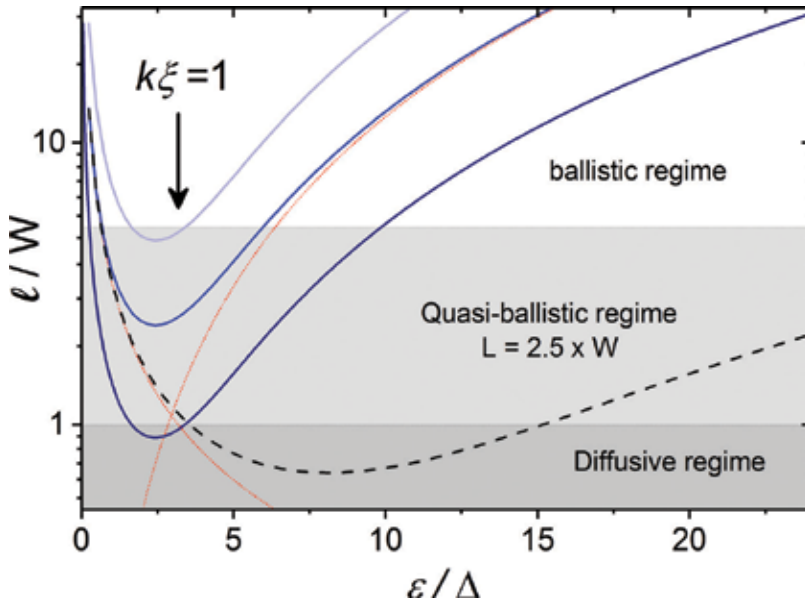

Figure 11. Energy dependence of the transport length l in a quantum wire with a perimeter W = L_p and a transverse energy quantization Δ is calculated for three different strengths of the disorder potential. Red dotted lines show asymptotic behaviors related to the divergence of l = L_{tr} at low or high energies, due to the density of states or to the anisotropy of scattering, respectively. In all cases, the transport of all surface modes is ballistic or quasi-ballistic. After [41].
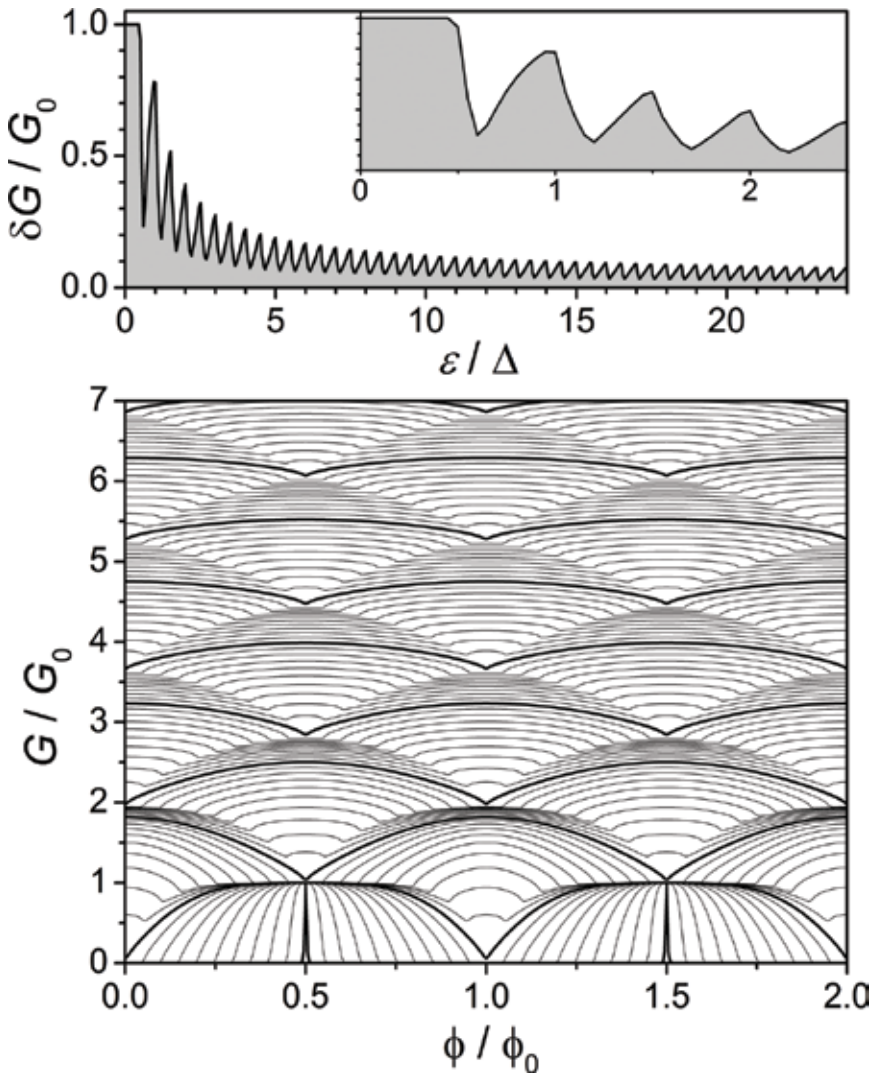
Figure 12. (a) Energy dependence of the Aharonov-Bohm amplitude, rapidly decreasing from the conductance quantum G_0 (contribution of the topological mode only) to a fraction of G_0 (contribution of higher-energy transverse modes); (b) flux dependence of the conductance for different energies, from 0 to 4.5 Δ (successive thin lines correspond to an energy change 0.05 Δ and thick lines to multiple values of 1/2 Δ). Phase shifts are due to the quantized energy spectrum of surface modes. The influence of the topological mode is seen only for very low energies. After [41].

3.4.3. Perfectly-transmitted topological mode

To evidence the influence of the topological mode on the conductance, it is therefore necessary to set the mesoscopic conductor in specific conditions:

1. In long wires, the transmission of all modes but the topological one should be reduced. However, the spin texture of surface Dirac states prevents the strong localization of

high-energy modes, so that this is not a good strategy for highly-doped quantum wires (as this is the case for Bi_2Se_3 nanostructures).

2. In the small-N limit (less than about 4–5 modes populated), the relative influence of the topological mode on the quantum magneto-conductance will be larger, also in short wires. This condition is rather restrictive and requires either to bring the electro-chemical potential close to the Dirac point or to achieve very large values of Δ.

With the goal to investigate the physics of 3D TI quantum wires close to the Dirac point, best results could be obtained in long and ultra-narrow nanostructures [46, 47], since low-energy modes other than the topological mode have a reduced transmission due to disorder (minimum of the backscattering length, so that $L_{tr} \ll L$ and $G \ll G_0$). Furthermore, since the transport of surface modes is quasi-ballistic, it will become important to optimize/control the coupling between metallic contacts and the transverse wave function of a given mode. In particular, the amplitude of probability can have an azimuthal angle dependence, which varies from one mode to another, so that quantum transport properties will ultimately depend on the exact geometry of the mesoscopic conductor. Also, the low-energy spectrum can be modified by a large transverse magnetic field. For a rectangular cross section (**Figure 13**), a striking property is related to the evolution of the topological mode from a helical state to a chiral edge state, when a moderate transverse magnetic field is applied [42]. The specific orbital response of such 3DTI quantum wires correponds to an intermediate situation between the quantum spin Hall in a 2D TI and the Quantum Hall effect in 2DEGs.

The control of low-energy quantum states in 3DTI nanostructures would offer novel opportunities for their quantum manipulation as well as for spin filtering, tuning the quantum states with an electric or a magnetic field. When coupled to metallic electrodes with gapped excitations, the topological mode generates novel quantum states with an intrinsic topological protection, such as Majorana bound states or spin-polarized edge states in the quantum

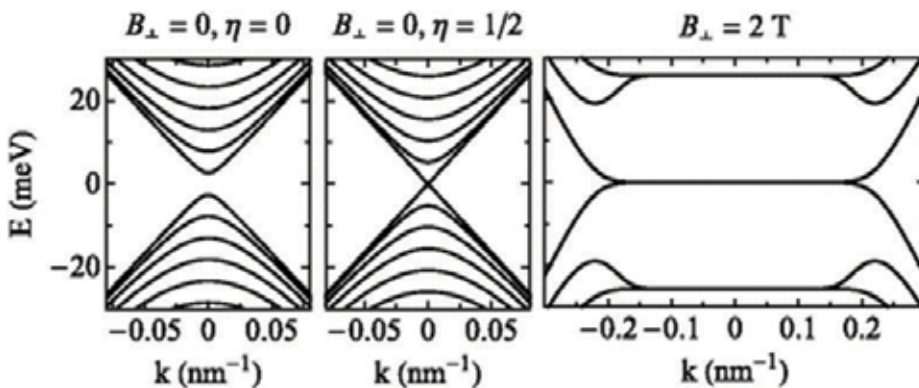**Figure 13.** Energy spectrum of a 3DTI quantum wire with a rectangular cross section (h = 40 nm; w = 160 nm) for η = ϕ/ϕ_0 = 0 (left) and η = ϕ/ϕ_0 = ½ (center; right), low-energy band structure in the presence of a large transverse magnetic induction $B_\perp$ = 2 T, showing the emergence of chiral edge states without dispersion over a wide range of impulse, independent of η. After [42].

anomalous Hall regime. These could be important for quantum dynamics studies, with limited decoherence. Non-topological low-energy modes are also interesting for their energy tuning, by a gate voltage or a magnetic flux, which is associated with a continuous change of their spin state between nearly-orthogonal states. Besides, these can be either 1D extended states (long quantum wires) or 0D localized states (short quantum wires, that is, for $L < L_{tr}$).

4. Conclusion and perspectives

The weak coupling of surface states in 3D topological insulator quantum wires, due to both their spin texture and the quantum confinement of Dirac fermions, gives unique opportunities to control novel quantum states in mesoscopic conductors, despite non-magnetic disorder. Yet, it remains difficult to control a small number of transverse quantized states close to the Dirac degeneracy point, mostly due to intrinsic limitations in conventional 3DTIs materials. Whereas the Bi_2Se_3 family offers many advantages (tunable band structure in solid solutions of ternary compounds and high-quality single-crystalline nanostructures), it remains difficult to achieve surface transport only, and, most important, to control low-energy surface quasi-particles (large residual bulk doping or interface charge transfer, due to disorder).

Therefore, the next generation of electronic devices based on 3D topological insulators will necessarily be developed from advanced functional nanostructures and heterostructures. One of the most important challenge will be the full control of interface band bending, with a high-enough interface quality so as to optimize the coupling between metallic contacts and spin-helical surface Dirac fermions. For instance, this is particularly true for spin transport experiments, which require to minimize the momentum/spin relaxation below the contacts in order to make use of the intrinsic potential of electronic states with spin-momentum locking.

Toward this goal, new growth and nanofabrication methods need to be envisioned, in combination with those already used to prepare high-quality single-crystalline nanostructures (vapor transport, vapor-liquid-solid epitaxy, and chemical-vapor deposition). Novel techniques, such as the in-situ stencil lithography of metallic contacts combined the growth of ultra-thin films by molecular beam epitaxy, already gave some promising results, for instance to realize highly-transparent superconducting contacts and investigate topological superconductivity [48]. Also, atomic layer epitaxy holds promises to realize core-shell lateral nanostructures adapted to the control of the electro-chemical potential at the interface with a topological insulator [49–51].

Acknowledgements

Conflict of interest

The authors declare no conflict of interest.

Author details

Romain Giraud[1,2]* and Joseph Dufouleur[2]

*Address all correspondence to: romain.giraud@cea.fr

1 Univ. Grenoble Alpes, CNRS, CEA, Grenoble-INP, Institute of Engineering Univ. Grenoble Alpes, INAC-Spintec, Grenoble, France

2 Leibniz Institute for Solid State and Materials Research, IFW Dresden, Dresden, Germany

References

[1] Hasan MZ, Kane CL. Topological insulators. Reviews of Modern Physics. 2010;**82**:3045

[2] Qi X-L, Zhang S-C. Topological insulators and superconductors. Reviews of Modern Physics. 2011;**83**:1057

[3] Bernevig BA, Zhang S-C. Quantum spin Hall effect. Physical Review Letters. 2006;**96**: 106802

[4] Kane CL, Mele EJ. Quantum spin Hall effect in Graphene. Physical Review Letters. 2005;**95**:226801. DOI: https://doi.org/10.1103/PhysRevLett.95.226801

[5] Büttiker M. Edge-state physics without magnetic fields. Science. 2009;**325**:278. DOI: 10.1126/science.1177157

[6] Fu L, Kane CL, Mele EJ. Topological insulators in three dimensions. Physical Review Letters. 2007;**98**:106803

[7] Moore JE, Balents L. Topological invariants of time-reversal-invariant band structures. Physical Review B. 2007;**75**:121306. DOI: https://doi.org/10.1103/PhysRevB.75.121306

[8] Culcer D, Hwang EH, Stanescu TD, Das Sarma S. Two-dimensional surface charge transport in topological insulators. Physical Review B. 2010;**82**:155457

[9] Kane CL, Mele EJ. Z2 topological order and the quantum spin Hall effect. Physical Review Letters. 2005;**95**:146802

[10] Fu L, Kane CL. Superconducting proximity effect and Majorana fermions at the surface of a topological insulator. Physical Review Letters. 2008;**100**:096407

[11] Oh S. The complete quantum Hall trio. Science. 2013;**340**:153

[12] König M, Wiedmann S, Brüne C, Roth A, Buhmann H, Molenkamp LW, Qi X-L, Zhang S-C. Quantum spin Hall insulator state in HgTe quantum wells. Science. 2007;**318**:766-770. DOI: 10.1126/science.1148047

[13] Bernevig BA, Zhang S-C. Quantum spin Hall effect. Physical Review Letters. 2006;**96**:106802

[14] Chen YL, Analytis JG, Chu J-H, Liu ZK, Mo S-K, Qi XL, Zhang HJ, Lu DH, Dai X, Fang Z, Zhang SC, Fisher IR, Hussain Z, Shen Z-X. Science. 2009;**325**:178

[15] Hsieh D, Xia Y, Qian D, Wray L, Dil JH, Meier F, Osterwalder J, Patthey L, Checkelsky JG, Ong NP, Fedorov AV, Lin H, Bansil A, Grauer D, Hor YS, Cava RJ, Hasan MZ. Nature (London). 2009;**460**:1101

[16] Xia Y, Qian D, Hsieh D, Wray L, Pal A, Lin H, Bansil A, Grauer D, Hor YS, Cava RJ, Hasan MZ. Nature Physics. 2009;**5**:398

[17] Dufouleur J, Veyrat L, Dassonneville B, Nowka C, Hampel S, Leksin P, Eichler B, Schmidt OG, Büchner B, Giraud R. Enhanced mobility of spin-helical Dirac fermions in disordered 3D topological insulators. Nano Letters. 2016;**16**:6733

[18] Dufouleur J, Veyrat L, Dassonneville B, Xypakis E, Bardarson JH, Nowka C, Hampel S, Eichler B, Schmidt OG, Büchner B, Giraud R. Weakly-coupled quasi-1D helical modes in disordered 3D topological insulator quantum wires. Scientific Reports. 2017;**7**:45276

[19] Dankert A, Geurs J, Kamalakar MV, Charpentier S, Dash SP. Room temperature electrical detection of spin polarized currents in topological insulators. Nano Letters. 2015;**15**:7976

[20] Jamali M, Lee JS, Jeong JS, Mahfouzi F, Lv Y, Zhao Z, Nikolić BK, Mkhoyan KA, Samarth N, Wang J-P. Giant spin pumping and inverse spin Hall effect in the presence of surface and bulk spin-orbit coupling of topological insulator Bi_2Se_3. Nano Letters. 2015;**15**:7126

[21] Lee JS, Richardella A, Hickey DR, Mkhoyan KA, Samarth N. Mapping the chemical potential dependence of current-induced spin polarization in a topological insulator. Physical Review B. 2015;**92**:155312

[22] Li CH, vant Erve OM, Robinson JT, Liu Y, Li L, Jonker BT. Electrical detection of charge-current-induced spin polarization due to spin-momentum locking in Bi_2Se_3. Nature Nanotechnology. 2014;**9**:218

[23] Mellnik AR, Lee JS, Richardella A, Grab JL, Mintun PJ, Fischer MH, Vaezi A, Manchon A, Kim E-A, Samarth N, Ralph DC. Spin-transfer torque generated by a topological insulator. Nature. 2014;**511**:449

[24] Pesin D, MacDonald AH. Spintronics and pseudospintronics in graphene and topological insulators. Nature Materials. 2012;**11**:409

[25] Rojas-Sánchez JC, Oyarzun S, Fu Y, Marty A, Vergnaud C, Gambarelli S, Vila L, Jamet M, Ohtsubo Y, Taleb-Ibrahimi A, Le Fevre P, Bertran F, Reyren N, George J-M, Fert A. Spin to charge conversion at room temperature by spin pumping into a new type of topological insulator: α-Sn films. Physical Review Letters. 2016;**116**:096602

[26] Müchler L, Casper F, Yan B, Chadov S, Felser C. Topological insulators and thermoelectric materials. Physica Status Solidi RRL. 2013;**7**:91-100. DOI: https://doi.org/10.1002/pssr.201206411

[27] Cava RJ, Ji H, Fuccillo MK, Gibson QD, Hor YS. Crystal structure and chemistry of topological insulators. Journal of Materials Chemistry C. 2013;**1**:3176

[28] Brahlek M, Koirala N, Bansal N, Oh S. Transport properties of topological insulators: Band bending, bulk metal-to-insulator transition, and weak anti-localization. Solid State Communications. 2015;**215-216**:54-62. DOI: 10.1016/j.ssc.2014.10.021

[29] Zhang J et al. Band structure engineering in (Bi1−xSbx)2Te3 ternary topological insulators. Nature Communications. 2011;**2**:574

[30] Xu Y, Miotkowski I, Liu C, Tian J, Nam H, Alidoust N, Hu J, Shih C-K, Hasan MZ, Chen YP. Observation of topological surface state quantum Hall effect in an intrinsic three-dimensional topological insulator. Nature Physics. 2014;**10**:956-963. DOI: 10.1038/nphys3140

[31] Bässler S, Hamdou B, Sergelius P, Michel A-K, Zierold R, Reith H, Gooth J, Nielsch K. One-dimensional edge transport on the surface of cylindrical $Bi_xTe_{3-y}Se_y$ nanowires in transverse magnetic fields. Applied Physics Letters. 2015;**107**(18):181602

[32] Hong SS, Zhang Y, Cha JJ, Qi X-L, Cui Y. One-dimensional helical transport in topological insulator nanowire interferometers. Nano Letters. 2014;**14**:2815

[33] Jauregui LA, Pettes MT, Rokhinson LP, Shi L, Chen YP. Magnetic field-induced helical mode and topological transitions in a topological insulator nanoribbon. Nature Nanotechnology. 2016;**11**:345

[34] Renard VT et al. Quantum corrections to the conductivity and Hall coefficient of a two-dimensional electron gas in a dirty AlGaAs/GaAs/AlGaAs quantum well: From the diffusive to the ballistic regime. Physical Review B. 2005;**72**:075313

[35] Niimi Y et al. Quantum coherence at low temperatures in mesoscopic systems: Effect of disorder. Physical Review B. 2010;**81**:245306

[36] Veyrat L, Iacovella F, Dufouleur J, Nowka C, Funke H, Yang M, Escoffier W, Goiran M, Eichler B, Schmidt OG, Büchner B, Hampel S, Giraud R. Band bending inversion in Bi_2Se_3 nanostructures. Nano Letters. 2015;**15**:7503

[37] Nowka C, Veyrat L, Gorantla S, Steiner U, Eichler B, Schmidt OG, Funke H, Dufouleur J, Büchner B, Giraud R, Hampel S. Catalyst-free growth of single-cristalline Bi_2Se_3 nanostructures for quantum transport studies. Crystal Growth & Design. 2015;**15**:4272

[38] Xu Y, Miotkowski I, Chen YP. Quantum transport of two-species Dirac fermions in dual-gated three-dimensional topological insulators. Nature Communications. 2016;**7**:11434

[39] Dufouleur J, Veyrat L, Teichgräber A, Neuhaus S, Nowka C, Hampel S, Cayssol J, Schumann J, Eichler B, Schmidt OG, Büchner B, Giraud R. Quasiballistic transport of Dirac fermions in a Bi_2Se_3 nanowire. Physical Review Letters. 2013;**110**:186806

[40] Peng H, Lai K, Kong D, Meister S, Chen Y, Qi X-L, Zhang S-C, Shen und Z-X, Cui Y. Aharonov-Bohm interference in topological insulator nanoribbons. Nature Materials. 2010;**9**(3):225-229

[41] Dufouleur J, Xypakis E, Büchner B, Giraud R, Bardarson JH. Suppression of scattering in quantum confined 2D-helical Dirac systems. Physical Review B. 2018;**97**:075401

[42] De Juan F, Ilan R, Bardarson JH. Robust transport signatures of topological superconductivity in topological insulator nanowires. Physical Review Letters. 2014;**113**:107003

[43] Bardarson JH, Brouwer PW, Moore JE. Aharonov-Bohm oscillations in disordered topological insulator nanowires. Physical Review Letters. 2010;**105**:156803

[44] Cho S, Dellabetta B, Zhong R, Schneeloch J, Liu T, Gu G, Gilbert MJ, Mason N. Aharonov–Bohm oscillations in a quasi-ballistic three-dimensional topological insulator nanowire. Nature Communications. 2015;**6**:7634

[45] Akkermans E, Montambaux G. Mesoscopic Physics of Electrons and Photons. 1st ed. Cambridge, England: Cambridge University Press; 2007

[46] Krieg J, Chen C, Avila J, Zhang Z, Sigle W, Zhang H, Trautmann C, Asensio und MC, Toimil-Molares ME. Exploring the electronic structure and chemical homogeneity of individual Bi_2Te_3 nanowires by nano-angle-resolved photoemission spectroscopy. Nano Letters. 2016;**16**(7):4001-4007

[47] Krieg J, Funke H, Giraud R, Dufouleur J, Trautmann C, Büchner B, Toimil-Morales E. Magnetotransport measurements on Bi_2Te_3 nanowires electrodeposited in etched ion-track membranes. Journal of Physics and Chemistry of Solids. (Accepted)

[48] Schüffelgen P et al. Stencil lithography of superconducting contacts on MBE-grown topological insulator thin films. Journal of Crystal Growth. 2017;**477**:183-187

[49] Hamdou B, Gooth J, Böhnert T, Dorn A, Akinsinde L, Pippel E, Zierold R, Nielsch K. Thermoelectric properties of band structure engineered topological insulator ($Bi_{1-x}Sb_x)_2Te_3$ nanowires. Advanced Energy Materials. 2015;**5**:1500280

[50] Murakami S, Nagaosa N, Zhang S-C. Spin-Hall insulator. Physical Review Letters. 2004;**93**:156804

[51] Pankratov OA, Pakhomov SV, Volkov BA. Supersymmetry in heterojunctions: Band-inverting contact on the basis of $Pb_{1-x}Sn_xTe$ and $Hg_{1-x}Cd_xTe$. Solid State Communications. 1987;**61**:93-96. DOI: 10.1016/0038-1098(87)90934-3

Observation of the Weak Antilocalization and Linear Magnetoresistance in Topological Insulator Thin Film Hall Bar Device

Sunil Kumar Pradhan and Ranjan Barik

Additional information is available at the end of the chapter

Abstract

In this research work, without using any resist and lithography techniques, we report clean, surface protected and high quality Topological Insulator (TI) thin film Hall Bar device of millimeter size long. In the magnetotransport measurements, the pronounced effect of weak antilocalization (WAL) behavior has been observed at low temperatures over the range T = 4–10 K and in the low field regions and the WAL cusp disappears as we go from 10 K onwards to higher temperatures, also we find that the high-field magnetoresistance (MR) is linear in field. With respect to magnetic field (B), the MR behavior seems to be symmetric. We also analyze the thickness dependent weak antilocalization (WAL) behavior, which has been observed in Topological Insulator Bi_2Te_3 thin film Hall Bar device. For varying thickness, our systematic magnetotransport measurements reveal WAL signals obtain in thicker films whereas below the critical thickness of ~4 nm, a sudden diminishment of the surface transport has been observed by suppression of WAL behavior. The analyzed and pronounced behavior of this effect is also greatly dependent on the temperatures, where the WAL cusps are observed in the low-field regions and at low temperatures.

Keywords: topological insulator, Bi_2Te_3, weak antilocalization, linear magnetoresistance

1. Introduction

In the recent years because of unique feature of topologically protected surface states which have strong spin-orbit coupling the three-dimensional (3D) topological insulators (TIs) like Bi_2Se_3, Bi_2Te_3 and their counterpart alloys have attracted tremendous and intense research

attention [1–4]. The surface states which has been observed, are believed to be protected against time-reversal-symmetry, owing to the fact that, electrons in the surface state behave as dirac electrons as in case of 3D TI [5], which can be applied to spintronics devices [6], quantum computing [7] and it is necessary to investigate TI from the transport point of view in order to address the electronic properties of Dirac electrons. In terms of weak antilocalization (WAL) effect in thin films [8, 9], nanoribbons [10] and 3D TI crystals [11, 12], several research groups have already analyzed this transport behavior, by making small scale devices using conventional lithography techniques, but no paper has yet reported to observe this magneto-transport behavior in Bi_2Te_3 thin film Hall Bar device without using lithography techniques. Also in terms of potential applications in magnetic sensors and magnetic random access memory [13], materials exhibiting linear magnetoresistance (LMR) are found to be promising candidates. The linear MR behavior in Bi_2Se_3 [14, 15] and Bi_2Te_3 [16, 17] has been revealed in recent literatures and these TIs provide an ideal platform to study the origin of LMR because of the unique surface states that are naturally zero band gaps with linear dispersion.

It is necessary to grow a high quality TI thin film, in order to observe this magnetotransport behavior in topological insulator Bi_2Te_3. Molecular beam epitaxy (MBE) in this respect has demonstrated and found to be suitable in producing samples with carrier mobilities higher than the bulk crystals with precise control on the growth rate, out of modern thin film growth techniques. In order to realize layer by layer growth and obtaining the right stoichiometry [18] this technology is very important. Here, with respect to weak antilocalization (WAL) and magnetoresistance (MR), we report on the magnetotransport measurement. After fabrication, the thin film Hall Bar device is subjected to Physical Property Measurement System (PPMS), where the magnetic field is applied perpendicular to the plane of Hall Bar device. At programmed temperatures, by sweeping the magnetic field between −9 T and + 9 T, the Longitudinal Resistance is measured.

2. Experimental

Using Molecular Beam Epitaxy (MBE), the thin films of Bi_2Te_3 were grown on 7 × 7 mm dimension Al_2O_3 (0001) substrate. Prior to the deposition, the base pressure was maintained at ~ 8 × 10^{-10} mbar. To evaporate Bi (99%) and Te (99.9%) sources, the standard Knudsen diffusion cells were used and the Te and Bi were heated to 205 and 630°C respectively. At last at Te/Bi flux ratio of ~10 with a growth rate of 8 Å per minute the Bi_2Te_3 Thin films were prepared at a substrate temperature of 230°C. By defining the pattern, using standard lithographic techniques like electron-beam lithography or photolithography, numerous methods in the recent literatures [19–22] were reported in making thin film hall bar geometry but in our work, without using any resists and lithography techniques, we applied a clean method of making a topological insulator thin film hall bar device. In our device fabrication, we employed two physical masks, for the same sample holder. One for using in reactive ion etching (RIE), called etching mask and other for depositing metal electrodes, called metal mask. For defining the dimension of the thin film hall Bar, the etching mask served the purpose and the metal mask served the purpose of depositing the metal electrodes. After the
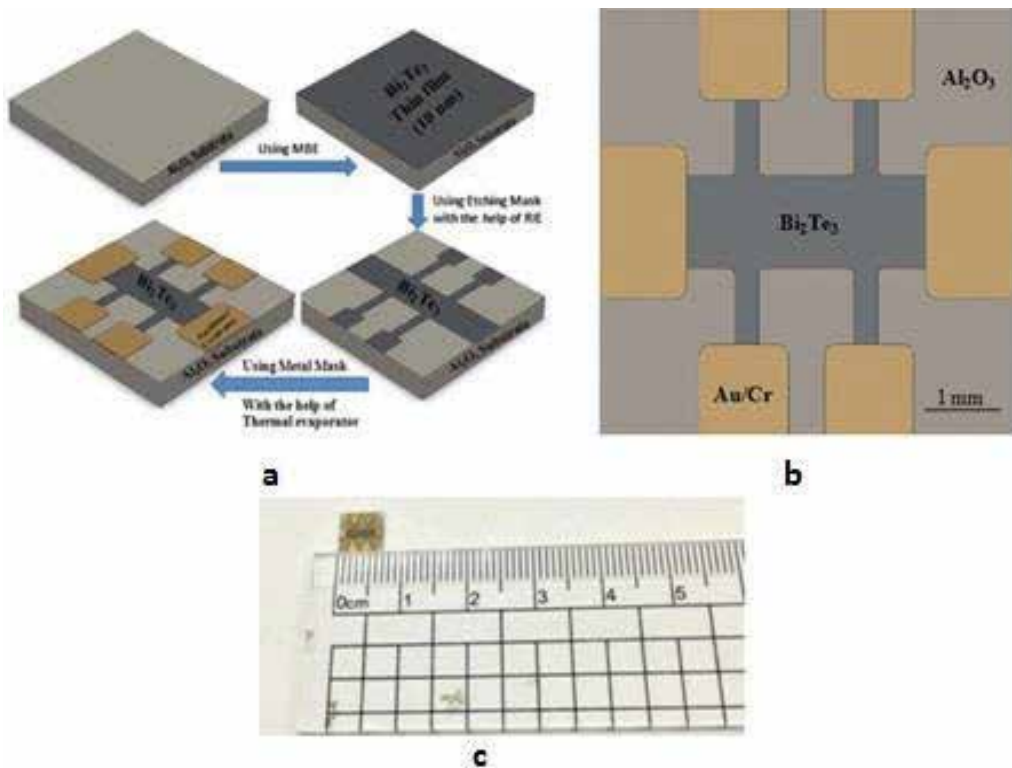
Figure 1. Methodology of fabrication of topological insulator Bi_2Te_3 thin film hall bar device.

thin film sample synthesized from the MBE, with the help of RIE the thin film hall Bar was made, using the etching mask placed over the sample on the sample holder. With the aid of CF_4 gas for 30 s, the etching was done for getting the required Hall Bar structure. Finally, on the same sample holder, Au (40 nm)/Cr (40 nm) metal ohmic contacts were made with the help of thermal evaporation, using the metal mask over the thin film Hall Bar sample. With dimension of 2 mm long and 1.5 mm wide we obtained our fabricated Topological Insulator Bi_2Te_3 thin film Hall Bar device. The **Figure 1a** shows the Schematic diagram of the device fabrication with image of Bi_2Te_3 topological insulator thin film hall bar device and the 7 × 7 mm dimension of the thin film hall bar device in **Figure 1b** and **c**, respectively.

3. Characterizations

Using AFM in a tapping mode, the topography of thin films was evaluated and by scanning a scratch deliberately made on as-grown thin films, the thickness was reliably determined. With the help of Siemens D-500 X-ray Diffractometer (XRD) further structural analyses were also carried out. In **Figure 2b** and **c** representative topographic AFM images of Bi2Te3 thin films are shown respectively, suggesting a layer-by-layer growth mode, revealing the ultra-smooth
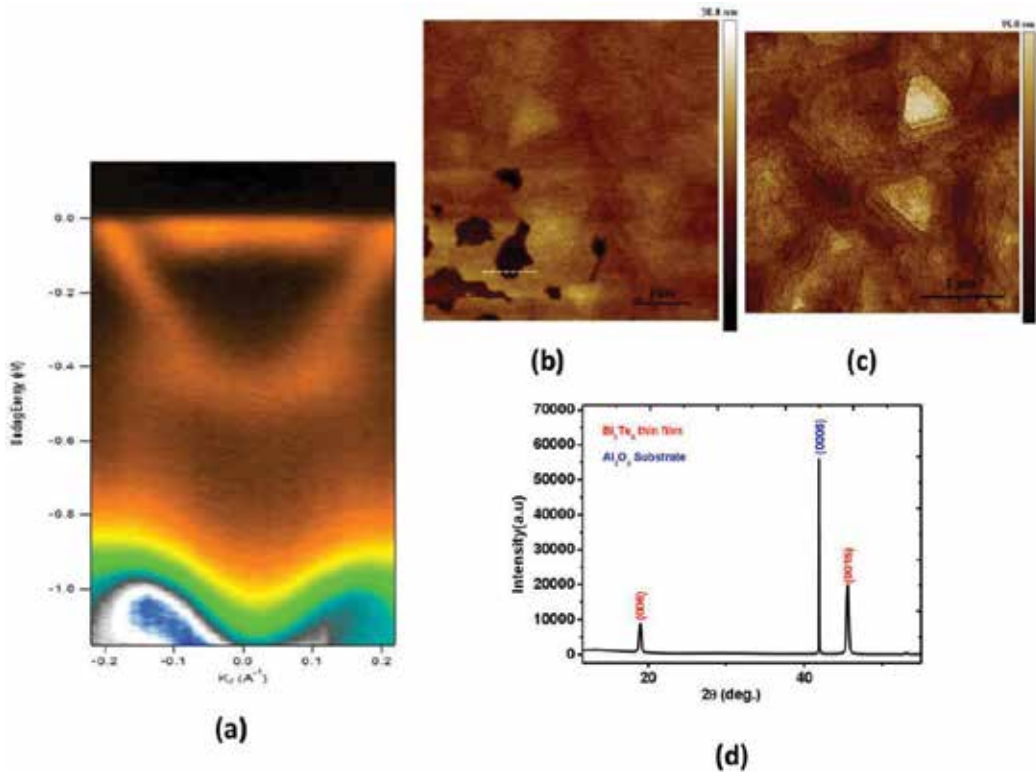
Figure 2. Characterization evidences of topological insulator Bi_2Te_3 thin film.

surfaces with large area terraces. In **Figure 2b**, the dashed line drawn, reveals 10 nm thickness film and **Figure 2c** illustrates 10 nm thin film, by the formation of 4–5 stacked layer comprising of domains of triangular terraces. This suggests a favorable growth dynamics accounting for the high crystalline quality of Topological Insulator thin film on Al_2O_3 substrate with the absence of spirals on the terraces together with the shape of the terrace. The XRD experiments were further conducted to investigate the crystalline quality and orientations. With the diffraction peak from Al_2O_3 substrate, **Figure 2d** displays (003) family diffraction peak from Bi_2Te_3 thin film. The result of the Angle Resolved Photo Emission Spectroscopy (ARPES), implying strong surface states is shown in **Figure 2a**.

4. Results and discussion

4.1. Magnetotransport measurement

In our observation and study, we confirm the weak antilocalization (WAL) effect and the origin of this research phenomenon is investigated. If we consider, interaction between time-reversal pair of electronic waves, then there is a constructive interference of this two phase-coherent

electronic waves propagating in opposite directions along the same closed path, in the absence of spin-orbit interaction, which gives rise to Weak-Localization (WL) effect. This effect gives results in increase of resistance or decrease of conductance. But the constructive interference is broken as a result of a phase difference between the two electronic waves, when the magnetic field is applied perpendicular to the plane of the system. By increasing the magnetic field, the increase of resistance can gradually be removed and consequently negative magnetoresistivity occurs. It finally gives rise to increase of the resistance or reduction in the conductance around zero magnetic field as the resistance correction influenced by this localization. In the presence of the spin-orbit interaction, there is a significant enhancement in the resistance, which is known as weak antilocalization effect [23, 24]. As far as the quality of the grown thin film is concerned, it has significant impact on the studies of transport properties of charge carriers and the weak antilocalization (WAL) behavior is an evaluation and indication for such improvement in the quality of the thin film, which manifests both the Dirac nature of the surface states in the bulk of Topological Insulators [8, 25] and strong spin-orbit interaction. If we Compare the 2D electron system, the 2D surface state of the three-dimensional topological insulator is different [26] as an odd number of Dirac points are considered to be encircled by Fermi arc [27, 28]. If we evaluate the topological insulator, its surface remains metallic and cannot be localized by disorder [29]. By Hikami et al. [30], the surface state of the topological insulator is well described. The **Figure 3a** shows the results of the magnetotransport measurement for the temperature ranges from T = 4 to 100 K and fields up to 9 T. The pronounced effect of WAL cusps are marked at low temperature between 4 and 10 K and in the low field regions as shown in the **Figure 3a**. Also we observe the enhancement of peak and the dip structure behaviors in the magnetoresistance, which is quite remarkable with decreasing temperatures. We have defined the normalized magnetoresistance (MR) as a function of magnetic field as MR = [[R (B) − R (0)]/R (0)] × 100%., where R (B) and R (0) are the resistances at field B and at zero field, respectively. The WAL cusps disappear, as the temperature is increased from 10 K onwards. We observe the WAL characteristic behaviors in the temperature ranges from 4 to 10 K as shown in the **Figure 3a**, and disappearance of WAL cusp from 10 K onwards. The MR curves seems to be quadratic like B dependence at low fields between 2 and 6 T and at higher fields from 6 T onwards, the MR follows linear like behavior and does not saturate. The quadratic growth here can be well explained and analyzed by semi-classical model, where the magnetic field drifts the conduction electrons and these conduction electrons are deflected by the Lorentz force. At T = 4 K, the thickness dependent WAL behavior is shown in the **Figure 3b** showing the WAL cusps for 10, 20, 50 nm thickness film, where as there is no observable WAL effect in ultra-thin films like 4 and 2 nm and the magnetoresistance (MR) curve attains to be flat w.r.t. magnetic field (B). The Fermi level is not in the gap but crosses the Surface State, as the film is thinned enough. Hence, the observed drastic suppression of the surface transport is likely due to an enhanced scattering of the carriers. The phase breaking length (L_φ), which is of temperature dependence is extracted from the Hikami-Larkin-Nagaoka (HLN) model fit [30] for 10 nm thickness film is shown in the **Figure 3c**, which reveals the relatively large phase coherent length of 155.8 nm at 4 K, by fitting to the HLN model. The **Figure 3d** shows the Conductance change with respect to low magnetic field region with the HLN model fit for 10 nm thickness film.
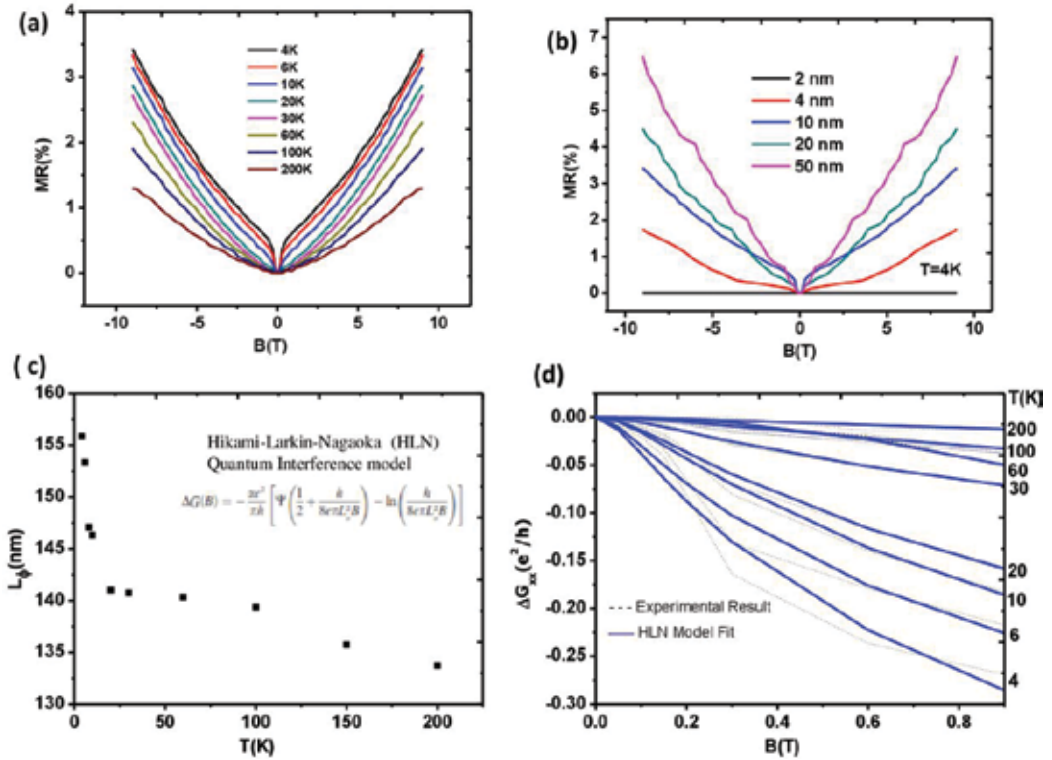
Figure 3. Results of Bi_2Te_3 thin films hall bar device with respect to magnetotransport.

4.2. Linear magnetoresistance (LMR)

We have observed linear magnetoresistance (LMR) behavior as shown in the **Figure 4** in our magnetotransport measurement study and it is found that the observed behavior is found to be seen in higher fields in the ranges from 6 to 9 T. In this linear region, there is a little variation in the slope of dMR/dB with respect to temperatures. We have observed these linear and non-saturating magnetoresistance features in the temperature ranges from 2 to 20 K. Previous literatures show the same trends and results where the high field LMR was found in single crystal of YPdBi Heusler topological insulator [31] and in Bi_2Se_3 nanoribbons [15]. The topological surface states are manifested by these results. The Linear MR at strong magnetic field is expected to occur in the quantum limit in the linear energy spectrum, in which all the electrons populated into single Landau level as per the theory, proposed by Abrikosov [32, 33]. This is governed and satisfied by the inequality relation $(h/2\pi) \times W_c > E_f$, where $(h/2\pi) \times W_c$ is the cyclotron energy and E_f is the Fermi energy. So the weak temperature dependence is predicted by quantum LMR theory. However, recent literature shows that linear magnetoresistance (LMR) appears to occur in smaller magnetic field, where several Landau levels are populated by electrons [34]. There are some other research literatures, where it is analyzed that LMR at the high field as a consequence of closing of band gap under certain pressure. This profound alteration of band structure is
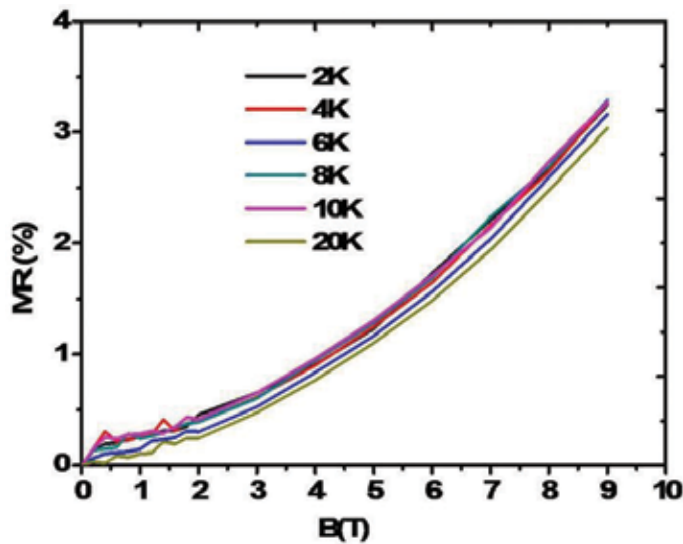
Figure 4. LMR of Bi_2Te_3 thin film hall bar device at high fields.

found in silver rich or silver deficient chalcogenides [35] by the application of hydrostatic pressure. Hence, the gap less linear energy spectrum, which is suggested by this, such as the surface states of topological insulators is required for the observation of Linear MR in high fields. As there exists a bulk band gap for the bulk state, in this analysis, the possible bulk contribution in the quantum LMR is excluded. To the previous literature on topological insulator B_2Te_3 nano-sheets [17], our results in linear MR are quite similar. As shown in the **Figure 4**, in our study we report $\cong 3.2\%$ MR value for temperatures ranging from 2 to 20 K. This characteristic feature of Linear MR (LMR), which has been found to be proportional to the magnetic field (B), is suitable for application in high magnetic field sensors.

4.3. Temperature-dependent electrical resistance measurement

For observing the temperature dependent resistance, we did the electrical measurements in our study. The longitudinal resistance (R) at zero magnetic field as a function of temperature is shown in the **Figure 5**. From the figure it is evident that, there is a decrease in the resistance in the temperature range from 300 to 240 K. The reason, we can consider with the bulk band gap. With the recent report on the ARPES measurements analysis of Bi_2Se_3 thin film grown on SiC (0001) by MBE [36], where there is a progressive and systematic increase in the bulk band gap with reducing film thickness, it implies the quantum confinement of the film along the growth direction perpendicular to the substrate. As in our case, the grown film is thin enough, so the result is quite practical and evident at higher temperatures. The longitudinal resistance decreases as the temperature decreases from 240 to 4 K, resembling the metallic like behavior as observed in most of the topological Insulators [37]. Such trend of decrease with temperatures can be analyzed and explained by power law increase of mobility with temperatures and alleviated phonon scattering. The resistance attains to be constant value
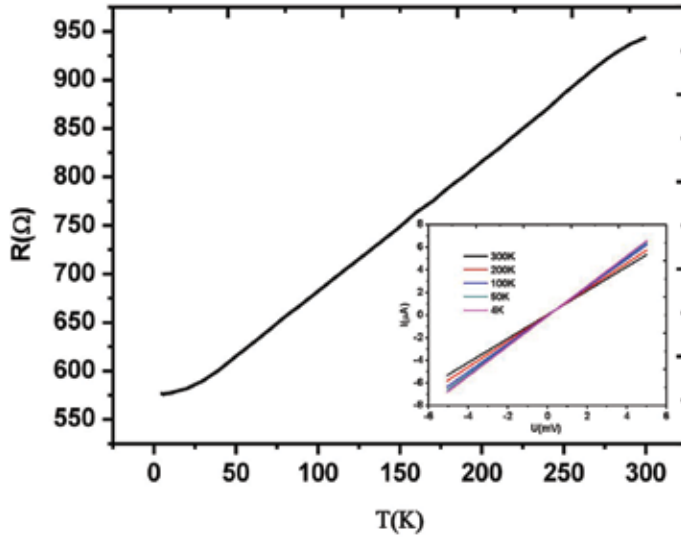
Figure 5. Temperature-dependent electrical resistance measurement result of Bi_2Te_3 hall bar device.

in the temperature range between 4 and 2 K. The reason, where the transport is primarily governed by combination of surface states and impurity band conduction is considered to be bulk carrier's freeze out effect. To the previous literature on Bi_2Se_3 grown on Si substrate [38], this temperature dependent result is quite similar. The Current-Voltage curves at different temperature, indicating ohmic contacts over the whole range of temperatures is shown in the insert in the **Figure 5**.

5. Conclusion

In the summary, in our fabricated topological insulator Bi_2Te_3 thin film Hall Bar device, we report the observation of weak antilocalization (WAL) behavior and linear magnetoresistance (LMR). The WAL characteristics is found to be in the low temperature and in the low magnetic field region and the LMR is considered to be accompanied with gapless energy spectrum of surface Dirac fermions and is believed to be quantum origin. A dip near 0 T magnetic fields is observed in the magnetoresistance (MR) characteristics of Bi_2Te_3 thin film hall Bar device. The originated dip is from the WAL effect and is found to be at low temperatures. By fitting to the HLN model for 10 nm thin film, we also derive relatively large phase breaking length of 155.8 nm at 4 K. This dependence on the thickness of the thin film has a pronounced behavior, i.e., below a certain critical thickness there is no observable WAL behavior. In our study and analysis, we observe disappearance of WAL in <5 nm thickness film. The reason is the film of topological insulator is so thinned that it leads to an opening of the gap at the Dirac point and results in a degenerate, massive Dirac dispersion, which leads to the diminishment of surface transport, by the observing flatness in the magnetoresistance curve.

Acknowledgements

Author details

Sunil Kumar Pradhan[1]* and Ranjan Barik[2]

*Address all correspondence to: sunilpradha@gmail.com

1 Department of Engineering and System Science, National Tsing Hua University, Hsinchu, Taiwan (ROC)

2 Microwave Tube Division, CSIR-Central Electronics Engineering Research Institute, Pilani, Rajasthan, India

References

[1] Langbehn J, Peng Y, Trifunovic L, von Oppen F, Brouwer PW. Physical Review Letters. 2017;**119**:246401

[2] Song Z, Fang Z, Fang C. Physical Review Letters. 2017;**119**:246402

[3] Benalcazar WA, Bernevig BA, Hughes TL. Science. 2017;**61**:357

[4] Chiu C-K, Teo JCY, Schnyder AP, Ryu S. Reviews of Modern Physics. 2016;**88**:035005

[5] Xu Y, Chiu J, Miao L, He H, Alpichshev Z, Kapitulnik A, Biswas RR, Wray LA. Nature Communications. 2017;**8**:14081

[6] Lee I, Kim CK, Lee J, Billinge SJ, Zhong R, Schneeloch JA, Liu T, Valla T, Tranquada JM, Gu G, Davis aJ CS. Proceedings of the National Academy of Sciences of the United States of America. 2015;**112**:1316

[7] Lau A, van den Brink J, Ortix C. Physical Review B. 2016;**94**:165164

[8] Chen J, He XY, Wu KH, Ji ZQ, Lu L, Shi JR, Smet JH, Li YQ. Physical Review B. 2011;**83**:241304

[9] Onose Y, Yoshimi R, Tsukazaki A, Yuan H, Hidaka T, Iwasa Y, Kawasaki M, Tokura Y. Applied Physics Express. 2011;**4**:083001

[10] Qu F, Yang F, Chen J, Shen J, Ding Y, Lu J, Song Y, Yang H, Liu G, Fan J, Li Y, Ji Z, Yang C, Lu L. Physical Review Letters. 2011;**107**:016802

[11] Murani A, Kasumov A, Sengupta S, Kasumov YA, Volkov VT, Khodos II, Brisset F, Delagrange R, Chepelianskii A, Deblock R, Bouchiat H, Gu'eron S. Nature Communications. 2017;**8**:15941

[12] Black-Schaffer AM, Balatsky AV, Fransson J. Physical Review B. 2015;**91**:201411

[13] Deb O, Soori A, Sen D. Journal of Physics. Condensed Matter. 2014;**26**:315009

[14] He H et al. Applied Physics Letters. 2012;**100**:032105

[15] Tang H, Liang D, Qiu RLJ, Gao XPA. ACS Nano. 2011;**5**:7510

[16] Li W, Claassen M, Chang C-Z, Moritz B, Jia T, Zhang C, Rebec S, Lee J, Hashimoto M, Lu D-H, Moore RG, Moodera JS, Devereaux TP, Shen Z-X. Scientific Reports. 2016;**6**:32732

[17] Wang XL, Du Y, Du SX, Zhang C. Physical Review Letters. 2012;**108**:266806

[18] Zhang GH, Qin HJ, Teng J, Guo JD, Guo Q, Dai X, Fang Z, Wu KH. Applied Physics Letters. 2009;**95**:053114

[19] He H et al. Applied Physics Letters. 2012;**100**:032105

[20] Kim D, Syers P, Butch NP. Nature Communications. DOI: 10.1038/ncomms3040. https://www.nature.com/articles/ncomms3040.pdf

[21] Yan Y et al. Applied Physics Letters. 2013;**103**:033106

[22] Zhang G, Qin H. Advanced Functional Materials. 2011;**21**:2351

[23] Chang C-Z, Tang P, Wang Y-L, Feng X, Li K, Zhang Z, Wang Y, Wang L-L, Chen X, Liu C, Duan D, He K, Ma X-C, Xue Q-K. Physical Review Letters. 2014;**112**:056801

[24] Chang C-Z, Zhao W, Kim DY, Zhang H, Assaf BA, Heiman D, Zhang S-C, Liu C, Chan MH, Moodera JS. Nature Materials. 2015;**14**:473

[25] Steinberg H, Laloe JB, Fatemi V, Moodera JS, Jarillo-Herrero P. Physical Review B. 2011;**84**:233101

[26] Ma Y, Kou L, Dai Y, Heine T. Physical Review B: Condensed Matter and Materials Physics. 2016;**94**:201104

[27] Qi XL, Zhang SC. Reviews of Modern Physics. 2011;**83**:1057

[28] Bian G, Wang Z, Wang XX, Xu C, Xu S, Miller T, Hasan MZ, Liu F, Chiang TC. ACS Nano. 2016;**10**:3859-3864

[29] Ando Y, Fu L. Annual Review of Condensed Matter Physics. 2015;**6**:361-381

[30] Hikami S, Larkin AI, Nagaoka Y. Progress in Theoretical Physics. 1980;**63**:707

[31] Wang W, Du Y. Scientific Reports. 2013;**3**:2181

[32] Niu C, Buhl PM, Bihlmayer G, Wortmann D, Blügel S, Mokrousov Y. Nano Letters. 2015;**15**:6071-6075

[33] Zhang RW, Zhang CW, Ji W-X, Li P, Yan S-S, Wang P-J. Scientific Reports. 2016;**6**:21351

[34] Zhang R-W, Zhang C-W, Ji W-X, Li P, Wang P-J, Yan S-S. Applied Physics Letters. 2016;**109**:182109

[35] Luo W, Xiang H. Nano Letters. 2015;**15**:3230-3235

[36] Zhou L, Shi W, Sun Y, Shao B, Felser C, Yan B, Frauenheim T. 2D Mater. 2016;**3**:035018

[37] Si C, Jin K-H, Zhou J, Sun Z, Liu F. Nano Letters. 2016;**16**:6584-6591

[38] Zhao J, Li Y, Ma J. Nanoscale. 2016;**8**:9657-9666

Light Devices

Growth Mode and Characterization of Si/SiC Heterostructure of Large Lattice-Mismatch

Lianbi Li

Additional information is available at the end of the chapter

Abstract

The Si/6H-SiC heterostructure of large lattice mismatch follows domain epitaxy mode, which release most of the lattice-mismatch strain, and the coherent Si epilayers can be grown on 6H-SiC. An interfacial misfit dislocation array is present at the interface that determines the domain's size. In this chapter, transmission electron microscopy (TEM) and high resolution X-ray diffraction (HRXRD) were employed to reveal in-plane orientation, interface structure and growth mode of the Si/SiC heterostructure. Based on the characterizations, residual lattice mismatch and edge misfit dislocation density at the hetero-interface can be precisely controlled. And these characterization methods are applicable for the heterostructures of large-lattice mismatch, except for the heterostructures with different crystal symmetry on the film and the substrate.

Keywords: large lattice mismatch, domain matching mode, SiC-based heterostructure, in-plane orientation, Interface micro-structure

1. Introduction

With advantageous material properties such as a wide bandgap and high thermal conductivity, silicon carbide (SiC) has attracted much attention for its wide applications in the photoelectric devices of high temperature and high power [1–5]. However, due to the wide bandgap, SiC-based photoelectric devices can be only driven by ultraviolet (UV) light, which essentially limits the application of visible and infrared light detection. Si/SiC heterostructure is suggested to make SiC-based devices to be light-activated by non-UV light, in which Si is used as a non-UV light absorption layer [6, 7]. In our previous work, it was found that the Si films on SiC substrates always have a polycrystalline structure with multiple orientations, while the preferential growth of the Si films with different orientations can be obtained at different growth

temperature [8–12]. The interface-structure of the heterostructure determines some important parameters such as the preferential orientation [13, 14], the interface state density [15–17] and the carrier mobility, which have significant impact on the heterostructure device performance. By observation of the Si/SiC interface-structure with different growth temperatures, the growth mode of the Si/SiC heterostructure can be revealed, and the accurate control of the growth orientation may be achieved. At present, the studies of the SiC-based Si/SiC heterostructure just focused on the electrical performance of the heterostructures in SiC SBD [18] and SiC MOSFET [19, 20], the growth mode and interface-structure of the Si/SiC heterostructure is rarely reported.

2. Growth mode, interface micro-structure and in-plane orientation of the Si/SiC heterostructure

2.1. Growth mode of the heterostructures of large lattice-mismatch

The crystal structure of Si and 6H-SiC is face-centered cubic (FCC) and hexagonal close-packed (HCP) with in-plane lattice constants of $a_{Si} = 5.430$ Å and $a_{SiC} = 3.081$ Å, respectively. The lattice mismatch of the Si(111)/6H-SiC(0001) is as large as 19.8%, which is given by

$$\varepsilon_x = \varepsilon_y = \left(a_{sic(0001)} - a_{Si(111)} \right) / a_{Si(111)} \tag{1}$$

where $a_{sic(0001)}$ and $a_{Si(111)}$ are the lattice constants of the SiC(0001) and Si(111) crystalline planes, respectively. If the lattice mismatch of the heterostructure is sufficiently low, the mismatch strain can be released by interfacial atomic relaxation of the heterostructure, and the strained-layer heterostructure with no interfacial misfit dislocations (MD) will be attained. However, the Si/SiC heterostructure has a large lattice mismatch, the epitaxial growth is still followed except that domain matching (DM) mode [21] in order to reduce the mismatch, and therefore an interfacial MD array is present at the interface that determines the domain's size [22–26]. A schematic illustration of mechanisms for accommodation of lattice mismatch strain in large-mismatch systems with domain epitaxial growth is shown in **Figure 1**. And this matching mode is applicable for the heterostructures with similar crystal symmetry on the film and the substrate. In the Si/6H-SiC system, domains consisting of m lattice constants of the Si film match with n of the SiC substrate. During domain matching system, the domain size na_{sic} of the SiC substrate does not match perfectly with ma_{Si} of the Si film and thus a residual domain mismatch strain is present in the film in the x direction, given by

$$\varepsilon_x = (m a_{sic\,x} - n a_{Si\,x}) / n a_{Si\,x} \tag{2}$$

Similarly, the residual strain

$$\varepsilon_y = \left(p a_{sic\,y} - q a_{Si\,y} \right) / q a_{Si\,y} \tag{3}$$

where p and q are integers, is present in the y direction. The lattice-mismatch of the Si/6H-SiC heterostructure calculated with the DM mode are very small, the coherent Si epilayer can be
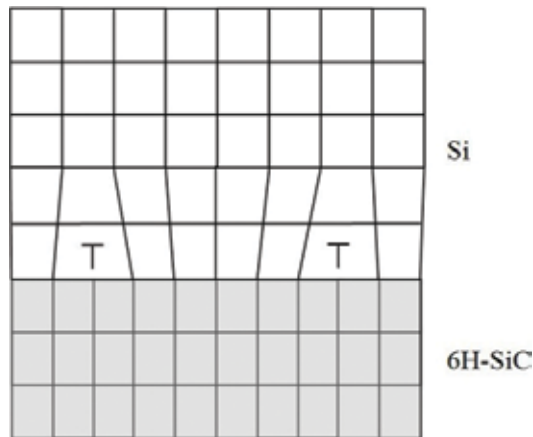
Figure 1. Schematic illustration of mechanisms for accommodation of lattice mismatch strain in large mismatch systems with DM mode.

grown on 6H-SiC. This type of edge misfit dislocation is also observed in other heterostructure of large lattice-mismatch, such as TiN/Si [23], ZnO/α-Al$_2$O$_3$ [23], Sc$_2$O$_3$/GaN [24], GaAs/Si [25] and In$_x$Ga$_{1-x}$N/GaN [26].

2.2. Interface micro-structure of the Si/SiC heterostructure

The low magnification cross-sectional transmission electron microscopy (TEM) bright-field image of the Si thin film grown on 6H-SiC(0001) at 900°C is shown in **Figure 2(a)**. In this image, the lower part belongs to the 6H-SiC substrate, while the upper part represents the Si thin film. The Si film with a thickness of about 0.55 μm shows irregular heterogeneous diffraction contrast, which suggests the existence of some structural defects such as stacking faults (SF) and twins in the film, as labeled in **Figure 2(a)**. The selected area electron diffraction (SAED) patterns of the Si/6H-SiC heterostructure corresponding to Si[-110]SiC[-12-10] zone axes are shown in **Figure 2(b)**. It is confirmed that the Si film has epitaxial connection with the 6H-SiC substrate and the orientation relationship of Si/6H-SiC heterostructure is (111)[1-10]$_{Si}$// (0001)[1-210]$_{6H-SiC}$. Alignment of the diffraction spots indicates that FFC-on-HCP epitaxial orientation, i.e., (111)$_{Si}$//(0001)$_{6H-SiC}$ is maintained at a growth temperature of 900°C. It should be pointed out that the extinction diffraction spots of (10-10)$_{SiC}$ and (10-16)$_{SiC}$ can be observed in the SAED patterns because of the multiple diffraction. A superposition of two FCC <110> zone diffraction patterns, which are symmetrical to each other with respect to the (111) mirror plane, indicating that the lamellar structure observed in the film consists of alternate stacks of twins, as shown in **Figure 2(b)**. Furthermore, the faint diffused streaks along the <111> orientation indicate that there exist a large number of SFs. And this agrees with the results of the diffraction contrast study.

Figure 3(a) shows a high-resolution TEM image of the Si/6H-SiC interface, exhibiting interfaces of Si(111)/6H-SiC(0001) without any indication of interfacial reactions, however, it is not crystallographic sharp, which reflects the roughness of the Si layer's surface and the poor
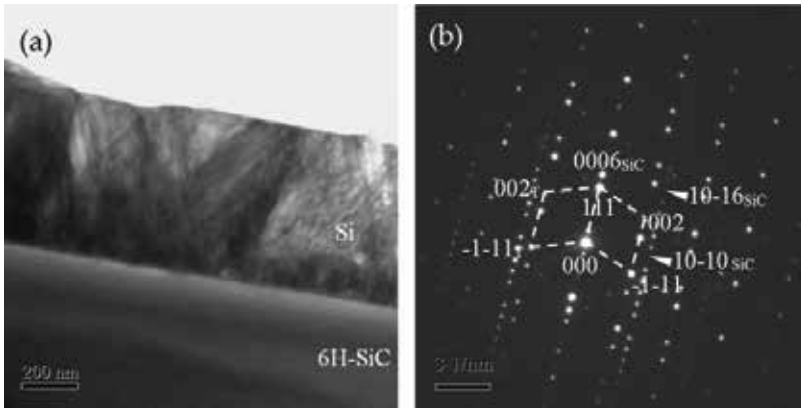
Figure 2. Cross-sectional low magnification TEM image and the SAED patterns of Si films grown on 6H-SiC (0001) at 900°C. (a) TEM image, (b) SAED patterns corresponding to Si[-110]SiC[-12-10] zone axes.

crystallographic match between interatomic distances in close-packed layers of between Si (111) and SiC (0001) planes (in-plane constants 3.84 Å for Si and 3.08 Å for 6H-SiC). Moreover, typical structural defects such as SFs and twins are clearly observed in the Si film, which are labeled in **Figure 3(a)**. **Figure 3(b)** is the magnified image of the region b in **Figure 3(a)**, which further confirms the epitaxial relation of the Si/6H-SiC heterostructure. Fourier-filtering technique is applied to remove the non-periodic information such as background signal and the structural defects in the Si film. The Fourier-filtered high-resolution TEM images of the Si thin film, the 6H-SiC substrate and the Si/6H-SiC interface are shown in **Figure 3(c)**–**3(e)**, respectively. It is clearly observed that the SiC substrate with the HCP stacking sequence as ABCACB has a crystal plane spacing of 2.57 Å, while the Si film with the FCC stacking as ABC has a crystal plane spacing of 3.21 Å. Calculated from the crystal plane spacing, lattice mismatch of the Si(111)/6H-SiC(0001) heterostructure is about 19.8%, which is in accordance with the calculation results based on the fast-Fourier transform (FFT) pattern. Nevertheless, the (0001) lattice planes of SiC and (111) lattice planes of Si are well aligned, and the Si film grows epitaxially but with MDs (indicated by the arrows) at the interface between the Si film and the 6H-SiC substrate, which can be easily identified by extra lattice fringes in the 6H-SiC. The Si epitaxial growth follows the DM mode, every five 6H-SiC(1-210) planes match with four Si (1-10) planes along the interface, as shown in **Figure 3(e)**. Moreover, the invariant crystal plane spacings of the Si film and the 6H-SiC substrate at the Si/6H-SiC interface demonstrate that the interfacial MD array accommodates most of the lattice mismatch strain and makes the lattice coincident at the Si/6H-SiC interface.

Based on the results shown above, the in-plane orientation of the $(111)_{Si}//(0001)_{6H-SiC}$ heterostructure is schematically shown in **Figure 4(a)**. Both of the 6H-SiC(0001) and Si(111) lattice planes have the same triangular lattice in two-dimensions (2D). And the Si(111) layers epitaxially grow on 6H-SiC(0001) without rotation of the 2D triangular lattice. However, the in-plane lattice constant of the Si(111) (3.84 Å) is larger than that of the 6H-SiC(0001) (3.08 Å), as shown in **Figure 4(b)**. The FCC-on-HCP epitaxial relationship with a four-to-five mode of Si-to-SiC is clearly observed. The residual mismatch calculated by the DM mode is only 0.26%,
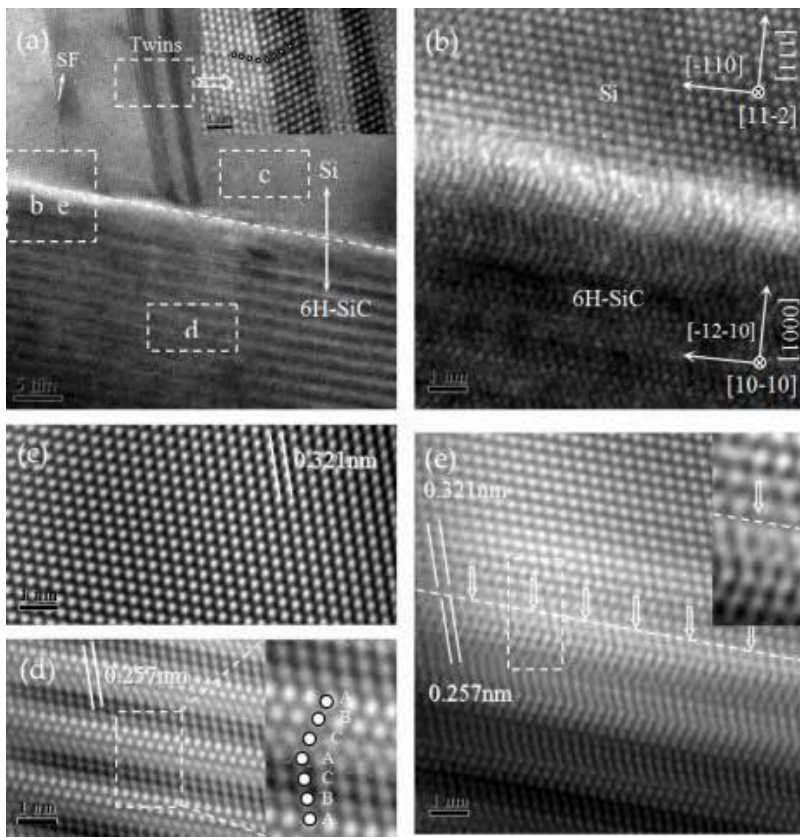
Figure 3. A HRTEM image of the Si/6H-SiC heterojunction grown at 900°C (a), a magnified image (b), and the Fourier-filtered HRTEM images (c)–(e).

which is much smaller than the mismatch of 19.8% calculated by the conventional lattice matching (LM) mode. Because the 2D triangular lattice of the Si(111) film has no rotation during epitaxial growth on 6H-SiC(0001), the domain mismatch strain ε_x in the x direction and ε_y in the y direction are the same as 0.26%.

XRD data, shown elsewhere [9], indicates that the Si phase with [110] orientation appears when the temperature increases higher than 1000°C, which is confirmed by the TEM characterizations. **Figure 5(a)** is a low magnification cross-sectional TEM image of the Si/6H-SiC(0001) heterostructure grown at 1050°C. The Si/SiC heterostructure has a sharp interface and consist of columnar grains. SAED patterns at the Si/6H-SiC interface corresponding to Si[-110]SiC[1-210] zone axes in **Figure 5(b)** clearly show the FCC-on-HCP orientation relationship of $(110)[001]_{Si}//(0001)[10-10]_{6H-SiC}$, confirming the epitaxial growth of the Si films with [110] orientation. The high-resolution TEM image of the Si(110)/SiC(0001) heterostructure is shown in **Figure 6(a)**. The Si/SiC interface is crystallographic sharp without any indication of the interfacial reaction products. **Figure 6(b)** is the Fourier-filtered HRTEM image, which confirms the epitaxial connection of the Si/6H-SiC heterostructure. Calculated from the crystal plane
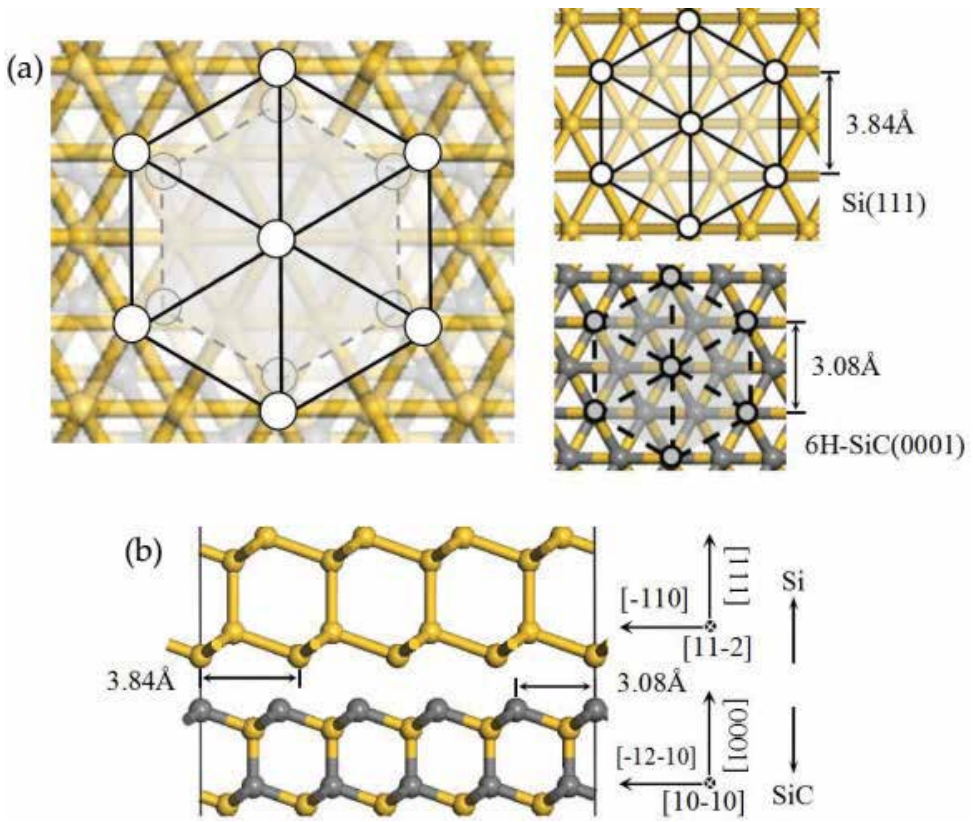
Figure 4. Schematic diagrams of the of Si(111)/6H-SiC(0001) heterojunction. (a) In-plane orientation, (b) atomic structure at the hetero-interface. The insets show the atomic structures of the Si(111) and 6H-SiC(0001) planes.
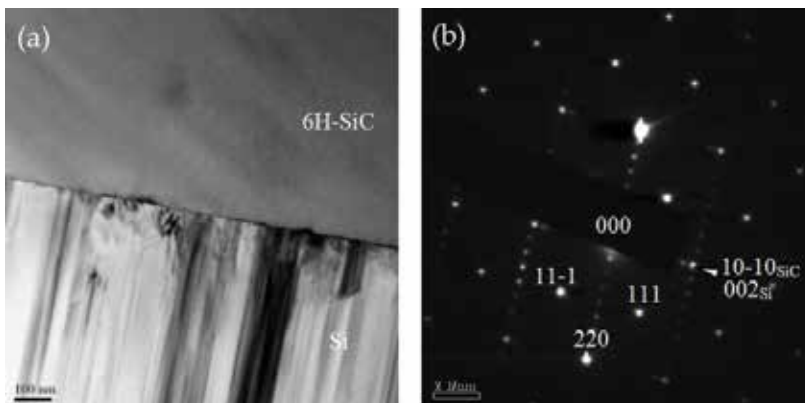

Figure 5. Low magnification cross-sectional TEM image and the SAED patterns of Si films grown on 6H-SiC(0001) at 1050°C. (a) TEM image, (b) SAED patterns of the Si/SiC interface corresponding to Si[-110]SiC[1-210] zone axes.
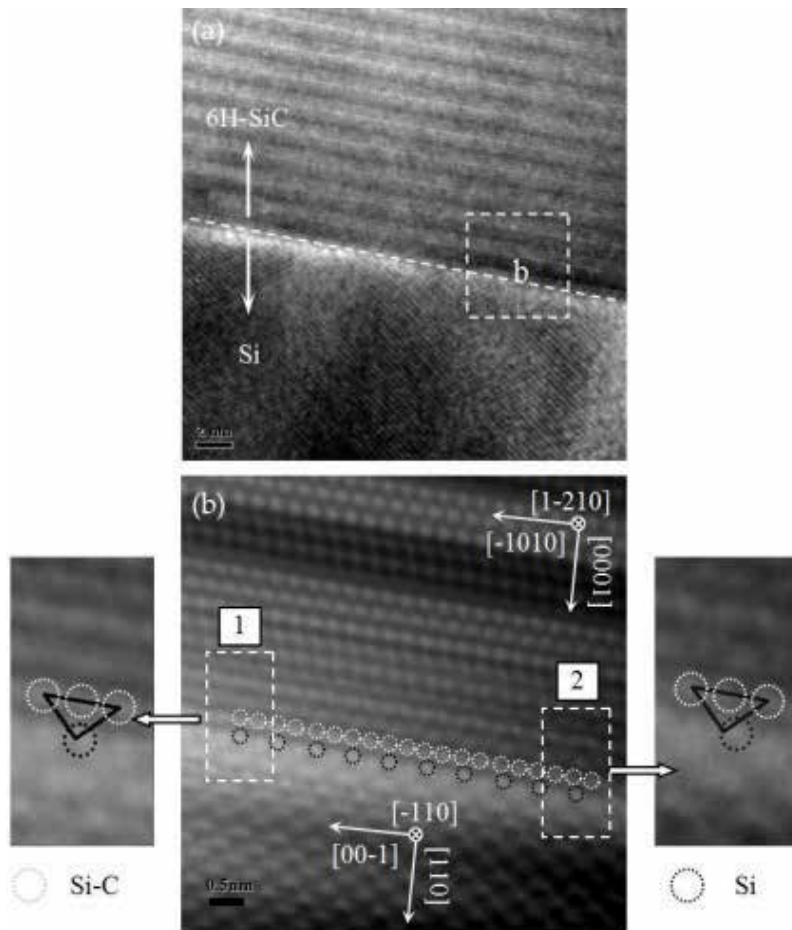
Figure 6. A HRTEM image of the Si/6H-SiC heterojunction grown at 1050°C (a), the Fourier-filtered HRTEM images (b). The insets are the magnified images of region 1 and 2, which show the atomic position of the Si/6H-SiC interface. The atomic positions of Si are slightly different in two regions. It suggests that the Si-to-SiC matching mode at the interface is long-periodic and is merely approximate 1:2.

spacings and the FFT patterns, lattice mismatch of the Si(110)/6H-SiC(0001) heterostructure is 1.84%. The interfacial MD array can also be observed by extra lattice fringes in the 6H-SiC. Every two 6H-SiC(10-10) planes match with one Si(001) planes along the interface, as shown in **Figure 6(b)**. Compared with the Si(111)/6H-SiC(0001) heterostructure with a residual mismatch of 0.26%, the Si(110)/6H-SiC(0001) heterostructure has higher residual mismatch of 1.84% along Si[001]SiC[10-10] orientation. If the Si-to-SiC matching mode is not 1:2 but a long-period structure of 53:54, the lattice mismatch can decrease to −0.55%. Of course the long-period matching is very difficult to be confirmed by experimental observations; however, the trend of this large-period matching can be observed in **Figure 6(b)**. The atomic position of Si in region 1 is slightly different from that of Si in region 2, as shown in the insets. It is suggested that the Si-to-SiC matching at the interface is merely approximate 1:2.

Figure 7(a) shows a HRTEM image of the Si(110)/6H-SiC(0001) interface. Because the observation orientation is SiC[-1010], the 6H stacking sequence as ABCACB of 6H-SiC is not observed. The SAED patterns at the Si/6H-SiC interface corresponding to Si[00-1]SiC[-1010] zone axes are shown in **Figure 7(b)**. SAED patterns at the Si/6H-SiC interface clearly show the FCC-on-HCP orientation relationship of (110)[-110]Si//(0001)[1-210]6H-SiC, confirming the epitaxial growth of the Si films with [110] growth orientation. **Figure 7(c)** shows the Fourier-filtered image of region 1, which further confirms the epitaxial connection of the Si(110)/6H-SiC(0001) heterostructure. The crystal plane spacing at the Si/6H-SiC interface also has no significant change. The Si epitaxial growth follows the DM mode, every five 6H-SiC(1-210) planes match with four Si(-110) planes along the interface, as shown in **Figure 7(d)**. According to the extra SiC lattice planes at the hetero-interface, Burgers vectors of the MDs can be determined uniquely. The MDs are of the pure edge type with a Burgers vector of $\langle 1-210 \rangle_{SiC}/3$ parallel to the interface, which are labeled in **Figure 7(d)**.
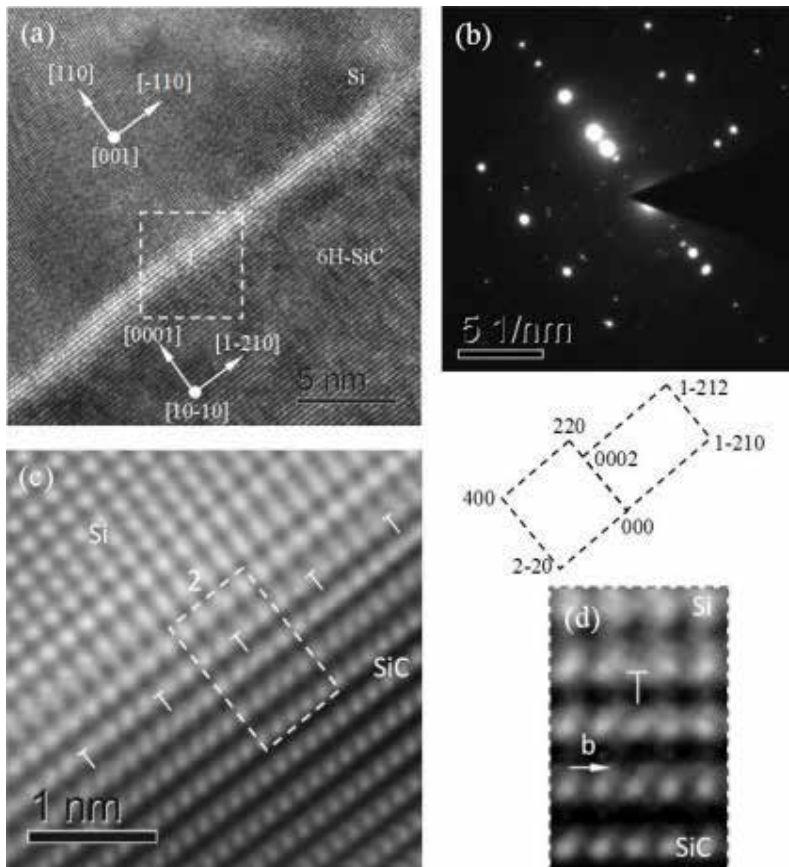

Figure 7. HRTEM images and the SAED patterns of Si(110)/6H-SiC(0001) interface. HRTEM image of the Si(110)/6H-SiC(0001) interface (a), SAED patterns (b), the Fourier-filtered HRTEM images of region 1 (c) and region 2 (d). The SAED patterns at the Si/6H-SiC interface corresponding to Si[00-1]SiC[-1010] zone axes.

Base on the HRTEM observations and SAED analysis, the lattice-structure model of the Si (110)/6H-SiC(0001) heterostructure is constructed and schematically shown in **Figure 8**. It is known that the Si(110) plane has a rectangular 2D lattice with different in-plane constants of 5.43 Å and 3.84 Å along the vertical orientations Si[001] and Si[-110], which is different from the 2D triangular lattice of the 6H-SiC(0001). However, the triangular lattice of 6H-SiC(0001) can be transformed to rectangular 2D lattice by missing partial Si-C atoms, which has in-plane constants of 5.33 Å and 3.08 Å along SiC[10-10] and SiC[1-210] respectively, as shown in **Figure 8(a)**. Along Si[001]SiC[10-10] orientations, the heterostructure has a lattice mismatch of 1.84% with in-plane constants 5.43 Å for Si and 5.33 Å for 6H-SiC. The residual lattice mismatch strain can be released by interfacial atomic relaxation of the Si/6H-SiC heterostructure and the strained-layer with no MDs will be attained. However, the 2D rectangular lattice of 6H-SiC(0001) is converted from the triangular lattice by missing every other Si-C atoms along [10-10] orientation. Therefore, MDs are still present at the Si(110)/6H-SiC(0001) interface and 1:2 mode of Si-to-SiC is observed. Along the vertical orientations Si[-110]SiC[1-210], the Si (110)/6H-SiC(0001) heterostructure has in-plane constants 3.84 Å for Si and 3.08 Å for 6H-SiC, and the interface with a four-to-five mode of Si-to-SiC is shown in **Figure 8(c)**, which is identical with the Si(111)/6H-SiC(0001) heterostructure.
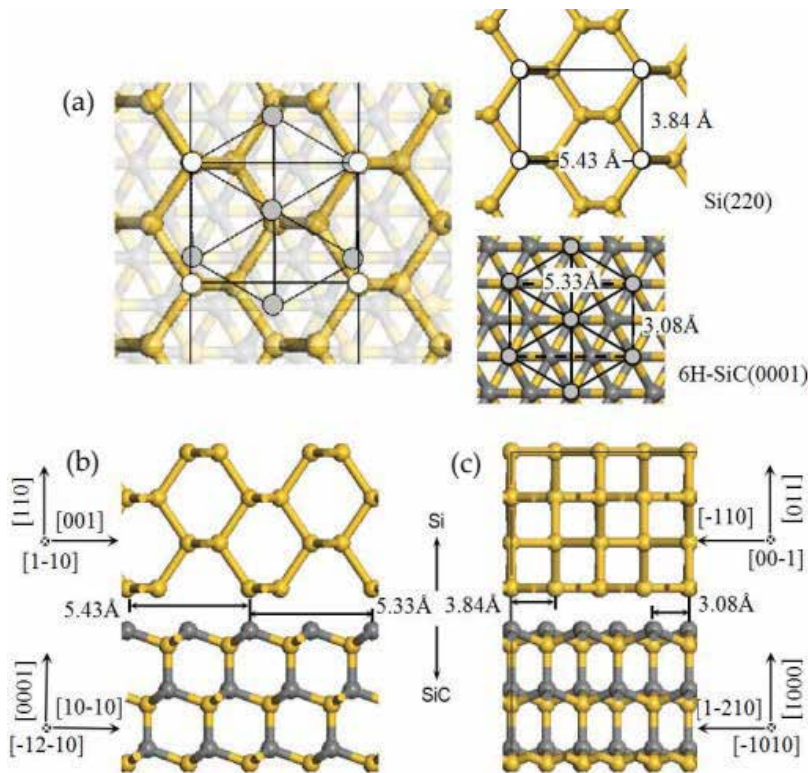

Figure 8. Schematic diagrams of the of Si(110)/SiC(0001) heterojunction. In-plane orientation (a), atomic structure at the interface along Si[001]SiC[10-10] (b) and Si[-110]SiC[1-210] (c). The insets show the atomic structures of the Si(110) and 6H-SiC(0001) planes.

Because of the large lattice mismatch strain, the conventional LM epitaxy is not expected. The lattice mismatch between 6H-SiC and Si is totally accommodated by MDs rather than by uniform elastic strains, the DM mode is observed.

2.3. In-plane orientation of the Si/SiC heterostructure

Figure 9 shows the XRD θ-2θ scans for Si/SiC(0001) heterostructures prepared at 900°C and 1050°C, respectively. It is shown that the Si film is [111] oriented when the Si layer is deposited at the lower temperatures of 900°C, as the growth temperature increase to 1050°C, the Si layer is mainly [110] oriented, which agrees with the SAED characterizations.

The in-plane orientation at the hetero-interface was carefully examined using X-ray phi(φ) scan. For investigating the [11-2] orientation in Si(111) plane, the out-of-plane orientation [110] must be confirmed, as demonstrated in **Figure 10**. **Figure 11(a)** shows XRD 360° φ scans of the Si(110) (χ = 35.27°) reflections of Si(111)/6H-SiC(0001) heterostructure grown at 900°C. Moreover, for investigating [10-10] orientation in 6H-SiC(0001) plane, the φ scans from the 6H-SiC(10-11) (χ = 80°) reflections are also characterized. Narrow and intense peaks with six-fold symmetry are observed. On the basis of the Si(110) and 6H-SiC(10-11) reflections shown in **Figure 11(a)**, it can be concluded that a FCC-on-HCP parallel epitaxy is achieved at 900°C and the in-plane orientation relationship is $(111)[1\text{-}10]_{Si}//(0001)[1\text{-}210]_{6H\text{-}SiC}$. The in-plane orientation of the Si(110)/6H-SiC(0001) heterostructure grown at 1050°C is also characterized, as shown in **Figure 11(b)**. For investigating the [001] orientation in Si(110) plane, the out-of-plane orientation [111] is confirmed firstly. The six-fold symmetry is also observed. It is confirmed that the in-plane orientation relationship is $(110)[001]_{Si}//(0001)[10\text{-}10]_{6H\text{-}SiC}$.

By means of the in-plane orientation characterizations, the 3D Si/SiC(0001) hetero-interface structures with different orientations are confirmed and schematically shown in **Figure 12**. The Si(111) layers grow epitaxially on 6H-SiC(0001) with an in-plane orientation relationship of Si [11-2]//SiC[10-10], as shown in **Figure 12(a)**. As mentioned above, the Si(111)/SiC(0001) heterostructure follows DM mode, the epitaxial growth is described by 4 (111) interatomic distances of Si matching with 5 (0001) interatomic distances of 6H-SiC, which releases most of the lattice-mismatch strain. The 4:5 matching generates edge-MD array at the Si/6H-SiC interface [13], and the MD density can be calculated as 4.87×10^{13} cm^{-2} according to the model
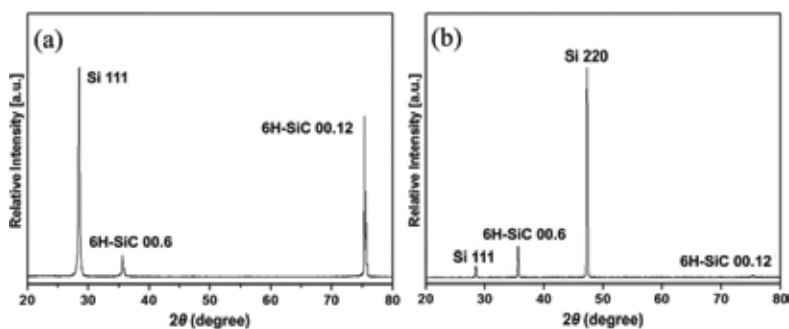

Figure 9. X-ray θ-2θ scans for Si/SiC(0001) heterostructures with the Si layer grown at (a) 900°C and (b) 1050°C.
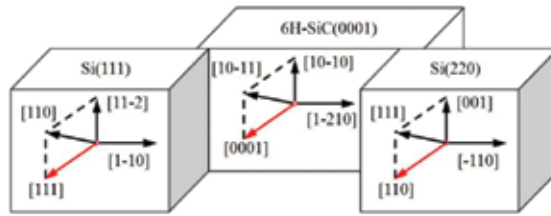
Figure 10. XRD φ scans schematic diagrams of the Si(111)/6H-SiC(0001) and Si(110)/6H-SiC(0001) heterostructures. For investigating the in-plane orientations, at least one out-of-plane orientation needs to be confirmed firstly.
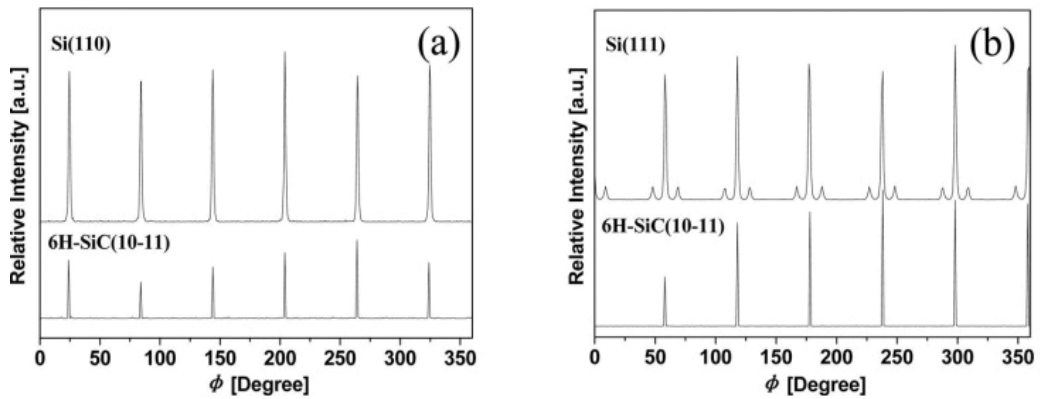

Figure 11. XRD φ scans of the Si/6H-SiC heterostructures, (a) Si(110) ($\chi = 35.27°$) reflections of Si(111)/6H-SiC(0001) heterostructure grown at 900°C, (b) Si(111) ($\chi = 35.27°$) reflections of Si(110)/6H-SiC(0001) heterostructure grown at 1050°C. The φ scans from the 6H-SiC(10-11) ($\chi = 80°$) reflections is also shown as reference at the bottom.

shown in **Figure 12(a)**, which is much smaller than the theoretical value (4.34×10^{14} cm^{-2}). However, the domain size na_{sic} of the SiC substrate ($n = 5$) does not match perfectly with ma_{Si} of the Si film ($m = 4$), and thus a residual domain mismatch strain ε, given by Eq. (2) is present in the film. The residual mismatch strain ε of the Si(111)/6H-SiC(0001) heterostructure calculated with the DM mode is 0.26%, which is much smaller than conventional LM mode (19.8%). The Si(110) layers epitaxial grow on 6H-SiC(0001) with an in-plane orientation of Si[-110]//SiC [1-210], and the crystal structure model is schematically shown in **Figure 12(b)**. Along orientations Si[-110]SiC[1-210], the Si(110)/6H-SiC(0001) heterostructure has in-plane constants 3.84 Å for Si and 3.08 Å for 6H-SiC, and the interface with a four-to-five mode of Si-to-SiC is identical with the Si(111)/6H-SiC(0001) heterostructure. Along the vertical Si[001]SiC[10-10] orientations, the distinct 1:2 matching is observed and thus MDs are still present at the Si(110)/6H-SiC(0001) interface. The MD density increases to 1.217×10^{14} cm^{-2} correspondingly, which is still smaller than the theoretical value (2.57×10^{14} cm^{-2}). The heterostructure has a residual mismatch strain ε of 1.84% with in-plane constants 5.43 Å for Si and 5.33 Å for 6H-SiC (**Table 1**).
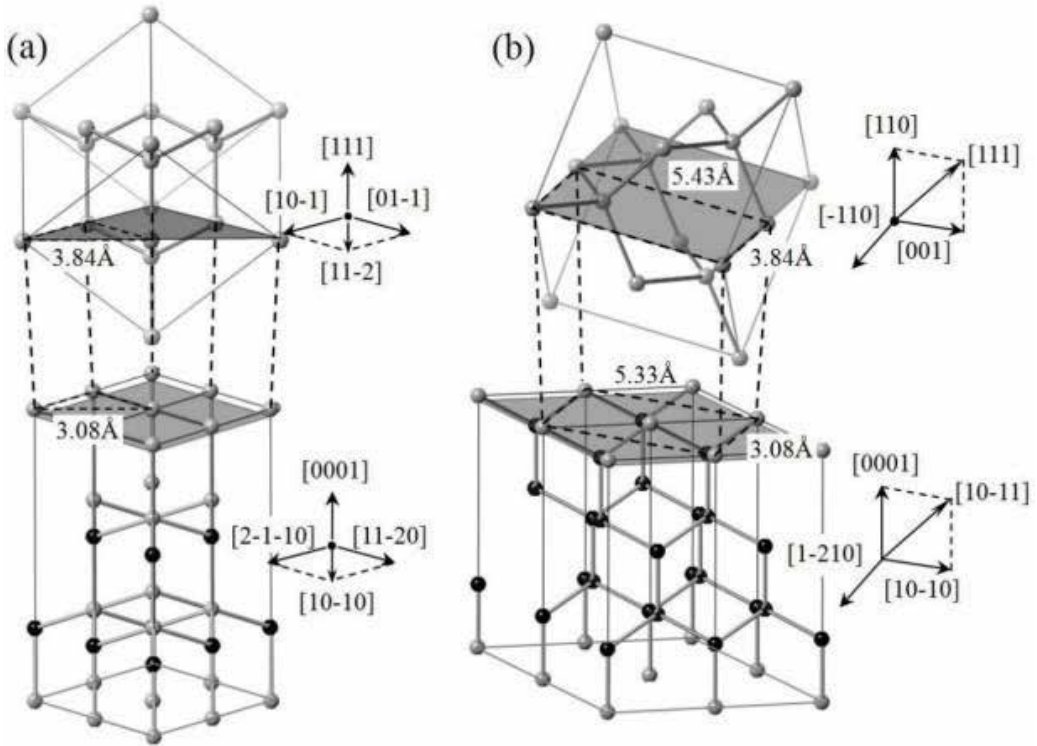
Figure 12. Schematic diagrams of the Si/6H-SiC(0001) heterojunction. Si/6H-SiC heterostructure with the [111] preferential orientation (a), Si/6H-SiC heterostructure with the [110] preferential orientation (b). As the preferential orientations are [111] and [110], the in-plane orientations are Si[01-1]//SiC[11-20] and Si[001]//SiC[10-10], respectively.

Growth orientation	Si-to-SiC DM mode		Residual mismatch		MD density theoretical value	MD density DM mode
Si(111)/6H-SiC(0001)	Si[11-2] SiC [10-10]	Si[1-10] SiC [1-210]	Si[11-2] SiC [10-10]	Si[1-10] SiC [1-210]	4.34×10^{14} cm^{-2}	0.487×10^{14} cm^{-2}
	4:5	4:5	0.26%	0.26%		
Si(110)/6H-SiC(0001)	Si[001] SiC [10-10]	Si[-110] SiC [1-210]	Si[001] SiC [10-10]	Si[-110] SiC [1-210]	2.57×10^{14} cm^{-2}	1.217×10^{14} cm^{-2}
	1:2	4:5	1.84%	0.26%		

The lattice-mismatch of the Si/6H-SiC heterostructure calculated with the domain matching model.

Table 1. Basic semiconductor properties of the Si/6H-SiC interface.

3. Conclusions

In this chapter, Si/SiC heterostructures with different orientations were prepared on 6H-SiC(0001) by LPCVD. The heterostructure of large lattice-mismatch grows by DM mode,

which releases most of the lattice-mismatch strain, and the coherent Si epilayers can be grown on 6H-SiC. Si(111)/6H-SiC(0001) heterostructure obtained at 900°C has an in-plane orientation relationship of $(111)[1\text{-}10]_{Si}//(0001)[1\text{-}210]_{6H\text{-}SiC}$. The Si(111)/6H-SiC(0001) interface has the 4:5 Si-to-SiC matching mode with a residual lattice-mismatch of 0.26% along both the Si[11-2] and Si[1-10] orientations. As the growth temperature increases to 1050°C, the preferential orientation of the Si film transitions to [110]. SAED patterns show that the in-plane orientation relationship is $(110)[001]_{Si}//(0001)[10\text{-}10]_{6H\text{-}SiC}$. Along Si[-110] orientation, the Si-to-SiC matching is still 4:5; along the vertical orientation Si[001], the matching mode is approximate 1:2 and the residual mismatch is 1.84% correspondingly. The atom quantity in one DM period decreases with increasing residual mismatch and vice versa. The Si film epitaxially grows but with MDs at the Si/6H-SiC interface. The MD density of the Si(111)/6H-SiC(0001) and Si(110)/6H-SiC(0001) obtained by experimental observations is as low as 0.487 and 1.217×10^{14} cm^{-2}, respectively, which is much smaller than the theoretical value.

Acknowledgements

Conflict of interest

We declare that we have no financial and personal relationships with other people or organizations that can inappropriately influence our work.

Author details

Lianbi Li[1,2]*

*Address all correspondence to: xpu_lilianbi@163.com

1 School of Science, Xi'an Polytechnic University, Xi'an, China

2 Department of Electronic Engineering, Xi'an University of Technology, Xi'an, China

References

[1] Seely JF, Kjornrattanawanich B, Holland GE, Korde R. Response of a SiC photodiode to extreme ultraviolet through visible radiation. Optics Letters. 2005;**30**:3120-3122. DOI: 10.1364/OL.30.003120

[2] Xin X, Yan F, Koeth TW, Joseph C, Hu J, Wu J, Zhao JH. Demonstration of 4H-SiC visible-blind EUV and UV detector with large detection area. Electronics Letters. 2005;**41**:1192-1193. DOI: 10.1049/el:20052977

[3] Hu J, Xin X, Zhao JH, Yan F, Guan B, Seely J, Kjornrattanawanich B. Highly sensitive visible-blind extreme ultraviolet Ni/4H-SiC Schottky photodiodes with large detection area. Optics Letters. 2006;**31**:1591-1593. DOI: 10.1364/OL.31.001591

[4] Levinshtein ME, Ivanov PA, Agarwal AK, Palmour JW. Optical switch-on of silicon carbide thyristor. Electronics Letters. 2002;**38**:592-593. DOI: 10.1049/el:20020415

[5] Henning JP, Schoen KJ, Melloch MR, Woodall JM, Cooper JA. Electrical characteristics of rectifying polycrystalline silicon/silicon carbide heterojunctions. Journal of Electronic Materials. 1998;**27**:296-299. DOI: 10.1007/s11664-998-0403-x

[6] Li LB, Chen ZM, Ren ZQ, Gao ZJ. Non-UV photoelectric properties of the Ni/n-Si/N$^+$-SiC isotype heterostructure Schottky barrier photodiode. Chinese Physics Letters. 2013;**30**(9): 097304. DOI: 10.1088/0256-307X/30/9/097304

[7] Li LB, Chen ZM, Liu WT, Li WC. Electrical and photoelectric properties of p-Si/n$^+$-6H-SiC heterojunction non-ultraviolet photodiode. Electronics Letters. 2012;**48**:1227-1228. DOI: 10.1049/el.2012.1471

[8] Li LB, Chen ZM, Xie LF, Yang C. TEM characterization of Si films grown on 6H-SiC (0001) C-face. Materials Letters. 2013;**93**:330-332. DOI: 10.1016/j.matlet.2012.11.093

[9] Xie LF, Chen ZM, Li LB, Yang C, He XM, Ye N. Preferential growth of Si films on 6H-SiC(0001) C-face. Applied Surface Science. 2012;**261**:88-91. DOI: 10.1016/j.apsusc.2012.07.101

[10] Li LB, Chen ZM, Zang Y, Song LX, Han YL, Chu Q. Epitaxial growth of Si/SiC heterostructures with different preferred orientations on 6H-SiC(0001) by LPCVD. CrystEngComm. 2016;**18**:5681. DOI: 10.1039/c6ce00137h

[11] Li LB, Chen ZM, Zang Y, Feng S. Atomic-scale characterization of Si(110)/6H-SiC(0001) heterostructure by HRTEM. Materials Letters. 2016;**163**:47-51. DOI: 10.1016/j.matlet.2015.10.017

[12] Li LB, Chen ZM, Zang Y. Interface-structure of the Si/SiC heterojunction grown on 6H-SiC. Journal of Applied Physics. 2015;**117**:013104. DOI: 10.1063/1.4901644

[13] Wu WB, Wong KH, Choy CL. Epitaxial growth of SrTiO$_3$ films with different orientations on TiN buffered Si(001) by pulsed laser deposition. Thin Solid Films. 2000;**360**:103-106. DOI: 10.1016/S0040-6090(99)01091-3

[14] Sugawara Y, Shibata N, Hara S, Ikuhara Y. Interface structure of face-centered-cubic-Ti thin film grown on 6H-SiC substrate. Journal of Materials Research. 2000;**15**:2121-2124. DOI: 10.1557/JMR.2000.0305

[15] Wang K, Hattrick-Simpers JR, Bendersky LA. Phase transformation in an yttrium-hydrogen system studied by TEM. Acta Materialia. 2010;**58**:2585-2597. DOI: 10.1016/j.actamat.2009.12.045

[16] Tokuyuki T, Shiro H. Control of interface states at metal/6H-SiC(0001) interfaces. Physical Review B. 2004;**70**:035312. DOI: 10.1103/PhysRevB.70.035312

[17] Long C, Ustin SA, Ho W. Structural defects in 3C-SiC grown on Si by supersonic jet epitaxy. Journal of Applied Physics. 1999;**86**:2509-2515. DOI: 10.1063/1.371085

[18] Pérez-Tomás A, Jennings MR, Davis M, Covington JA, Mawby PA, Shah V, Grasby T. Characterization and modeling of n-n Si/SiC heterojunction diodes. Journal of Applied Physics. 2007;**102**:014505. DOI: 10.1063/1.2752148

[19] Pérez-Tomás A, Jennings MR, Davis M, Shah V, Grasby T, Covington JA, Mawby PA. High doped MBE Si p-n and n-n heterojunction diodes on 4H-SiC. Microelectronics Journal. 2007;**38**:1233-1237. DOI: 10.1016/j.mejo.2007.09.019

[20] Guy OJ, Jenkins TE, Lodzinski M, Castaing A, Wilks SP, Bailey P, Noakes TCQ. Ellipsometric and MEIS studies of 4H-SiC/Si/SiO_2 and 4H-SiC/SiO_2 interfaces for MOS devices. Materials Science Forum. 2007;**556–557**:509-512. DOI: 10.4028/www.scientific.net/MSF.556-557.509

[21] Tsvetanka Z, Jagannadham K, Narayan J. Epitaxial growth in large-lattice-mismatch systems. Journal of Applied Physics. 1994;**75**:860-871. DOI: 10.1063/1.356440

[22] Narayan J, Tiwari P, Chen X, Chowdhury R, Zheleva T. Epitaxial growth of TiN films on (100) silicon substrates by laser physical vapor deposition. Applied Physics Letters. 1992; **61**:1290-1292. DOI: 10.1063/1.107568

[23] Narayan J, Larson BC. Domain epitaxy: A unified paradigm for thin film growth. Journal of Applied Physics. 2003;**93**:278-285. DOI: 10.1063/1.1528301

[24] Niermann T, Zengler D, Tarnawska L, Stork P, Schroeder T, Lehmann M. Virtual GaN substrates via Sc_2O_3/Y_2O_3 buffers on Si(111): Transmission electron microscopy characterization of growth defects. Journal of Applied Physics. 2013;**113**:223501. DOI: 10.1063/1.4809561

[25] Otsuka N, Choi C, Nakamura Y, Nagakura S, Fischer R, Peng CK, Morkog H. High resolution electron microscopy of misfit dislocations in the GaAs/Si epitaxial interface. Applied Physics Letters. 1986;**49**:277-279. DOI: 10.1063/1.97140

[26] Lü W, Li DB, Li CR, Zhang Z. Generation and behavior of pure-edge threading misfit dislocations in $In_xGa_{1-x}N$/GaN multiple quantum wells. Journal of Applied Physics. 2004; **96**:5267-5270. DOI: 10.1063/1.1803633

Quantum Wells and Ultrathin Metallic Films

Victor Barsan

Additional information is available at the end of the chapter

Abstract

The chapter illustrates how simple quantum mechanics can sometimes provide quite precise description of nanophysics phenomena. From this perspective, both exact and approximate solutions for the bound-state energy of an electron in a square well are exposed. These results are used to improve the calculation of quantum size effects (QSEs) in ultrathin metallic films, obtained by several authors with simpler models of quantum wells. We show that, for a small (less than 5) number of monolayers, the differences between the predictions of these simpler models, and our approach, are important. Methods to improve the accuracy in the evaluation of various quantum size effects are shortly discussed. Using quantum mechanical-electromagnetic analogies, our results can be used in the study of light propagation in dielectric wave guides.

Keywords: ultrathin metallic films, quantum wells, finite square well, quantum size effects, heterojunctions

1. Introduction

If the dimension of a physical system is reduced, on one or several directions, up to the nanometric range, electron confinement generates states specific to quantum wells, quantum dots, or to other nanostructures, studied by new branches of science, nanophysics and nano-technology, extremely interesting from both applicative and fundamental perspectives. A fascinating aspect of nanophysics is that it can be sometimes understood using elementary, one-particle quantum mechanics; for instance, many phenomena specific to quantum wells can be treated using the simple model of a particle in a rectangular potential.

A class of physical systems which can be studied in the frame of this model is a particular kind of quantum wells—the ultrathin metallic films. In the last decades, they were object for

active investigation, mainly due to the quantum size effects (QSEs), like the oscillatory behavior of the film stability [1], of the lattice deformation [2], of the work function [3], etc., in dependence of the number of atomic monolayers. The QSEs, predicted in the pioneering papers of Sandomirskii [4] and Schulte [5], are important for both practical and theoretical reasons. The ultrathin metallic films have a special relevance for ferromagnetic materials, as they are responsible for the giant magnetoresistivity of the Fe/Cr antiferromagnetic lattice [6]. Also, the possibility of obtaining ultrathin metallic films, having a specific number of monolayers, allows the experimentalist to tune the work function, controlling the chemistry of the metallic surface [3]. All these effects can be satisfactorily explained with a quite simple physics, whose basic ingredient is the different quantization imposed to electrons moving on longitudinal and transversal directions. Namely, the electrons moving parallel to the surface of the metallic film are quantized by cyclic conditions; the result is that the wave vectors are quasi-continuous. The electrons moving perpendicular to the film are considered as confined in a rectangular well, so they are quantized according to the theory of quantum wells; the result is that the spectrum is discrete.

How simple can the model of the well be, in order to provide a quantitative understanding of the physics of ultrathin metallic films? In spite of its simplicity, even the model of the infinite rectangular well gives sometimes good results, for instance, for the calculation of lattice deformation [2] or of Fermi energy [7]. These successes can be explained by the fact that, if the number of monolayers is not very small, ($n \gtrsim 25$), the deep levels play a dominant role, and the difference between the corresponding levels (i.e., having the same quantum number) of the finite and of the infinite well is negligible. However, for a small number of monolayers ($n \lesssim 5$), this approximation does not work anymore. This is why it is important to obtain the exact value of the energy levels in the finite well or at least a precise approximation.

In this chapter, we shall present exact or approximate analytic results for the energy levels of a finite square well and show how they can improve the simple theoretical models which give a quantitative understanding of the behavior of ultrathin metallic films, especially the QSEs. Its structure is the following: in the second section, we shall discuss the quantum problem of the finite square well, mainly in order to put the eigenvalue equations in an appropriate form. The next one is a short review of the various attempts of solving these transcendental eigenvalue equations. The fourth section describes a simple algebraic approximation of the solution of the eigenvalue equations—the parabolic approximation—mentioning also similar but more precise approaches. In the next one, we put the eigenvalue equations in differential form and obtain the exact solution as a series expansion. The sixth section is devoted to the applications in the quantum statistical physics of the ultrathin metallic films of the analytic results obtained for the bound-state energy in a finite square well. By analyzing the predictions of the three models frequently used in the physics of ultrathin metallic films (infinite, semi-infinite, and finite square well) for the Fermi wave vector, we show the key role played by the finitude of the well, in the evaluation of QSEs. In the last section, we describe how our results can improve the current theory of this class of metallic films.

2. The bound states of a particle in a finite rectangular well

Until the mid-1980 of the previous century, the finite rectangular well was just an elementary problem of quantum mechanics, with applications in finding the energy levels of the quasi-free electrons on long molecules [8] or of the Ramsauer-Townsend effect [9]. The progress of solid-state physics, which finally led to the fabrication of quantum wells [10], quantum dots, or ultrathin metallic films [11, 12] and to the observation of QSEs associated with them, transformed these simple systems from problems of elementary quantum mechanics into theoretical models of devices of great practical interest.

We shall study now the movement of a particle in a finite rectangular well. There are, in principle, two ways of defining the potential of the well, choosing the origin of the energy $(E = 0)$ at the top or at the bottom of the well. In the first case, the advantage is that the energy of the bound states ("inside the well") is negative, as usual in quantum mechanics; in the second one, that is, in the limit of a very deep well, the energy level tends to the energy of the corresponding level of the infinite well. Even elementary, this distinction might be useful, in order to avoid confusions. We shall examine in detail the first case, so we shall consider a potential having the form (**Figure 1**):

$$V(x) = -U \cdot \theta\left(\frac{a}{2} - |x|\right) \tag{1}$$

where θ is the Heaviside function. The second case is shortly mentioned later on (Eqs. (24) and (25)). The Schroedinger equation for a particle of mass m moving in the potential (1) is

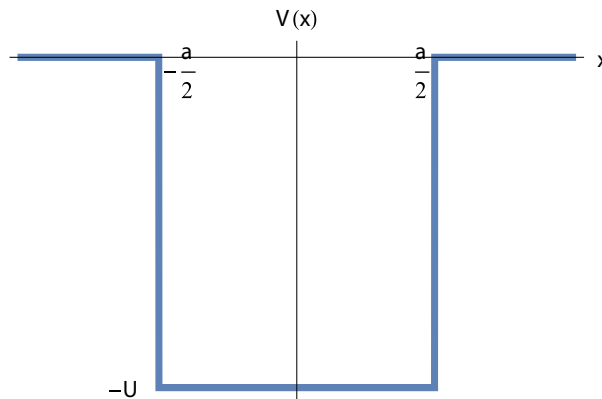$$\left[-\frac{\hbar^2}{2m}\frac{d^2}{dx^2} + V(x) - E\right]\psi(x) = 0 \tag{2}$$

Figure 1. The square well potential (Eq. (1)).

As the potential is invariant at spatial inversion, $V(x) = V(-x)$, the solutions have well-defined parity. Let us put

$$E = -\frac{\hbar^2 \varkappa^2}{2m}, \quad U = \frac{\hbar^2 k_0^2}{2m}; \quad k^2 = k_0^2 - \varkappa^2 \tag{3}$$

where the quantities $k, k_0, \varkappa$ have the dimension of wave vectors. With these notations, the Schroedinger equation for the particle inside the well takes the form:

$$\left(\frac{d^2}{dx^2} + k^2\right)\psi(x) = 0, \quad |x| < \frac{a}{2} \tag{4}$$

For the particle outside the well, it is

$$\left(\frac{d^2}{dx^2} - \varkappa^2\right)\psi(x) = 0, \quad |x| > \frac{a}{2} \tag{5}$$

The even solutions are

$$u_+(x) = A_+ \cos kx, \qquad\qquad 0 \leqslant x \leqslant a/2$$
$$u_+(x) = A_+ \cos ka \; e^{\varkappa(a-x)}, \qquad\quad x > a/2 \tag{6}$$
$$u_+(-x) = u_+(x)$$

and the odd ones are

$$u_-(x) = A_- \sin kx, \qquad\qquad 0 \leqslant x \leqslant a/2$$
$$u_-(x) = A_- \sin ka \; e^{\varkappa(a-x)}, \qquad\quad x > a/2 \tag{7}$$
$$u_-(-x) = u_-(x)$$

The continuity of the derivative in $x = a/2$ gives, for even states

$$\tan \frac{ka}{2} = \frac{\varkappa}{k} \tag{8}$$

and for odd states

$$\cot \frac{ka}{2} = -\frac{\varkappa}{k} \tag{9}$$

Defining the dimensionless parameter

$$P = k_0 a/2 = \sqrt{2mU}\,\frac{a}{2\hbar} = \frac{1}{p} \tag{10}$$

sometimes called potential strength, which actually characterizes both the particle (m) and the well (a, U), Eqs. (8) and (9) become

$$\tan \frac{ka}{2} = \frac{\sqrt{k_0^2 a^2 - k^2 a^2}}{ka} = \frac{\sqrt{P^2 - k^2 (a/2)^2}}{ka/2}, \quad even \ states \tag{11}$$

$$\cot \frac{ka}{2} = -\frac{\sqrt{k_0^2 a^2 - k^2 a^2}}{ka} = -\frac{\sqrt{P^2 - k^2 (a/2)^2}}{ka/2}, \quad odd \ states \tag{12}$$

Also, the energy is

$$E = -U \left[1 - \left(\frac{ka}{2P} \right)^2 \right] \ //13 \tag{13}$$

Using well-known trigonometric identities, Eqs. (11) and (12) take the form:

$$\frac{\cos \frac{ka}{2}}{\frac{ka}{2}} = \pm \frac{1}{P} \ (even \ states); \quad \frac{\sin \frac{ka}{2}}{\frac{ka}{2}} = \pm \frac{1}{P} \ (odd \ states) \tag{14}$$

The sign must be chosen in agreement with Eqs. (11) and (12), so to satisfy the conditions $\tan \frac{ka}{2} > 0$ for even states and < 0 for odd states, as we shall indicate explicitly in the forthcoming paragraphs.

In other words, to solve the eigenvalue, Eq. (14) means to find the functions $\zeta(p), \ \xi(p),$ satisfying the equations:

$$\frac{\sin \zeta(p)}{\zeta(p)} = \pm p, \quad \frac{\cos \xi(p)}{\xi(p)} = \pm p, \quad p = \frac{1}{P} \tag{15}$$

This is, of course, a difficult task. If we write Eq. (15) in a slightly different form

$$\frac{\sin x}{x} = y(x), \quad \frac{\cos x}{x} = y(x) \tag{16}$$

to solve Eq. (15) means to invert the function $y(x)$ defined by Eq. (16), i.e., to obtain the function $x(y)$. Clearly, x in Eq. (16)—and in the rest of the chapter—has nothing to do with the space coordinate x, as initially used in Eqs. (1)–(7).

The functions $\zeta(p), \xi(p)$ correspond to the intersections of the plots of the functions $\sin x/x$, $\cos x/x$ with the line $y = \pm p$, which satisfy the sign rule mentioned, after Eq. (14). The number of solutions depends on the value of p. If there is at least one solution $\xi(p)$ for any p, the solution $\zeta(p)$ exists only for $p < 1$. In **Figure 2**, the functions $\sin x/x$, $\cos x/x$ and the line $y = \pm p$, for $p = 0.1$, are plotted. The $x-$coordinate of the intersections corresponds to the functions $\zeta(p), \xi(p),$ as we shall explain later on.
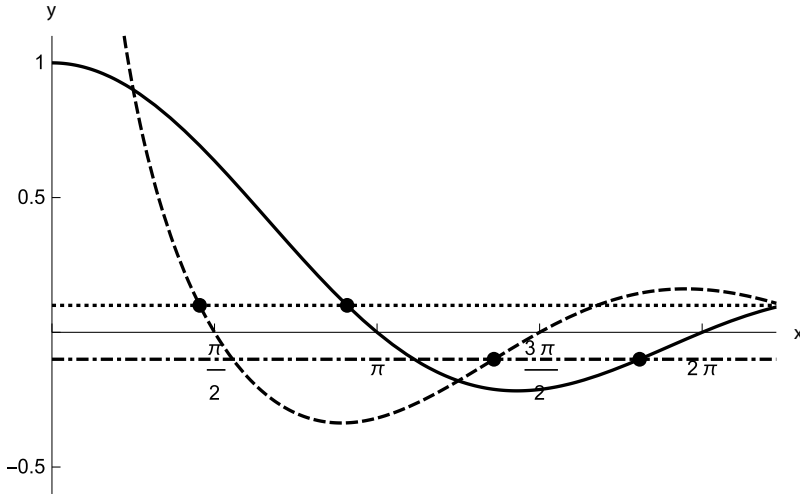
Figure 2. The $x-$ coordinate of the intersection points between the functions $\sin x/x$ (solid) and $\cos x/x$ (dashed) with the lines $y(x) = p$ (dots) and $y(x) = -p$ (dash-dots), marked with a point, corresponds to the functions $\zeta_1(p), \zeta_2(p)$, respectively, $\xi_1(p), \xi_2(p)$, for $p = 0.1$.

We shall write in a more explicit form Eq. (15), taking into account both the sign of the tan function (or of the cot function, which is, evidently, the same thing), as already mentioned, and the intervals of monotony of the functions $\sin x/x$, $\cos x/x$ [13]. The extremum points of the function $\cos x/x$ are given by the roots r_{cn} of the equation:

$$\tan x = -\frac{1}{x} \tag{17}$$

where r_{cn} is the root closest to $(n-1)\pi$. The eigenvalue equations for the even states are

$$x \in \left(0, \frac{\pi}{2}\right): \quad \frac{\cos x}{x} = p; \quad x \equiv \xi_1(p) \tag{18}$$

$$x \in \left(r_{c2}, \frac{3\pi}{2}\right): \quad \frac{\cos x}{x} = -p; \quad x \equiv \xi_2(p) \tag{19}$$

$$x \in \left(r_{c3}, \frac{5\pi}{2}\right): \quad \frac{\cos x}{x} = p; \quad x \equiv \xi_3(p) \tag{20}$$

and so on.

Similarly, the extremum points of the function $\sin x/x$ are the roots r_{sn} of the equation:

$$\tan x = x \tag{21}$$

where r_{sn} is the root closest to $\left(n - \frac{1}{2}\right)\pi$. The eigenvalue equations for the odd states are

$$x \in (r_{s,2}, 2\pi): \quad \frac{\sin x}{x} = -p; \quad x \equiv \zeta_2(p) \tag{22}$$

$$x \in (r_{s,3}, 3\pi): \quad \frac{\sin x}{x} = p; \quad x \equiv \zeta_3(p) \tag{23}$$

and so on. Each of Eqs. (18)–(20) and (22)–(23) has a unique solution, $\xi_1(p)$, $\xi_2(p)$, $\xi_3(p)$, respectively, $\zeta_2(p)$, $\zeta_3(p)$. On the aforementioned intervals, the functions $\cos x/x$, $\sin x/x$ are monotonic and have an inverse. The inverse functions are $\xi_1(p)$, $\xi_2(p)$, $\xi_3(p)$, respectively, $\zeta_2(p)$, $\zeta_3(p)$. The function $\zeta_1(p)$ satisfies the equation:

$$x \in (0, \pi): \quad \frac{\sin x}{x} = p; \quad x \equiv \zeta_1(p) \tag{24}$$

According to Eq. (13), the energy eigenvalues are

$$E_n = -U + U\left(\frac{k_n a}{2P}\right)^2 \tag{25}$$

If the particle moves not in potential $V(x)$ given by (1), but in a potential

$$V^{(1)}(x) = V(x) + U \tag{26}$$

then the energy levels will be given by

$$E_n^{(1)} = U\left(\frac{k_n a}{2P}\right)^2 \tag{27}$$

According to the parity of n, $k_n a/2$ corresponds to the functions ξ and ζ, for instance, $k_1 a/2 = \xi_1(p), k_2 a/2 = \zeta_1(p)$, etc.

As already mentioned, the advantage of using the potential (1) is that the energy of a particle "inside the well," so in a bound state, is negative, corresponding to the most usual convention of quantum mechanics. However, the form (26) of the potential has the advantage that its levels approach, in the limit of a very deep well, the levels of the infinite well. Indeed, for $n \to \infty$, so for very deep wells, the quantization condition for the wave vector becomes $k_n a \simeq n\pi$, so

$$k_n \simeq \frac{n\pi}{a} \tag{28}$$

and Eq. (27) gives the expression of the wave vector corresponding to the $n-$th state in an infinite well:

$$E_n^{(\infty)} = \frac{\pi^2 \hbar^2}{2ma^2} n^2 \tag{29}$$

3. Solving the eigenvalue equation of the finite well: a historical perspective

The eigenvalue equations for the wave vectors (18)–(20) and (22)–(24) are transcendental equations, and their solutions cannot be written as a finite combination of elementary functions. More than this, till now, they cannot be expressed neither in terms of the special functions of the mathematical physics. There are a large number of papers devoted to this subject, in the last 60 years.

The first one, due to Pitkanen [14], writes the eigenvalue Eqs. (8) and (9) in the simpler form (18)–(20) and (22)–(24), providing an interesting visualization of the solutions. The second one, due to Cantrell [15] (who does not cite [14], producing a delay in the circulation of this paper), also proposes the replacement of Eqs. (8) and (9) with (18)–(20) and (22)–(24)—in fact, a repetition of Pitkanen's contribution—and notices that the eigenvalue equation for odd states is also the eigenvalue equation for a particle moving in a semi-infinite well, i.e., in a potential given by

$$U(x < 0) = \infty, \quad U(0 < x < a) = -U_0, \quad U(x > a) = 0 \tag{30}$$

Graphical solutions are proposed by Guest [16], who made visible the similarities between the bound-state energies in a finite well and the modes of a metallic wave guide ([17]; fig. (8.14)); actually, both the electrodynamic and quantum mechanical problems are equivalent forms of the same Sturm-Liouville problem [18]. Aronstein and Stroud [19] wrote the eigenvalue equation as

$$\frac{ka}{2} + \arcsin\frac{ka/2}{P} = \frac{n\pi}{2} \tag{31}$$

This elegant form had been already given in the first edition of Landau's textbook of quantum mechanics, in the late 1940s of the twentieth century (for the English version of a more recent edition, see [20]) but remained unknown to Western physicists—a minor but significant consequence of the poor circulation of scientific information during the Cold War.

A completely different approach was proposed by Siewert [21], who obtained an exact solution in an integral form; unfortunately, it is very complicated and of limited practical use. Recently, Siewert's solutions were discussed in the context of generalized Lambert functions [22], a subject under intense investigation.

Among the papers which provide approximate analytical solutions of the eigenvalue Eqs. (18)–(20) and (22)–(24), the most popular one, authored by Barker et al. [23], is essentially a low-order algebraic approximation of $\sin x, \cos x$. Another interesting contribution is that of Garrett [24], who introduced an intuitive physical concept, the characteristic depth δ of a finite well, for a bound electron with energy E:

$$\delta = \frac{\hbar}{\left(2m(V_0 - E)\right)^{1/2}} \quad /32 \tag{32}$$

as the magnitude of the domain outside the well, where the wave function can penetrate significantly, decreasing however exponentially. This concept is similar to the concept of skin depth in electromagnetism [17] or to the concept of viscous penetration depth in fluids [25], § 24.

In the context of various approximations, it is worth to mention the "algebraization" of trigonometric functions, proposed by de Alcantara Bonfim and Griffiths [26], which transforms the transcendental equations for the eigenvalues of the finite well in approximate, tractable, algebraic equations. For instance, we can use the approximations:

$$\tan x \simeq \frac{0.45x}{1 - \frac{2x}{\pi}}; \quad \cos x \simeq \frac{1 - (2x/\pi)^2}{(1 + cx^2)^s}, \quad 0 \leqslant x \leqslant \frac{\pi}{2} \tag{33}$$

where the pair of constants can be chosen as

$$s = 1/2, \quad c = 0.212 \text{ or } s = 1, \quad c = 0.101 \tag{34}$$

4. The parabolic approximation

To solve the eigenvalue equations, or—more generally—Eq. (16), with $y \gtrless 0$, means, as already mentioned, to obtain the inverse of the function $y(x)$ defined by (16), i.e., to obtain the function $x(y)$. Geometrically, the inverse of the function $y(x)$, plotted as a curve whose generic point is (x, y), is its symmetric with respect of the first bisectrix. A generic point of the inverse function has the coordinates (y, x).

Clearly, only the monotonic functions can be inverted; for instance, in our case, the function $\sin x/x$ must be replaced with its restriction on their intervals of monotony, and this restriction will be actually inverted. We shall consider $r_{sn} \simeq \left(n - \frac{1}{2}\right)\pi$ and approximate the bump of the function $\sin x/x$ on the interval $(2n\pi, (2n+1)\pi)$ with a segment of parabola. It is easy to see that the ascendant part of this parabola is given by the equation:

$$y = \frac{4}{\left(2n + \frac{1}{2}\right)\pi^3}\left\{\frac{\pi^2}{4} - \left[x - \left(2n + \frac{1}{2}\right)\pi\right]^2\right\}, \tag{35}$$

$$2n\pi < x < \left(2n + \frac{1}{2}\right)\pi$$

Solving this equation for y

$$x = \left(2n + \frac{1}{2}\right)\pi - \sqrt{\frac{\pi^2}{4} - \frac{y}{4}\left(2n + \frac{1}{2}\right)\pi^3} \tag{36}$$

and making the change $x \leftrightarrow y$, we get for the root ζ_{2n} [27]:

$$\zeta_{2n}^{(par)}(x) = \left(2n + \frac{1}{2}\right)\pi - \sqrt{\frac{\pi^2}{4} - \frac{x}{4}\left(2n + \frac{1}{2}\right)\pi^3}, \tag{37}$$

$$0 < x < \frac{1}{\left(2n + \frac{1}{2}\right)\pi}$$

Following exactly the same steps, similar expressions can be obtained for $\zeta_{2n}(x < 0)$ and for all the functions ζ_q, ξ_q their parabolic approximations can be obtained. A special case is ζ_1 :

$$\zeta_{2n}^{(par)}(x) = \pi\sqrt{1 - x} \tag{38}$$

The method cannot be applied, evidently, for ξ_1, as the function to be inverted has no bump.

The explicit expressions of the parabolic approximation for the functions ξ_n $(n > 1)$ and ζ_n, obtained in [27] are simple, but cumbersome, and will not be given here.

It is possible to improve the parabolic approximation in two ways:

(1) To express the numerical coefficients in formulas similar to Eq. (36) using analytic approximations for the roots of the equations $\tan x = x$ and $\tan x = -1/x$. Actually, these transcendental equations can be transformed in approximate, tractable, algebraic equations, using the algebraic approximations of the tan function, proposed by de Alcantara Bonfim and Griffiths [26] and generalized by other authors [28]. This approach is sometimes called "improved parabolic approximation."

(2) To approximate the bumps of the functions $\sin x/x$ and $\cos x/x$ with a cubic curve (polynomial); this approach is sometimes called cubic approximation. The calculations are elementary, but cumbersome, and will not be given here [29].

For an algebraic approximation of ζ_1, we can use a formula similar to the cos approximation in Eq. (34), namely,

$$\frac{\sin x}{x} \simeq \frac{1 - \left(\frac{x}{\pi}\right)^2}{\sqrt{1 + 0.2x^2}} \tag{39}$$

proposed in [30].

The finite square well is a good starting point for similar quantum mechanical problems, i.e., the asymmetric well (when the walls of the well, see **Figure 1**, have different heights), the

semi-infinite well (when one of the walls is infinite), or more realistic cases, when the walls are rounded (see [11, 12]). These potentials can model a semiconductor heterojunction (a thin semiconductor slice sandwiched between two different, larger semiconductors), a metallic film deposited on a semiconductor (in vacuum), and so on.

5. The differential form of transcendental equations

We shall indicate now an approach for solving the eigenvalue Eqs. (18)–(20) and (22)–(24) providing an exact solution, written as a series expansion. We shall first illustrate this method with the function $\zeta_1(p)$.

Taking the derivative with respect to p in both sides of the equation

$$p\zeta_1(p) = \sin\zeta_1(p) \tag{40}$$

we get

$$\frac{d\zeta_1(p)}{dp} = \frac{\zeta_1(p)}{\cos\zeta_1(p) - p} \tag{41}$$

Using Eq. (40) and taking into account that we are in the second quadrant

$$\cos\zeta_1(p) = -\sqrt{1 - p^2\zeta_1(p)^2} \tag{42}$$

we obtain the differential form of the equation for $\zeta_1(p)$:

$$\frac{d\zeta_1(p)}{dp} = -\frac{\zeta_1(p)}{\sqrt{1 - p^2\zeta_1(p)^2} + p}, \quad p \in [0, 1], \quad \zeta_1(p) \in \left(\frac{\pi}{2}, \pi\right) \tag{43}$$

with the initial condition:

$$\zeta_1(0) = \pi \tag{44}$$

Putting

$$X_{2n}(p) = \zeta_n(p), \, X_{2n-1}(p) = \xi_n(p), \quad n = 1, 2, \ldots, \tag{45}$$

replacing p by x and relaxing the restriction $p > 0$, the equations for the eigenvalues of the wave vectors can be written in a unitary form:

$$\frac{dX_n(x)}{dx} = -\frac{X_n(x)}{\sqrt{1 - x^2X_n(x)^2} + x} \tag{46}$$

with the initial condition:

$$X_n(0) = \frac{n\pi}{2} \tag{47}$$

With Eq. (46), we can obtain the derivatives of any order of $X_n(x)$ in an arbitrary point x_0 and, consequently, write down the Taylor series for this function, with arbitrary accuracy. Choosing $x_0 = 0$, we get the following series expansion for $X_n(x)$:

$$X_n(x) = \sum_{m=0}^{\infty} q_m\left(\frac{n\pi}{2}\right)x^m \tag{48}$$

The parameters q_m are polynomials in the variable

$$\frac{n\pi}{2} \equiv b : \tag{49}$$

$$q_0(b) = b, \quad q_1(b) = -b, \quad q_2(b) = b \tag{50}$$

$$q_3(b) = -b\left(1 + \frac{b^2}{6}\right), \quad q_4(b) = b\left(1 + \frac{2b^2}{3}\right) \tag{51}$$

$$q_5(b) = -b\left(1 + \frac{5}{3}b^2 + \frac{3}{2^3 \cdot 5}b^4\right), \quad q_6(b) = b\left(1 + \frac{2 \cdot 5}{3}b^2 + \frac{2^3}{3 \cdot 5}b^4\right) \tag{52}$$

and so on. For the explicit expression of $q_m(b)$, $m < 17$, see [13]. The first three terms correspond to the Barker approximation.

Let us also remark that, in spite of the fact that the equivalence of Sturm-Liouville problems for electromagnetic fields and for wave functions was noticed many years ago, the results obtained for the finite rectangular well remain unused by the researchers studying wave propagation in wave guides or in other simple geometries. Reciprocally, the very detailed solutions of the equations for the normal modes of electromagnetic waves (see, for instance, the references [90, 92] in [31]) were apparently overlooked by researchers working in quantum mechanics.

6. Applications to the statistical physics of ultrathin metallic films

With few exceptions, the physics of ultrathin metallic films can be satisfactorily explained using different types of infinite well for the potential of electrons moving normally to the film plane. The model of the infinite well can be improved, for instance, by the phase accumulation theory [11, 12, 32], quite popular among the scientist working in surface physics. The theory

satisfactorily explains the quantum scale effects (QSEs) appearing in such systems and predicted theoretically in the pioneering papers of Sandomirskii [4] and Schulte [5].

If, for thin films, such theoretical models can be successfully applied, for ultrathin films, with only few (typically, less than 5) monolayers, obtained experimentally in the last two decades, the approximation of the infinite well is inadequate. This is why in such cases we have to use the exact solutions for the bound-state energy of the finite well or, at least, their analytic approximations. In order to make clear the differences between the predictions of the two models—the first one is based on the infinite well, and the second one is based on the finite well—we shall evaluate some QSE for an ultrathin metallic film for three potentials: infinite, semi-infinite, and finite wells.

6.1. The infinite well model for the quantum well in an ultrathin metallic film

Let us consider a rectangular metallic films, with edges L_x, L_y, L_z, where L_x, L_y are macroscopic or mesoscopic and L_z is nanoscopic. If the metallic film is placed between two semi-infinite dielectrics, we can presume that the conduction electrons move freely in the plane of the film (defined by the axes Ox, Oy), and in transversal direction (Oz), the potential can be approximated by an infinite rectangular well. The film has the volume:

$$V = L_x L_y L_z \tag{53}$$

and the electron energy is

$$\frac{\hbar^2 \vec{k}^2}{2m} \tag{54}$$

where we put

$$\vec{k} = (k_x, k_y, k_z) = \left(\frac{2\pi}{L_x} n_x, \ \frac{2\pi}{L_y} n_y, \ \frac{\pi}{L_z} n_z \right) \tag{55}$$

$$n_x, \ n_y = \pm 1, \ \pm 2, \ \ldots; \ n_z = 1, \ 2, \ \ldots \tag{56}$$

The differences between the values taken by the integers n_x, n_y and n_z are due to the fact that, along the directions Ox and Oy, the quantization is obtained imposing cyclic conditions, and along the direction Oz by "rigid wall" conditions, specific to the infinite well, with impenetrable walls.

For ultrathin films, the discrete spectrum of k_z can be easily observed experimentally, and the conduction electrons constitute a quasi-2D multiband electron gas, characterized by a quasi-continuum, 2D wave vector $\vec{k}_{2D} = (k_x, k_y)$ and by a quantized wave vector $k_z = n_z \frac{\pi}{L_z}$.

The number $n_z = q$ plays the role of an subband index. So, in the 3D reciprocal space, the spectrum is formed by planes of allowed states (subbands), parallel to the xOy plane, and separated along the z direction, by segments of length $\Delta k_z = \pi/L_z$.

Let us consider a numeric example. For a metallic film with two atomic monolayers, the typical values are $L_z \sim 0.6\ nm$, so $\Delta k_z \sim 5\ nm^{-1}$ and $k_F = 16\ nm^{-1}$. Therefore, only three plans cut the Fermi (hemi-)sphere, or—in other words—only the first subbands are occupied, corresponding to $p = 1, 2, 3$. Let us mention that there is no band corresponding to $p = 0$, as, in this case, the amplitude of the wave function would be zero.

We shall compute the number of occupied electronic states and the Fermi wave vector of the ultrathin film. The total number of subbands, which cut the Fermi sphere is Q, defined by

$$Q = \mathrm{int}\left[\frac{k_F}{\Delta k_z}\right] \tag{57}$$

where $\mathrm{int}[x]$ is the largest integer smaller than x. In our particular case, discussed in the previous example, $Q = 3$, so there are only three distinct subbands, occupied at $T = 0$. For films with few monolayers, the subbands are separated by energies of about $1\ eV$, so we can consider that $T = 0$.

As the occupied states belonging to the subband of index q are situated inside circles cut by the Fermi sphere, of radius $k_{F,q} = \left[k_F^2 - (q\Delta k_z)^2\right]^{1/2}$ (these circles are the intersection of the subband plane with the Fermi sphere), and the area corresponding to one electronic state k in each subband is $(2\pi)^2/L_xL_y = (2\pi)^2 L_z/V$, there are

$$\frac{\pi k_{F,q}^2}{(2\pi)^2 L_z/V} = \frac{V}{(2\pi)^2 L_z}\pi k_{F,q}^2 \tag{58}$$

occupied states in the subband q. The number of electrons N inside the Fermi sphere is obtained by summing up over the occupied subbands:

$$N = 2\frac{V}{(2\pi)^2 L_z}\pi \sum_{q=1}^{Q} k_{F,q}^2 \tag{59}$$

$$= \frac{V}{2\pi L_z}\left[Q k_F^2 - \left(\frac{\pi}{L_z}\right)^2 \sum_{q=1}^{Q} q^2\right]$$

where the factor of 2 is due to the electron spin. Putting

$$\Sigma_1(Q) = \sum_{q=1}^{Q} q^2 = \frac{1}{6}Q(Q+1)(2Q+1) \tag{60}$$

and introducing the number density of electrons $n = N/V$, we get

$$\left[k_F^2 \right]_Q = n \frac{2\pi L_z}{Q} + \left(\frac{\pi}{L_z} \right)^2 \frac{\Sigma_1(Q)}{Q} \tag{61}$$

giving the dependence of the Fermi wave vector on the thickness L_z, on the number of subbands Q, and on the electron number density n.

Introducing Eq. (61) in Eq. (57), we get

$$\left[\frac{\pi}{12} Q(4Q+1)(Q-1) \right]^{1/3} \frac{1}{n^{1/3}} \leqslant L_z < \left[\frac{\pi}{12} Q(4Q+5)(Q+1) \right]^{1/3} \frac{1}{n^{1/3}} \tag{62}$$

The last two equations define the QSEs on the Fermi wave vector; they can be considered as the starting point of all other similar QSEs of various physical quantities characterizing the ultrathin film.

Choosing $n = 4 \cdot 10^{22} cm^{-3} = 40\ nm^{-3}$, we get the expression of the Fermi wave vector for an electronic gas 1, 2, 3, or 4 subbands:

$$\left[k_F^2 \right]_1 = 80\pi L_z + \left(\frac{\pi}{L_z} \right)^2, \quad L_z < 0.5\ nm \tag{63}$$

$$\left[k_F^2 \right]_2 = 40\pi L_z + \frac{5}{2} \left(\frac{\pi}{L_z} \right)^2, \quad 0.5\ nm \leqslant L_z < 0.8\ nm \tag{64}$$

$$\left[k_F^2 \right]_3 = \frac{80\pi}{3} L_z + \frac{14}{3} \left(\frac{\pi}{L_z} \right)^2, \quad 0.8\ nm \leqslant L_z < 1.1024\ nm \tag{65}$$

$$\left[k_F^2 \right]_4 = 20\pi L_z + 7.5 \cdot \left(\frac{\pi}{L_z} \right)^2, \quad 1.1024\ nm \leqslant L_z < 1.4006\ nm \tag{66}$$

where k_F is measured in nm^{-1}. The expressions (63)–(66) clearly illustrate the QSE on the Fermi wave vector.

6.2. The semi-infinite well model for the quantum well in an ultrathin metallic film

As already mentioned (see Eq. (45) and the remark just below Eq. (27)), the relation between the solutions of the eigenvalue Eq. (46), namely, the functions X, and the wave vector k is

$$k \to \frac{2}{L} X \tag{67}$$

and the bound states of the semi-infinite well are described by the odd states of a finite well with the same length. In other words

$$k_{2n} \to \frac{2}{L_z} \zeta_n(p) \tag{68}$$

It is convenient to define

$$w = \left(\frac{mU}{2\hbar^2}\right)^{1/2} \tag{69}$$

So, the inverse strength of the quantum well, similar to Eq. (10), can be defined as

$$p = \frac{1}{wL_z} \tag{70}$$

According to Eq. (68), the wave vector depends on both L_z and U (or w). As U is a material dependent quantity, related, in principle, to the work function, we shall replace it, for this numerical example, with the typical value of $U = 5 \; eV$; in this case, Eq. (70) gives

$$p = \frac{1}{6.5 \times \overline{L_z}} \tag{71}$$

with $\overline{L_z}$ in nanometers.

An important difference which occurs at semi-infinite wells, compared to the infinite wells, is that it keeps a finite number of bound states. Consequently, the energy spectrum of the electron gas of the metallic film contains a finite number of subbands, in dependence of the value of p. The well keeps at least one state if

$$p < 1 \quad \Rightarrow \overline{L_z} > \frac{1}{6.3} = 0.16 \; nm \tag{72}$$

and exactly one state ζ_1 if

$$\frac{2}{3\pi} = 0.21221 < p < 1, \quad or \; 0.16 \; nm < \overline{L_z} < 0.74794 \; nm \tag{73}$$

This corresponds, usually, to a film with one or two monolayers. We have two states in the well, ζ_1 and ζ_2, if

$$\frac{2}{5\pi} = 0.12732 < p < 1, \quad or \; 0.16 \; nm < \overline{L_z} < 1.2467 \; nm \tag{74}$$

This corresponds, usually, to a film with up to four monolayers, etc. These conditions are purely mathematical, i.e., consequences of the specific form of the eigenvalue equations.

Now, we shall impose physical conditions, due to the $p-$ or $\overline{L_z}-$ dependence of the Fermi wave vector and of the number of subbands. Taking into account Eq. (67) and using an argument similar to Eq. (57), we find

$$k_F^2 = \frac{2\pi L_z}{Q} n + \frac{1}{Q} \left(\frac{2}{L_z}\right)^2 \sum_{q=1}^{Q} \left(\zeta_q(p)\right)^2 \tag{75}$$

Let us presume that the electron gas contains exactly Q subbands, which is equivalent to the relation:

$$\frac{2}{(Q-1/2)\pi} < p = \frac{1}{6.5 \times \overline{L_z}} < 1, \quad or \ \ 0.16 \ nm < \overline{L_z} < 1.2467 \ nm \tag{76}$$

or

$$\frac{1}{6.5} < \overline{L_z} < \frac{(Q-1/2)\pi}{13} \tag{77}$$

Therefore, instead of Eq. (62), we have

$$\left(\frac{2}{L_z}\right)^2 \zeta_Q^2(p) \leqslant k_F^2 = \frac{2\pi L_z}{Q} n + \frac{1}{Q} \left(\frac{2}{L_z}\right)^2 \sum_{q=1}^{Q} \left(\zeta_q(p)\right)^2 \ //78 \tag{78}$$

The term corresponding to the r.h.s. of the inequality (62) is missing in this case, as the number of roots (solutions) is completely determined by the condition imposed to L_z, according to Eq. (77).

Replacing the electron number density with a typical value $n = 40 \ nm^{-3}$ and using Eq. (63), we get (we took advantage of the fact that, incidentally, the numeric factor is $0.25128 \simeq 1/4$)

$$\zeta_Q^2(p) \leqslant \frac{1}{4Qp^3} + \frac{1}{Q} \sum_{q=1}^{Q} \left(\zeta_q(p)\right)^2 \tag{79}$$

This restriction on p, which can be verified using, for instance, the cubic approximation for ζ_n, must be considered together with Eqs. (71)–(73).

6.2.1. The finite well model for the quantum well in an ultrathin metallic film

The situation is quite similar to the previous one—the semi-infinite well. However, in this case, there is at least a solution for each value of p. Eqs. (71)–(73) are replaced by

$$p > 1 \ \ or \ \ \overline{L_z} < \frac{1}{6.3} = 0.16 \ nm, \tag{80}$$

$$one \ state, \ \ X_1 = \xi_1;$$

$$\frac{1}{\pi} = 0.31831 < p, \quad or \ \ \overline{L_z} < 0.31831 \ nm, \tag{81}$$

$$\text{two states,} \quad X_1 = \xi_1, \quad X_2 = \zeta_1$$

$$\frac{2}{3\pi} = 0.21221 < p < 1, \quad or \ \overline{L_z} < 0.74794 \ nm, \tag{82}$$

$$\text{three states,} \quad X_1 = \xi_1, \quad X_2 = \zeta_1, \quad X_3 = \xi_2$$

and so on. In Eqs. (76) and (77), the replacement $\zeta_q \to X_q$ must be done. Eq. (74), with $\zeta_q \to X_q$, gives the QSE for the Fermi wave vector.

These solutions, or their analytic approximations (for instance, the cubic one), can be used directly in the models already proposed for the infinite well [33], in order to obtain the electron density, the surface free energy, the surface dipolar moment, or other similar quantities, in the more realistic case of a finite rectangular well.

7. Conclusions

This chapter illustrates how solutions of a simple quantum mechanical problem can be used for the description of certain interesting phenomena of nanophysics. Specifically, we referred to the exact solutions of the eigenvalue equations for the eigenenergy of the bound states of a particle in a rectangular well. If the physical problem is elementary, and the wave functions are simply written in terms of elementary functions, the equations for the eigenvalues of energy (or of the wave vector) are transcendental—and highly nontrivial. We obtain both exact solutions (series expansions) of these transcendental equations and approximate ones—with various degrees of complexity and accuracy. The value of the Fermi wave vector of the electrons in the metallic film, calculated for the finite well model, differs drastically from those calculated with the infinite well one.

Our results for the one-electron wave functions of the finite barrier model can be used as Kohn-Sham state in the self-consistent calculations of surface energy [34], for more accurate calculations of the stability of the films [1] and of other QSEs [33]. They can be also used as zero-order approximations for more realistic potentials, e.g., with rounded walls or undulate bottom—in a Rayleigh-Schroedinger or Dalgarno-Lewis perturbation theory [35].

Using the analogy between the movement of electrons in time-independent potentials and propagation of electromagnetic waves in dielectrics or metallic wave guides [18], mathematically, they are identical Sturm-Liouville problems; our results can be extended to several problems of electromagnetism and optics. This analogy can be easily developed for planar dielectric waveguides, namely, for "step-index" dielectrics, consisting of a slab of higher refractive index (core), sandwiched between two half spaces of lower refractive index (cladding). In such a situation, the quantum counterpart of the dielectric guide is a square well. This issue is discussed in detail by Casey and Panish in the context of heterostructure lasers [36]. It is easy to notice that the eigenvalue equations for transverse electric and magnetic modes, (2.4–45, 54, 60, 66) in [36], are essentially identical with our Eqs. (8) and (9).

Acknowledgements

Author details

Victor Barsan

Address all correspondence to: vbarsan@theory.nipne.ro

IFIN and the UNESCO Chair at HHF, Bucharest-Magurele, Romania

References

[1] Wu B, Zhang Z. Stability of metallic thin films studied with a free electron model. Physical Review B. 2008;**77**:035410 (12pp) DOI: 10.1103/PhysRevB.77.035410

[2] Czosche P, Hong H, Basile L, Chiang T-C. Quantum oscillations in the layer structure of thin metal films. Physical Review Letters. 2003;**91**:226801 (4pp). DOI: 10.1103/PhysRev Lett.91.226801

[3] Kim J, Qin S, Yao W, Niu Q, Chou M-Y, Shih C-K. Quantum size effects on the work function of metallic thin film nanostructures. Proceedings of National Academy of Sciences. 2010;**107**:12761-12765. DOI: 10.1073/pnas.0915171107

[4] Sandomirskii VB. Quantum size effects in a semimetal film. Soviet Physics JETP. 1967;**25**:101-106

[5] Schulte FK. A theory of thin metal films: electron density, potentials and work function. Surface Science. 1976;**55**:427-444. DOI: 10.1016/0039-6028(76)90250-8

[6] Qiu ZQ, Smith NV. Quantum well states and oscillatory magnetic interlayer coupling. Journal of Physical: Condensed Matter. 2002;**14**:R169-R193. PII: 0953-8984/02/080169+25 $30.00

[7] Atkinson WA, Slavin AJ. A free-electron calculation for quantum size effects in the properties of metallic islands on surfaces. American Journal of Physics. 2008;**76**:1099-1101. DOI: 10.1119/1.2976792

[8] Harrison WA. Applied quantum mechanics. Singapore: World Scientific; 2000. 353 p

[9] Van Wyk S. Computer Solutions in Physics. World Scientific; 2011. 292 p

[10] Kolbas RM, Holonyak N Jr. Manmade quantum wells: A new perspective on .the finite square well problem. American Journal of Physics. 1984;**52**:431-437. DOI: 10.1119/1.13649

[11] Milun M, Pervan P, Woodruff DP: Quantum well structures in thin metal films: Simple model physics in realty? Reports in Progress Physics. 2002;**65**:99-141. PII: S-0034-4885(02) 12597-8

[12] Pervan P, Milun M. Quantum well states in metallic films, wires, and dots. In: Wandelt K, editor. Surface and Interface Science: Solid-Solid Interfaces and Thin Films. 1st ed. New Jersey: Wiley-VCH Verlag; 2014. pp. 493-543

[13] Barsan V. Square wells, quantum wells and ultra-thin metallic films. Philosophical Magazine. 2014;**94**:190-207. DOI: DOI10.1080/14786435.2013.845313

[14] Pitkanen PH. Rectangular potential well in qeuantum mechanics. American Journal of Physics. 1955;**23**:111-113

[15] Cantrell CD. Bound-state energies of a particle in a finite square well: An improved graphical solution. American Journal of Physics. 1971;**39**:107-110

[16] Guest PG. Graphical solutions for the square well. American Journal of Physics. 1972;**40**: 1175-1176. DOI: https://doi.org/AJPIAS0002-9505

[17] Jackson JD. Classical Electrodynamics. 3rd ed. New Jersey: John Wiley & Sons; 1999. 808 p

[18] Barsan V. Waveguides, resonant cavities, optical fibers and their quantum counterparts. In: Barsan V, Lungu RP, editors. Trends in Electromagnetism. 1st ed. InTech; 2011. pp. 89-112

[19] Aronstein DL, Stroud CR. General series solution for finite square-well energy levels for use in wave-packet studies. American Journal of Physics. 2000;**68**:943-947. DOI: https:// doi.org/AJPIAS0002-9505

[20] Landau LD, Lifshitz EM. Quantum Mechanics: Non-Relativistic Theory. 3rd ed. Amsterdam: Pergamon Press; 1977. 680 p

[21] Siewert CE. Explicit results for the quantum-mechanical energy states basic to a finite square-well potential. Journal of Mathematical Physics. 1978;**19**:434-435. DOI: https://doi. org/JMAPAQ19

[22] Barsan V: Siewert solutions of transcendental equations, generalized Lambert functions and physical applications. arXiv:1703.10052v1;2017

[23] Barker B I, Rayborn G H, Ioup J W, Ioup G E. Approximating the finite square well in an infinite well: Energies and eigenfunctions. American Journal of Physics. 1991;**59**:1038-1042. DOI: https://doi.org/AJPIAS59

[24] Garrett S. Bound state energies of a particle in a finite square well: A simple approximation. American Journal of Physics. 1979;**47**:195-196. doi.org/10.1119/1.11875.47

[25] Landau LD, Lifshitz EM. Fluid Mechanics. 2nd ed. Pergamon, 1987. 535p

[26] de Alcantara Bonfim OF, Griffiths DJ. Exact and approximate energy spectrum for the finite square well and related potentials. American Journal of Physics. 2006;**74**:43-49 https://doi.org/10.1119/1.2140771

[27] Barsan V, Dragomir R. A new approximation for the quantum square well. Optoelectronics and Advanced Materials Rapid Communication. 2012;**6**:917-925

[28] Barsan V: Algebraic approximations for transcendental equations with applications in nanophysics.Philosophical Magazine. 2015;**95**:3023-3038. DOI: http://dx.doi.org/10.1080/14786435.2015.1081425

[29] Barsan V. A new analytic approximation for the energy eigenvalues of a finite square well. Romanian Report in Physics. 2012;**64**:685-694

[30] Barsan V, Ciornei M-C. Semiconductor quantum wells with BenDaniel–Duke boundary conditions: Approximate analytical results. European Journal of Physics. 2017;**38**:015407 (22pp). DOI: 10.1088/0143-0807/38/1/015407

[31] Marcuse D. Light Transmission Optics. 2nd ed. New York: Van Nostrand; 1982. 541p

[32] Jalochowski M. Experimental evidence for quantum size effects in ultrathin metallic films. Progress in Surface Science. 1995;**48**:287-297. DOI: https://doi.org/PSSFBP48

[33] Han Y, Liu D-J. Quantum size effects in metal nanofilms. Physical Review. 2009;**B80**: 155404 (17pp). DOI: 10.1103/PhysRevB.80.155404

[34] Pitarke JM, Eguilez AG. Jellium surface energy beyond the local-density approximation. Physical Review. 2012;**B63**:045116 (11pp). DOI: 10.1103/PhysRevB.80.045116

[35] Mavromatis HA. Exercises in Quantum Mechanics. 2nd ed. Dordrecht: Kluwer; 1992. 339p. ISBN 0-7923-1557-X

[36] Casey HC Jr, Panish MB. Heterostructure Lasers. 1st ed. Amsterdam: Academic Press; 1978. 272 p. ISBN 012163101X, 9780121631017

Photoionization Cross Section in Low-Dimensional Systems

Moletlanyi Tshipa and Monkami Masale

Additional information is available at the end of the chapter

Abstract

A theoretical investigation of the effects of the parabolic, shifted parabolic, hill-like, and cup-like parabolic confining electric potentials on photoionization cross section (PCS) in a spherical quantum dot is presented. Each of the parabolic potentials is superimposed on an infinite spherical square quantum well (ISSQW) potential. The parabolic potential blueshifts the peaks of the PCS, while the shifted parabolic potential causes a redshift. As the so-called strength of cup-like parabolic potential is increased, the peak of the PCS becomes redshifted for the $s \rightarrow p$ transition, but blueshifted for the $p \rightarrow d$, $d \rightarrow f$ (and so forth) transitions. On the contrary, an increase in the strength of the hill-like parabolic potential blueshifts peaks of the PCS for $s \rightarrow p$ transitions, while it redshifts those of transitions between higher states.

Keywords: photoionization cross section, confining electric potential, spherical quantum dot, hydrogenic impurity

1. Introduction

Recent advances in nanofabrication technology have made it possible to fabricate nanostructures of different sizes and geometries [1–3]. Nanostructures have a wide range of applications including in nanomedicine [4, 5], optoelectronics [6, 7], energy physics [8–12], and gas sensing [13]. Now, even with utmost care and employing the most advanced techniques, it is not possible to fabricate nanostructures which are free of impurities. It may be advantageous, however, to introduce impurities into a nanostructure at the fabrication stage. The presence of such deliberately introduced impurities can lead to improved performance of nanodevices, for example, enhancement of electrical conductivity of semiconducting materials [14]. The impurity may actually be positively charged, in which case an electron may become

bound to it, thus forming an electron-hole pair. Photoionization is one of the useful probes for the particular nature of electron-impurity interactions in low-dimensional systems. In the process of photoionization, upon absorbing sufficiently enough energy from the irradiating electromagnetic field, the electron can break free from the impurity. In a sense, photoionization is the classical analog of the binding energy problem. Certainly, the subtlety in photoionization effects is in the variety of conditions in low-dimensional systems. These conditions include quantization of the electron's energy levels as well as the optical properties of the specimen.

In this regard, photoionization studies on nanostructures could offer insight into the electron-impurity interaction in a wide variety of conditions. These photoionization effects have fueled significant interest in the processes of photoionization in low-dimensional systems. The effects of geometry and hydrostatic pressure on photoionization cross section (PCS) have been reported in concentric double quantum rings [15]. The effect of applied electric field on photoionization cross section has also been probed in cone-like quantum dots [16]. The role that impurity position plays in modifying the PCS in a core/shell/shell quantum nanolayer [17] and a purely spherical quantum has been investigated [18]. Overall, it has been found that photoionization transitions are independent of the photon polarization for a centered impurity, while the transitions are dependent on the photon polarization when the impurity is off-centered. Influences of intense laser field and hydrostatic on PCS in pyramid-shaped quantum dots have also been reported [19]. There also have been studies of PCS in spherical core/shell zinc blende quantum structures under hydrostatic pressure and electric field [20].

In this chapter, the effect of geometry of confining electric potential on centered donor-related PCS in spherical quantum dots is investigated. The electric potentials considered are the parabolic, shifted parabolic, cup-like, and the hill-like potentials, all of which have a parabolic dependence on the radial distance of the spherical quantum dot. To start with, the Schrödinger equation is solved for the electron's eigenfunctions and energy eigenvalues within the effective mass approximation. It is emphasized that the treatment of photoionization process given here is limited only to isotropic media.

2. Theory

The basic problem of photoionization involves an electron deemed to be bound to a donor charge or indeed a center of positive charge embedded in a semiconductor specimen. An electron, upon absorbing sufficiently enough energy from the irradiating electromagnetic field, can be "liberated" from the electrostatic field of the positive charge. Now, in low-dimensional systems, the energy of an electron is quantized into different energy levels. The process of photoionization can thus involve intermediate transitions wherein an electron in some initial state $|i\rangle$ absorbs a photon of energy $\hbar\omega$ and thereby makes a transition to a final state $|f\rangle$. It is worth noting that in photoionization calculations, the initial states of the electron are described by wave functions taking into account the presence of the impurity. The final states, however, are described by the wave functions in the absence of the impurity. This notion of taking the initial and final quantum states of the electron, in a sense, is a simulation of calculations of the

binding energies in classical mechanics. The energies of the corresponding initial and final states are E_i and E_f, respectively. The system investigated here is a spherical quantum dot (SQD) of refractive index n and relative dielectric constant ε, which may be a GaAs material embedded in a $Ga_{1-x}Al_xAs$ matrix, with a donor impurity embedded at its center. Now, one of the physical quantities that are useful in the description of this binding energy-like problem is called photoionization cross section. This quantity may be regarded as the probability that a bound electron can be liberated by some appropriate radiation per unit time per unit area, given by [15–20]

$$\sigma_{lm} = \sigma_o \hbar \omega \sum_f \left| \left\langle f \right| \vec{r} \left| i \right\rangle \right|^2 \delta\left(E_f - E_i - \hbar\omega \right) \tag{1}$$

where $\left| \left\langle f \right| \vec{r} \left| i \right\rangle \right|$ is the interaction integral coupling initial states to final states, α_{FS} is the fine structure constant and $\vec{r}$ is the electron position vector. Finally, the amplitude of the PCS is given by $\sigma_o = 4\pi^2 \alpha_{FS} n E_{in}^2 / \left(3E_{av}^2 \varepsilon \right)$ in which E_{in} is the effective incident electric field and E_{av} the average electric field inside the quantum dot. Evaluation of the matrix elements for an SQD leads to the selection rules $\Delta l = \pm 1$ [21], that is, the allowed transitions are only those for which the l values of the final and initial states will be unity. In the investigations carried out here, the evaluations of the PCS are for transitions only between two electron's energy subbands. For purposes of computation, therefore, the Dirac delta function in Eq. (1) is replaced by its Lorentzian equivalent given by

$$\delta\left(E_f - E_i - \hbar\omega \right) = \frac{\hbar\Gamma}{\left(E_f - E_i - \hbar\omega \right)^2 + \left(\hbar\Gamma \right)^2}, \tag{2}$$

where this is the so-called Lorentzian linewidth.

Now, in view of spherical symmetry, the solutions of the Schrödinger wave equation are sought in the general form $\Psi_{lm}(r, \theta, \varphi) = C_{lm} Y_{lm}(\theta, \varphi) \chi(r)$, where C_{lm} the normalization constant, $Y_{lm}(\theta, \varphi)$ the spherical harmonics of orbital momentum and magnetic quantum numbers l and m, respectively. The radial part of the total wave function, $\chi(\rho)$, is found to be the following linear second-order differential equation

$$\frac{1}{r^2} \frac{d}{dr} \left(r^2 \frac{d\chi(r)}{dr} \right) + \left\{ \frac{2\mu}{\hbar^2} \left[E_{lm} + \frac{k_e e^2}{\varepsilon r} - V(r) \right] - \frac{l(l+1)}{r^2} \right\} \chi(r) = 0 \tag{3}$$

where μ is the effective mass of electron (of charge -e) and k_e is the Coulomb constant.

2.1. The electron's wave functions

The specific forms of the solutions of the differential equation described above depend on the particular electric confining potential considered. Here, the different radially dependent forms of the so-called intrinsic electric confinement potential of the spherical quantum dot, in turn, taken into account in solving Eq. (3) are (shown in **Figure 1**) (1) simple parabolic, (2) shifted
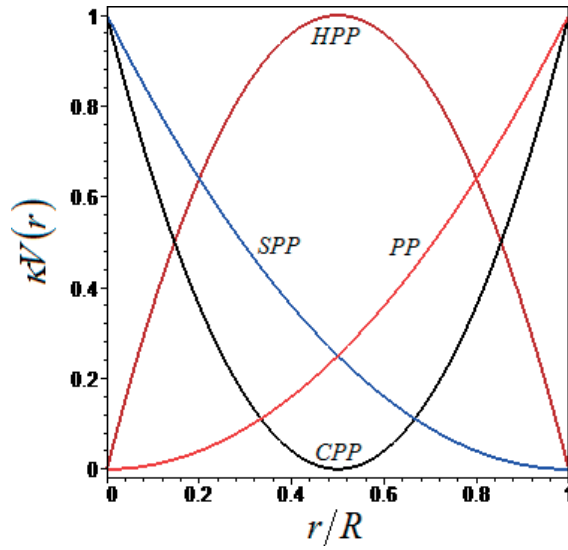
Figure 1. The spatial variation of the confining electric potentials across the SQD: simple parabolic potential (PP), shifted parabolic potential (SPP), cup-like potential (CPP), and the hill-like potential (HPP).

parabolic, (3) bi-parabolic (cup-like), and (4) inverse bi-parabolic (hill-like), each superimposed on an infinite spherical square quantum well (ISSQW).

2.1.1. Parabolic potential

When the parabolic potential (PP), which has the form

$$V(r) = \frac{1}{2}\mu\omega_0^2 r^2, \qquad (r < R) \tag{4}$$

and infinity elsewhere, is inserted into the Schrödinger equation (Eq. (2)) in the presence of the donor impurity, then the second-order differential equation is solvable in terms of the Heun biconfluent function [22, 23].

$$\chi(\rho) = C_{1lm}e^{g_1(r)}r^l HeunB\big(2l+1, \alpha, \beta, \gamma, g_2(r)\big) + C_{2lm}e^{g_1(r)}r^{-(l+1)}HeunB\big(-(2l+1), \alpha, \beta, \gamma, g_2(r)\big) \tag{5}$$

with

$$\alpha = 0, \quad \beta = -\frac{2E_{lm}}{\hbar\omega_0}, \gamma = \frac{4k_e e^2}{\varepsilon\hbar}\sqrt{-\frac{\mu}{\hbar\omega_0}} \tag{6}$$

and the arguments

$$g_1(r) = \frac{\mu\omega_0}{2\hbar}r^2, \text{ and } g_2(r) = \sqrt{2g_1(r)}. \tag{7}$$

Eq. (5) is the complete solution of the differential equation given earlier; however, the second solution diverges at the origin and so C_{2lm} must be taken as zero. The application of the standard boundary condition of continuity of the wave function at the walls ($r = R$) of the SQD leads to the following electron's energy eigenvalue equation:

$$HeunB(2l + 1, \alpha, \beta_E, \gamma, g_2(R)) = 0. \tag{8}$$

The electron's energy spectrum is derived from numerically solving Eq. (8) for its roots β_E according to

$$E_{lm} = -\frac{\beta_E}{2}\hbar\omega_0. \tag{9}$$

2.1.2. Shifted parabolic potential

This potential is convex: maximum at the center and decreases parabolically to assume a minimum value (here taken as zero) at the radius

$$V(r) = \frac{1}{2}\mu\omega_o^2(r - R)^2, \qquad (r < R) \tag{10}$$

and infinity elsewhere. The solution to the radial component of the Schrödinger equation (Eq. (3)) corresponding to this potential is also in terms of the Heun biconfluent function (Eq. (5)) but with [23]

$$\alpha = 2\sqrt{-\frac{\mu\omega_0 R^2}{\hbar}}, \quad \beta = -\frac{2E_{lm}}{\hbar\omega_0}, \gamma = \frac{4k_e e^2}{\varepsilon\hbar}\sqrt{-\frac{\mu}{\hbar\omega_0}} \tag{11}$$

and the arguments

$$g_1(r) = \frac{\mu\omega_0}{2\hbar}(r - 2R)r \text{ and } g_2(r) = -i\sqrt{\frac{\mu\omega_0}{\hbar}}r \tag{12}$$

The energy spectrum is given by the usual boundary conditions at the walls of the SQD as

$$E_{lm} = -\frac{\beta_E}{2}\hbar\omega_0 \tag{13}$$

where β_E is the value of β that satisfies the condition given in Eq. (8).

2.1.3. The bi-parabolic (cup-like) potential

The solution to the Schrödinger equation for the bi-parabolic potential

$$V(r) = \frac{1}{2}\mu\omega_0^2(r - R/2)^2,$$

(14)

and infinity elsewhere, in the presence of the impurity, is in terms of the Heun biconfluent function (Eq. (5)) [24] with

$$\alpha = iR\sqrt{\frac{\mu\omega_0}{\hbar}}, \beta = -\frac{2E_{lm}}{\hbar\omega_0}, \gamma = -\frac{4ik_e e^2}{\varepsilon\hbar}\sqrt{\frac{\mu}{\hbar\omega_0}}$$

(15)

and the arguments

$$g_1(\rho) = \frac{\mu\omega_0}{2\hbar}(\rho - R)\rho, \text{ and } g_2(\rho) = -i\sqrt{\frac{\mu\omega_0}{\hbar}}\rho.$$

(16)

Requiring that the electron wave function should vanish at the walls of the SQD avails the energy spectrum for an electron in an SQD with an intrinsic bi-parabolic potential as

$$E_{lm} = -\frac{\beta_E}{2}\hbar\omega_0$$

(17)

where β_E is the value of β that satisfies the condition stipulated in Eq. (8).

2.1.4. The inverse lateral bi-parabolic (hill-like) potential

The hill-like potential has a concave parabolic increase in the radial distance from the center to reach maximum at a radial distance half the radius ($r = R/2$), after which a concave parabolic decrease brings it to a minimum at the walls of the SQD ($r = R$)

$$V(r) = \frac{1}{2}\mu\omega_o^2(Rr - r^2), \qquad (r < R)$$

(18)

and infinity elsewhere. The radial component of the Schrödinger equation for this potential in the presence of the impurity is also solvable in terms of the Heun biconfluent function (Eq. (5)) but with [24]

$$\alpha = R\sqrt{\frac{\mu\omega_0}{i\hbar}}, \beta = \frac{\left(\mu\omega_0^2 R^2 - 8E_{lm}\right)}{4i\hbar\omega_0}, \gamma = -\frac{4ik_e e^2}{\varepsilon\hbar}\sqrt{\frac{-\mu}{i\hbar\omega_0}}$$

(19)

and the arguments

$$g_1(r) = \frac{\mu\omega_0}{2i\hbar}(R-r)r \text{ and } g_2(r) = \sqrt{\frac{-i\mu\omega_0}{\hbar}}r.$$

(20)

Application of the boundary conditions at the walls of the SQD avails the energy spectrum as

$$E_{lm} = \frac{1}{8}\mu\omega_0^2 R^2 - \frac{i\beta_E}{2}\hbar\omega_0$$

(21)

with β_E being the value of β that satisfies the condition set in Eq. (8).

3. Results and discussions

The parameters used in these calculations are relevant to *GaAs* quantum dots: effective electronic mass $\mu = 0.067m_e$, m_e being the free electron mass and $\varepsilon = 12.5$. The impurity linewidth has been taken such that $\hbar\Gamma = 0.1\ meV$ [18, 19]. The spatial variation of the confining electric potentials across the SQD is illustrated in **Figure 1**, where $\kappa = \left[2/\left(\mu\omega_0^2 R^2\right)\right]$. **Figure 2** displays the effects of these potential geometries on the ground-state radial electron wave functions across an SQD of radius $R = 250$ Å in the absence of the hydrogenic impurity. The parabolic potential shifts the electron wave functions toward the center of the SQD, while the shifted parabolic potential (SPP) shifts the electron wave functions toward the walls of the SQD. As stated earlier, the cup-like is zero at $r = 0.5R$ but maximum at both the center and at the walls of the SQD. Thus, this potential tends to "concentrate" the electron's wave functions of the excited states to regions near $r = 0.5R$ but diminish the ground-state wave functions near regions where it is maximum. By contrast, the hill-like potential is maximum at $r = 0.5R$ and thus has the opposite effect on the respective electron's wave functions.

Figure 3 depicts the variation of the first-order $(s \to p)$ and second-order $(p \to d)$ transition energies as functions of the strengths of the potentials, viz: the parabolic potential (PP), shifted parabolic potential (SPP), the cup-like potential (CPP), and the hill-like potential (HPP). These are the differences in the energies of states between which an electron is allowed to make transitions within the dipole approximation during photoionization. Now, in the absence of the impurity, the first-order transition energies ΔE_{sp} are always lower than those of second-order transition ΔE_{pd}, that is, for all values of nano-dot radius. In the presence of the impurity, however, there is some characteristic radius R_0 at which the first-order and the second-order
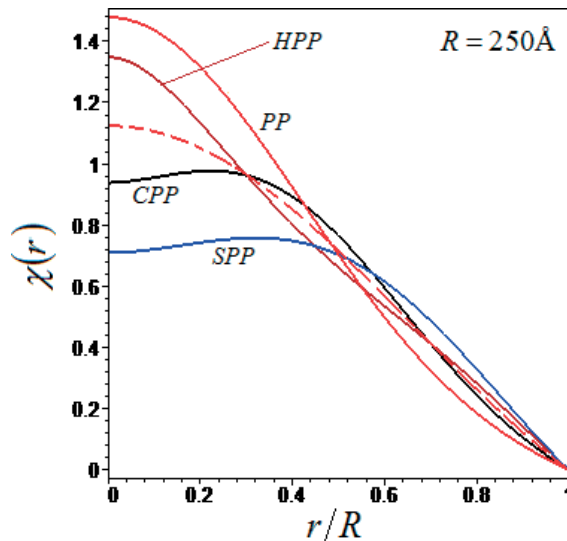

Figure 2. The effect of the different potentials on the ground-state radial electron wave function for an SQD of radius $R = 250$ Å. The potentials, parabolic (PP), shifted parabolic (SPP), cup-like (CPP), and the hill-like (HPP) all have strength $\hbar\omega_0 = 10$ meV. The dashed curve represents ground-state electron wave function in an ISSQW ($\hbar\omega_0 = 0$ meV).
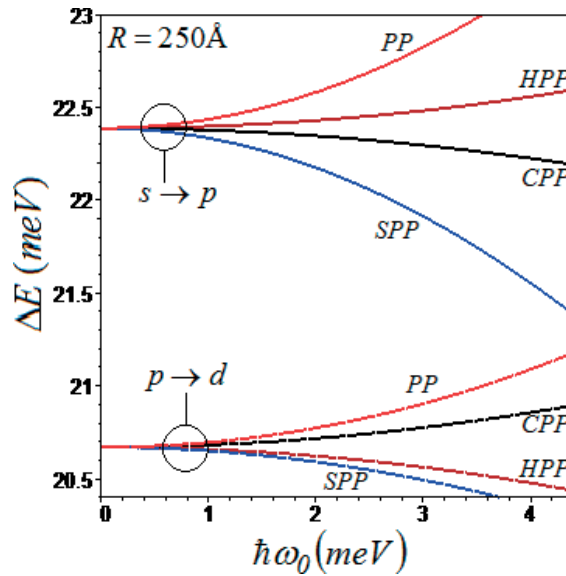
Figure 3. The dependence of the first- $(s \rightarrow p)$ and second $(p \rightarrow d)$-order transition energies on the strengths of the different potentials, viz.: the parabolic potential (PP), shifted parabolic potential (SPP), the cup-like potential (CPP), and the hill-like potential (HPP), for an SQD of radius R = 250 Å.

transition energies coincide. For the system investigated here, this radius is in the neighborhood of $R_0 = 171$ Å. For SQDs with radii less (greater) than R_0, the second-order transition energies are more (less) than the first-order transition energies. The parabolic potential and hill-like potentials reduce the value of this radius as they intensify. On the contrary, increasing the strengths of the shifted parabolic potential and the cup-like potentials increases R_0, sending it to infinity as it intensifies further. In this case, ΔE_{sp} and ΔE_{pd} would never coincide and $\Delta E_{pd} > \Delta E_{sp}$. The parabolic potential widens the gap between the energies of the initial and final states, regardless of the order of transition. The increase is more pronounced in transitions involving the lower states than in transitions involving the higher states. The shifted parabolic potential decreases transition energies also regardless of the order of transition, and with the reduction being more pronounced for transitions involving the lower states than in those involving the higher states. However, the situation is not so straightforward with the cup-like and the hill-like potentials. The cup-like potential decreases transition energies of only transitions involving the ground (s) state and enhances transition energies involving higher states. The hill-like potential increases only the transition energies involving the ground state but decreases transition energies involving higher states.

Figure 4 shows the sum of the $s \rightarrow p$ and $p \rightarrow d$ normalized photoionization cross sections for an SQD of radius R = 250 Å, where the dashed curve is for an ISSQW ($\hbar\omega_0 = 0$ meV) while the solid curve corresponds to the parabolic potential of strength $\hbar\omega_0 = 5$ meV superimposed on the ISSQW. Here, as in subsequent figures, the radius of the SQD is greater than R_0, thus the $s \rightarrow p$ peak occurs at larger beam energies than the second-order peak. Increasing the strength
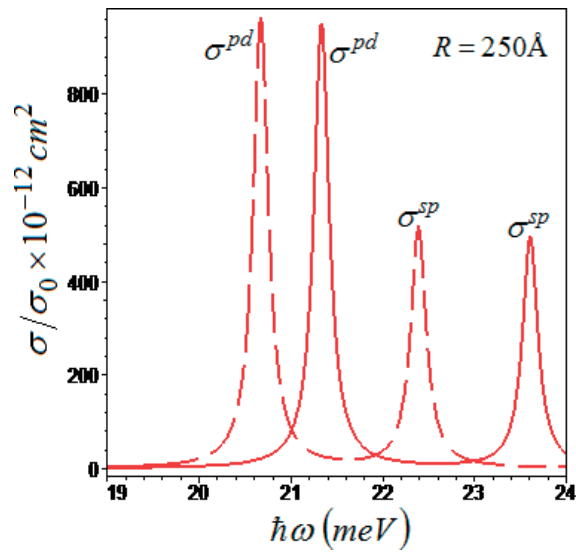
Figure 4. The sum of the first- and second-order normalized PCSs as functions of beam energy for the ISSQW (dashed curves) and for an SQD with the parabolic potential of strength $\hbar\omega_0 = 5$ meV superimposed on an ISSQW (solid plots), for a radius $R = 250$ Å.

of the parabolic potential blueshifts the peaks of the PCS, simultaneously moving them apart. This can be beneficial in cases where transitions between different states (e.g., the $s \rightarrow p$ and the $p \rightarrow d$ transitions) need to be isolated and distinct, for research or practical purposes.
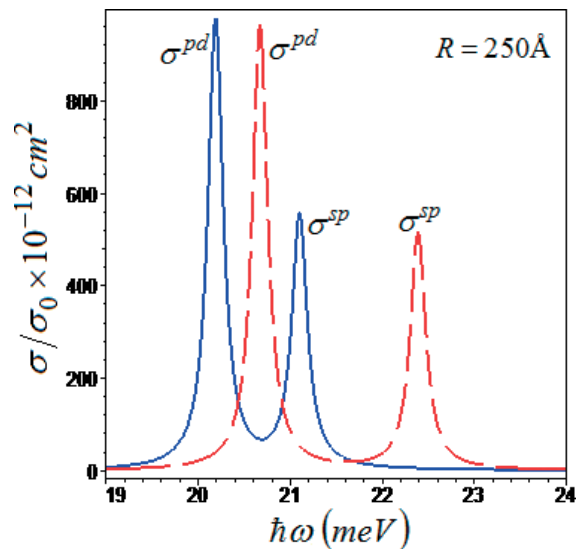

Figure 5. The sum of the first- and second-order normalized PCSs as functions of beam energy for the ISSQW (dashed curves) and for an SQD with the shifted parabolic potential of strength $\hbar\omega_0 = 5$ meV superimposed on an ISSQW, for a radius $R = 250$ Å.

Figure 5 depicts the summed normalized PCS for the $s \rightarrow p$ and $p \rightarrow d$ transitions in an SQD of radius R = 250 Å. The dashed curve is associated with the ISSQW ($\hbar\omega_0 = 0$ meV) while the solid plot corresponds to PCS for an SQD with a shifted parabolic potential of the so-called strength such that $\hbar\omega_0 = 5$ meV. Overall, the shifted parabolic potential redshifts the resonance peaks of the PCSs. It is interesting to note, however, that the first-order resonance peak redshifted to a much greater extent than that of the second order. These results suggest that the shifted parabolic potential can be utilized to manipulate the first-order and second-order transitions according to their corresponding photon energy of excitation [23].

Figure 6 illustrates the normalized $s \rightarrow p$ and $p \rightarrow d$ PCSs as functions of the photon energy for an SQD of radius R = 250 Å. The dashed curve is for the purely ISSQW ($\hbar\omega_0 = 0$ meV) while the solid plot is for the cup-like potential of strength $\hbar\omega_0 = 5$ meV superimposed on the ISSQW. As can be clearly seen from the figure, the cup-like potential redshifts peaks of the $s \rightarrow p$ PCS while it blueshifts the peaks of the $p \rightarrow d$ PCS. This potential also blueshifts peaks of PCS of transitions involving higher states ($d \rightarrow f, f \rightarrow g$ and so forth).

Figure 7 depicts the variation of the normalized $s \rightarrow p$ and $p \rightarrow d$ PCSs with the photon energy for an SQD of radius R = 250 Å. Here also, the dashed curve represents the purely ISSQW ($\hbar\omega_0 = 0$ meV) while the solid plot is for the hill-like potential of strength $\hbar\omega_0 = 5$ meV superimposed on the ISSQW. Increasing the strength of the hill-like potential blueshifts the peaks of the $s \rightarrow p$ PCS while it redshifts those of the $p \rightarrow d$ PCS. Although not shown here, the hill-like potential also redshifts peaks of the PCS associated with transitions from higher states ($d \rightarrow f, f \rightarrow g$ and so forth).
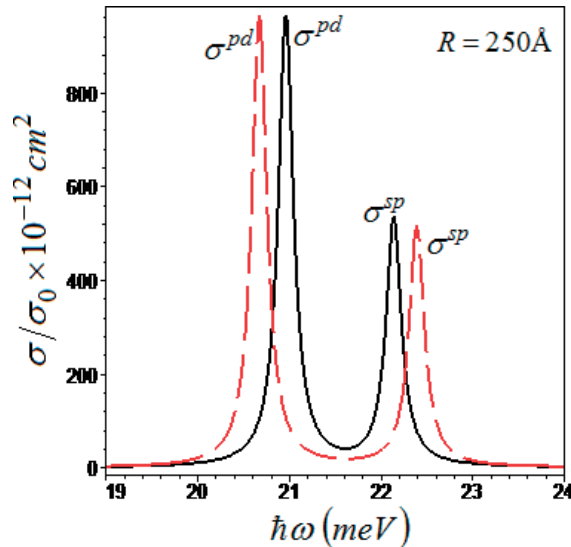

Figure 6. The sum of the first- and second-order normalized PCSs as functions of beam energy for the ISSQW (dashed curves) and for an SQD with the cup-like potential of strength $\hbar\omega_0 = 5$ meV superimposed on an ISSQW, for a radius R = 250 Å.
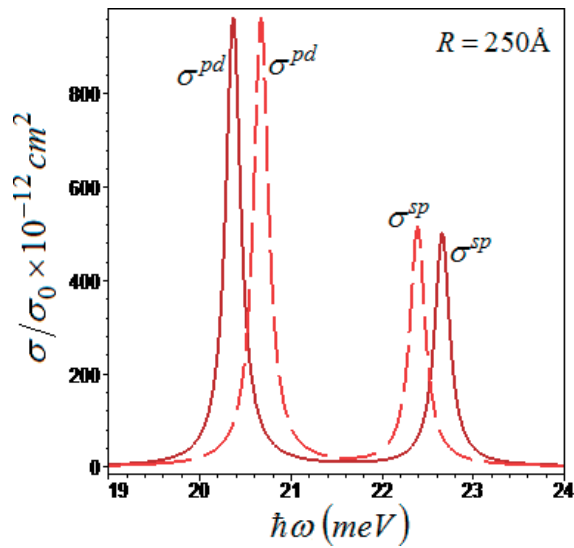
Figure 7. The sum of the first- and second-order normalized PCSs as functions of beam energy for the ISSQW (dashed curves in both) and for an SQD with the hill-like potential of strength $\hbar\omega_0 = 5$ meV superimposed on an ISSQW, for a radius $R = 250$ Å.

4. Conclusions

The electron's wave functions in a spherical quantum dot with a centered donor impurity have been obtained, and these were utilized to evaluate the effects of the geometry of confining electric potentials on PCS in an SQD. The parabolic potential enhances photoionization transition energies independent of the initial or the final state, while the shifted parabolic potential decreases the transition energies, also independent of the order of transition. As a result, the parabolic potential blueshifts the peaks of the PCS, while the shifted parabolic potential redshifts the peaks, for all transitions. The cup-like and the hill-like potentials exhibit a selective enhancement or a reduction of transition energies. The hill-like parabolic potential enhances the transition energies involving the ground state but dwindles those involving higher states. A consequence of this effect is that the hill-like parabolic potential blueshifts peaks of $s \rightarrow p$ PCS but redshifts those involving higher states. The situation is the other way around in the case of the cup-like parabolic potential. The results presented here also suggest that nano-patterning techniques may offer yet another method of tuning the process of photo-ionization to resonance, through tailored electric potentials.

Conflict of interest

The authors have no conflict of interest to declare.

Author details

Moletlanyi Tshipa* and Monkami Masale

*Address all correspondence to: tshipam@mopipi.ub.bw

University of Botswana, Gaborone, Botswana

References

[1] Meng L, He X, Gao J, Li J, Wei Y, Yan J. A novel nanofabrication technique of silicon-based nanostructures. Nanoscale Research Letters. 2016;**11**:504. DOI: 10.1186/s11671-016-1702-4

[2] Moura I, de Sá A, Abreu AS, Oliveira M, Machado AV. Morphology, optical, and electric properties of polymer-quantum dots nanocomposites: Effect of polymeric matrix. Journal of Materials Science. 2016;**51**:8699-8710. DOI: 10.1007/s10853-016-0129-8

[3] Sadeghimakki B, Zheng Y, Jahed NMS, Sivoththaman S. Synthesis of CIS quantum dots in low-temperature regime: Effects of precursor composition and temperature ramps. IEEE Transactions on Nanotechnonlogy. 2017;**16**(4):659-666. DOI: 10.1109/TNANO.2017.2703162

[4] Chan WCW, Maxwell DJ, Gao X, Bailey RE, Han M, Nie S. Luminescent quantum dots for multiplexed biological detection and imaging. Current Opinion in Biotechnology. 2002;**13**:40-46

[5] Bwatanglang IB, Mohammad F, Yusof NA, Abdullah J, Hussein MZ, Alitheen NB, Abu N. Folic acid targeted Mn:ZnS quantum dots for theranostic applications of cancer cell imaging and therapy. International Journal of Nanomedicine. 2016;**11**:413-428. DOI: 10.214/IJN.S90198

[6] Chen J, Liu D, Al-Marri M, Nuuttila L, Lehtivuori H, Zheng K. Photo-stability of CsPbBr3 perovskite quantum dots for optoelectronic application. Science China Materials. 2016;**59**(9):719-727. DOI: 10.1007/s40843-016-5123-1

[7] Litvin AP, Martynenko IV, Purcell-Milton F, Baranov AV, Fedorov AV, Gun'ko YK. Colloidal quantum dots for optoelectronics. Journal of Materials Chemisrty A. 2017;**5**: 13252-13275. DOI: 10.1039/c7ta02076g

[8] Li X, Rui M, Song J, Sheh Z, Zeng H. Carbon and grapheme quantum dots for optoelectronic and energy devices: A review. Advanced Materials. 2015;**25**:4929-4947. DOI: 10.1002/adfm.201501250

[9] Lan X, Voznyy O, Kiani A, de Arquer FPG, Abbas AS, Kim G-H, Liu M, Yang Z, Walters G, Xu J, Yuan M, Ning Z, Fan F, Kanjanaboos P, Kramer I, Zhitomirsky D, Lee P, Perelgut A, Hoogland S, Sargent EH. Passivation using molecular halides increases quantum dot solar cell performance. Advanced Materials. 2016;**28**:299-304. DOI: 10.1002/adma.201503657

[10] Xu W-P, Zhang Y-Y, Wang Q, Li Z-J, Nie Y-H. Thermoelectric effects in triple quantum dots coupled to a normal and a superconducting leads. Physics Letters A. 2016;**380**:958-964. DOI: 10.1016/s0014-5793(01)03293-8

[11] Ding W-L, Peng X-L, Sun Z-Z, Li Z-S. Novel bifunctional aromatic linker utilized in CdSe quantum dots-sensitized solar cells: Boosting the open circuit voltage and electron injection. Journal of Materials Chemistry A. 2017;**5**:14319-14330. DOI: 10.1039/c7ta03349d

[12] Cortés N, Rosales L, Chico L, Pacheco M, Orellana PA. Enhancement of thermoelectric efficiency by quantum interference effects in trilayer silicone flakes. Journal of Physics: Condensed Matter. 2017;**29**:015004. DOI: 10.1088/0953-8984/29/1/015004

[13] Yang C, Xiao F, Wang J, Su X. 3D flower- and 2D- sheet-like CuO nanostructures: Microwave assisted synthesis and application in gas sensors. Sensors and Actuators B. 2015;**207**: 177-185. DOI: 10.1016/j.snb.2014.10.063

[14] Xie W. Binding energy of an off-center hydrogenic donor in a spherical Gaussian quantum dot. Physica B: Condensed Matter. 2008;**403**:2828-2831. DOI: 10.1016/j.physb.2008.02.017

[15] Baghramyan HM, Barseghyan MG, Kirakosyan AA, Laroze D, Duque CA. Donor-impurity related photoionization cross section in GaAs/Ga$_{1-x}$Al$_x$As concentric double quantum rings: Effects of geometry and hydrostatic pressure. Physica B: Condensed Matter. 2014;**449**:193-198. DOI: 10.1016/j.physb.2014.05.034

[16] Iqraoun E, Sali A, Rezzouk A, Feddi E, Dujardin F, Mora-Ramos ME, Duque CA. Donor impurity-related photoionization cross section in GaAs cone-like quantum dots under applied electric field. Philosophical Magazine. 2017;**97**(18):1445-1463. DOI: 10.1080/14786435.2017.1302613

[17] Baghdasaryan DA, Kazaryan EM, Sarkisyan HA. Photoionization and electrostatic multipoles properties of spherical core/shell/shell quantum nanolayer with off-center impurity. Superlatticess and Microstructures. 2017;**104**:69-77. DOI: 10.1016/j.spmi.2017.02.017

[18] Ham H, Lee CJ. Photoionization cross section of hydrogenic impurities in spherical quantum dots: Infinite well model. Journal of the Korean Physical Society. 2003;**42**:S688-S692

[19] Niculescu EC. Impurity-related photoionization cross section in a pyramid-shaped quantum dot: Intense laser field and hydrostatic pressure effects. Physica E: Low-dimensional Systems and Nanostructures. 2014;**63**:105-113. DOI: 10.1016/j.physe.2014.05.012

[20] El Ghazi H, Peter AJ. Photoionization cross-section of donor-related in (in,Ga)N/GaN core/shell under hydrostatic pressure and electric field effects. Superlattices and Microstructures. 2017;**104**:222-231. DOI: 10.1016/j.spmi.2017.02.013

[21] Xie W. Hydrostatic pressure effect on photoionization cross section of a Trion in quantum dots. Superlattices and Microstructures. 2013;**63**:10-17. DOI: 10.1016/j.spmi.2013.08.011

[22] Ronveaux A. Heun's Differential Equations. Oxford: Oxford University Press; 1995

[23] Tshipa M. Photoionization cross section in a spherical quantum dot: Effects of some parabolic confining electric potentials. Condensed Matter Physics. 2017;**20**(2):23703:1-9. DOI: 10.5488/CMP.20.23703

[24] Tshipa M. The effects of cup-like and hill-like parabolic confining potentials on photoionization cross section of a donor in a spherical quantum dot. The European Physical Journal B. 2016;**89**:177. DOI: 10.1140/epjb/e2016-60988-6
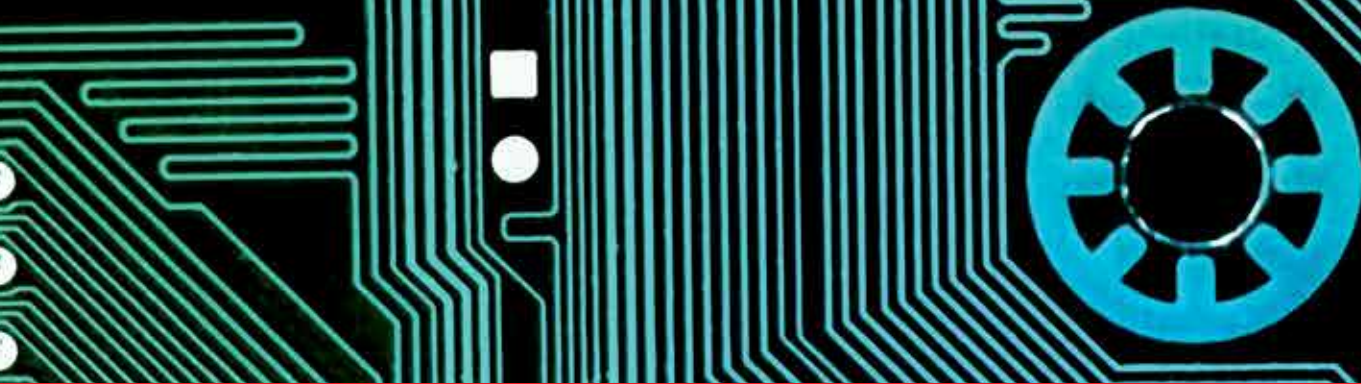
Edited by Vasilios N. Stavrou

The current book entitled *Heterojunctions and Nanostructures* is divided into two sections. In Section 1, the chapters are related to topological insulators where their theoretical aspects, their current experiments, and their applications are presented. A few presented topics are, among others, the topological phases of matter, band topology of insulators and also of Weyl semimetals, transport properties of 3D topological insulator quantum wires and the influence of disorder, transport properties of quasi-1D (and 2D) topological surface states, quantum coherence, and topological insulator thin-film Hall bar device. In Section 2, the chapters are related to light devices such as laser diodes and their fabrication techniques. This section includes, among others, topics such as semiconductor quantum nanowire laser diodes, solutions of Schrodinger equation in nanostructures, numerical methods, light-to-electricity conversion devices, photoexcited carrier transportation process in quantum wells and quantum dots, growth mode and characterization of heterostructure of large lattice mismatch, and photoionization cross section.

IntechOpen